Spring 2021

Fiber-optic and coaxial-cable extrinsic Fabry-Perot interferometers for sensing applications

Chen Zhu

Department: Electrical and Computer Engineering

FIBER-OPTIC AND COAXIAL-CABLE EXTRINSIC FABRY-PEROT INTERFEROMETERS FOR SENSING APPLICATIONS

by

CHEN ZHU

A DISSERTATION

Presented to the Graduate Faculty of the

MISSOURI UNIVERSITY OF SCIENCE AND TECHNOLOGY

In Partial Fulfillment of the Requirements for the Degree

DOCTOR OF PHILOSOPHY

in

ELECTRICAL ENGINEERING

2021

Approved by:

Dr. Jie Huang, Advisor
Dr. Kristen M. Donnell
Dr. Steve E. Watkins
Dr. Xiaodong Yang
Dr. Jiangfan Zhang

PUBLICATION DISSERTATION OPTION

This dissertation consists of the following four articles, formatted in the style used by the Missouri University of Science and Technology:

Paper I, found on pages 8–23, C. Zhu, Y. Chen, Y. Du, Y. Zhuang, F. Liu, R.E. Gerald II, and J. Huang, "A Displacement Sensor with Centimeter Dynamic Range and Submicrometer Resolution Based on an Optical Interferometer", has been published in IEEE Sensors Journal, vol. 17, no. 17, pp. 5523-5528, 2017.

Paper II, found on pages 24–44, C. Zhu, Y. Chen, Y. Zhuang, Y. Du, R.E. Gerald II, Y. Tang, and J. Huang, "An Optical Interferometric Triaxial Displacement Sensor for Structural Health Monitoring: Characterization of Sliding and Debonding for a Delamination Process", has been published in Sensors, vol. 17, no. 11, p. 2696, 2017.

Paper III, found on pages 45–72, C. Zhu, R.E. Gerald II, Y. Chen, and J. Huang, "Probing the Theoretical Ultimate Limit of Coaxial Cable Sensing: Measuring Nanometer Scale Displacements", has been published in IEEE Transactions on Microwave Theory and Techniques, vol. 68, pp. 816-823, 2019.

Paper IV, found on pages 73–102, C. Zhu, R.E. Gerald II, Y. Chen, and J. Huang, "Portable Metal-organic Framework Sensor", has been published in Sensors and Actuators B: Chemical, vol. 321, p. 128608, 2020.

ABSTRACT

The fiber-optic extrinsic Fabry-Perot interferometer (EFPI) is one of the simplest sensing configurations and is widely used in various applications due to its prominent features, such as high sensitivity, immunity to electromagnetic interference, and remote operation capability. In this research, a novel one-dimensional wide-range displacement sensor and a three-dimensional displacement sensor based on fiber-optic EFPIs are demonstrated. These two robust and easy-to-manufacture sensors expand the application scope of the fiber-optic EFPI sensor devices, and have great potential in structural health monitoring, the construction industry, oil well monitoring, and geo-technology.

Furthermore, inspired by the fiber-optic EFPI, a novel and universal ultra-sensitive microwave sensing platform based on an open-ended hollow coaxial cable resonator (OE-HCCR, i.e., the coaxial cable EFPI) is developed. Both the theoretical predictions and experimental results demonstrate the ultra-high sensitivity of the OE-HCCR device to variations of the gap distance between the endface of the coaxial cable and an external metal plate. Additionally, combining the chemical-specific adsorption properties of metal-organic framework (MOF) materials with the dielectric sensitivity of the OE-HCCR, a mechanically robust and portable gas sensor device (OE-HCCR-MOF) with high chemical selectivity and sensitivity is proposed and experimentally demonstrated. Due to its low cost, high sensitivity, all-metal structure, robustness, and ease of signal demodulation, it is envisioned that the proposed OE-HCCR device will advance EFPI sensing technologies, revolutionize the sensing field, and enable many important sensing applications that take place in harsh environments.

ACKNOWLEDGMENTS

I would like to take this opportunity to thank all those people who helped me during my academic journey towards a Ph.D. in Electrical Engineering. First and foremost, I would like to express my sincere gratitude to my advisor, Dr. Jie Huang, for giving me a chance to work with him. His continuous guidance and generous support throughout the past four years have encouraged me to finish the Ph.D. program with great enthusiasm. His patience, profound, insight, and selfless guidance have not only continuously inspired me in research but also made a great impact on my personality, and will continue inspiring me as I move forward as a researcher.

I would like to thank Dr. Jie Huang, Dr. Kristen M. Donnell, Dr. Steve E. Watkins, Dr. Jiangfan Zhang, and Dr. Xiaodong Yang for serving on my committee and for the valuable advice and suggestions for the completion of my research.

I am also grateful to Dr. Rex E. Gerald II for his help and mentorship during my time in the Ph.D. program. I still remember the interactions that we had during our first collaborative project, the development of a wide-range fiber-optic displacement sensor, when I was deeply motivated by his insight, critical thinking, creativity, and patience. His personality has inspired me and will keep pushing me forward in my future academic life.

I would also like to thank all the colleagues in the Lightwave Technology Lab at Missouri S&T and my friends for their help in my research and life.

Last but not least, I would like to thank my parents and other family members for their love and support, especially during the current 2020 pandemic. Without their love and support, I would not have been able to finish this dissertation.

TABLE OF CONTENTS

Page

LIST OF ILLUSTRATIONS

SECTION Page

PAPER III

PAPER IV

SECTION

LIST OF TABLES

PAPER III Page

1. INTRODUCTION

1.1. BACKGROUND AND MOTIVATIONS

Interferometry is one of the most widely used investigative techniques in various fields [1]. Interferometers are a group of interferometric devices that are commonly used in a multitude of scientific and industrial applications for measurements of a variety of physical and chemical quantities, such as displacement, pressure, refractive index, etc. [2, 3]. In an interferometer, two coherent electromagnetic (EM) waves are superimposed, causing the phenomenon of interference, to generate periodic patterns. These patterns contain the information about the propagation delay between the two EM waves. In turn, by analyzing the interference pattern, the propagation delay of the interferometer can be determined. Therefore, an interferometer can measure any quantity of interest that can be correlated to its propagation delay. Based on different implementations of splitting and combining the two coherent EM waves, several configurations have been developed: the Fabry-Perot interferometer (FPI), the Michelson interferometer (MI), the Mach-Zehnder interferometer (MZI), the Sagnac interferometer, and the Fizeau interferometer [4].

Among the different configurations, the FPI is the simplest interferometer configuration. An FPI consists of two partially reflecting surfaces [5]. The incident EM wave is directly and partially reflected by the first reflecting surface; the rest of the EM wave goes through the Fabry-Perot (FP) cavity, where it reaches and reflects off the second reflecting surface. The reflected wave then transmits through the cavity and the first reflecting surface again. The two reflected EM waves with a certain propagation delay (defined by the FP cavity length and the cavity medium) superimpose to generate

interference fringes that have information about the FP cavity. Compared with other interferometers, FPIs are unique in their compactness and ease of fabrication.

Optical fibers and coaxial cables are two types of cylindrical waveguides widely used in telecommunications. Described by the same EM theory, both optical fibers and coaxial cables can transmit EM waves over long distances. However, the frequencies of the EM waves supported by them are quite different, i.e., optical frequency (e.g., THz) for optical fibers and radio frequency (e.g., GHz) for coaxial cables. Therefore, optical fibers and coaxial cables have evolved along quite different pathways over the years. Particularly, optical fibers have been extensively exploited for sensing applications, while coaxial cables are mainly used for radiofrequency communications.

Fiber-optic FPIs are one of the most popular fiber-optic sensing configurations [6]. Generally, fiber-optic FPIs can be divided into two categories, the intrinsic FPI (IFPI) and the extrinsic FPI (EFPI), as illustrated in Figure 1.1. Figure 1.1(a) is a schematic representation of a fiber-optic IFPI that is formed between two fiber in-line reflectors. The solid optical fiber between the two reflectors serves as the FP cavity. The fiber-inline reflectors can be typically fabricated using micromachining techniques, e.g., femtosecond laser inscription. The IFPI is small in size, can be multiplexed in series, and is typically used for temperature and strain sensing, but requires costly micromachining processes. On the other hand, the fiber-optic EFPI, as shown in Figure 1.1(b), is much easier to fabricate. The EFPI is formed between a cleaved end facet of an optical fiber and an external reflector (i.e., an optically reflective surface), and the gap between the endface of the optical fiber and the external reflector serves as the FP cavity. Although with the increased size due to the extrinsic configuration, EFPI-based sensors have found wider applications than IFPI-

based sensors. Any physical parameter that can be correlated to the movement (displacement) of the external reflector (via a mechanical transducer) can be measured using an EFPI sensor. Chemical parameters that can be correlated to the refractive index of the cavity medium can be measured as well. However, on one hand, the application of the fiber-optic EFPI is stilled limited so far, e.g., for one-dimensional wide-range and three-dimensional displacement measurements. On the other hand, to ensure a stable and high-quality interference signal, single-mode fibers (SMFs) are typically employed to construct EFPI sensors, which essentially limit the application scope of EFPI sensors [7]. For instance, SMFs are made of fused silica, which is not stable at extremely high temperatures (e.g., >1000 °C). Therefore, high-temperature applications of fiber-optic EFPI sensors are hindered. Additionally, accurate interrogation and demodulation of a fiber-optic EFPI sensor are relatively difficult to achieve, requiring a broadband light source, a high-precision spectrometer, and sophisticated algorithms.

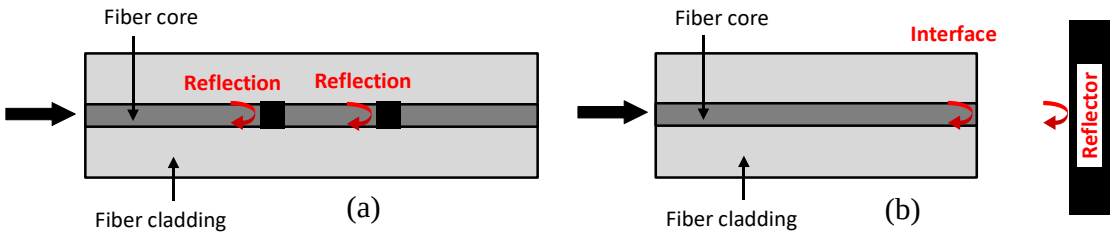

Figure 1.1. Schematics of fiber-optic FPIs. (a) IFPI. (b) EFPI.

In recent years, researchers strived to translate several fiber-optic sensing configurations to coaxial cables, including the fiber Bragg grating [8] and the IFPI [9], as shown in Figure 1.2. The cable-inline reflectors could be fabricated using a simple hole-

drilling method. The resultant coaxial cable Bragg grating and the coaxial cable Fabry-Perot interferometer were demonstrated for sensing strain up to 5% [10], which is approximately five times larger than the maximum strain measured by traditional fiber-optic sensors. The demonstrated coaxial cable-based sensor devices provided a promising solution for some challenging issues faced by their optical counterparts, optical fiber-based sensor devices, for example, fragility, the difficulties associated with installation, stringent requirements regarding fabrication, stringent alignment requirements, and large-strain tolerance. However, material limitations attributed to the dielectric layer inside a coaxial cable (e.g., polyethylene, which can only survive up to 200 °C), hinder the development of coaxial cable-based sensors for high-temperature and harsh environments. Very recently, we proposed and demonstrated a new sensing structure, the hollow coaxial cable Fabry-Perot resonator (HCC-FRP), inspired by the Fabry-Perot etalon [11-15]. The all-metal design of the HCC-FPR greatly improves its thermal stability and tolerance, which is expected to provide an alternative to fiber-optic counterparts for extremely high-temperature sensing applications. However, the existing coaxial cable in-line sensor devices suffered from low measurement resolution due to the long interrogation wavelength, approximately two orders of magnitude lower resolution than that typically encountered for fiber-optic sensors. Additionally, the structural design flexibility of HCC-FRP devices is limited due to the in-line structure.

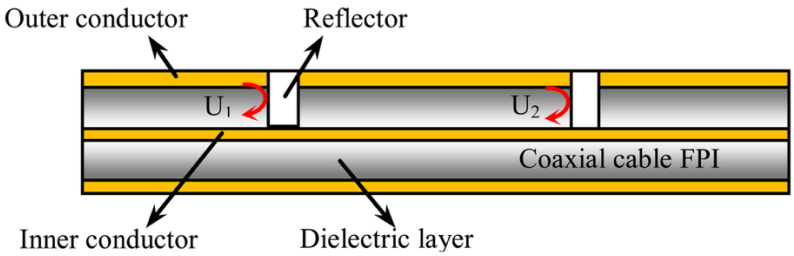

Figure 1.2. Schematic of the coaxial cable IFPI [9].

1.2. OBJECTIVES AND ORGANIZATION OF THE DISSERTATION

As discussed in the previous section (Section 1.1), more studies need to be performed to advance the fiber-optic EFPI sensing and coaxial cable sensing technologies. Toward this end, the objectives of this dissertation are to:

1) Propose and demonstrate a displacement transfer mechanism to facilitate the fiber-optic EFPI for wide-range and sensitive one-dimensional displacement sensing.

2) Demonstrate a fiber-optic EFPI-based three-dimensional displacement sensor for characterization of interfacial sliding and debonding between two different objects.

3) Propose and demonstrate a microwave sensing scheme to improve the measurement sensitivity and resolution of coaxial cable-based sensor devices.

4) Develop a coaxial cable-based portable and robust chemical sensor device for gas sensing applications.

The investigation results are presented in the form of four published journal papers in this dissertation and their contents are briefly described as follows.

In Paper I, a user-configurable triangle geometry-based displacement transfer mechanism is proposed and from which a low cost and compact EFPI based optical fiber

displacement sensor with a wide dynamic range, up to 2.0 cm and 0.270 μm resolution, is developed. The fundamental design principle includes an inclined mirror, mounted on a translational stage, that combines with the endface of a single-mode fiber to form a Fabry-Perot cavity. The user-configurable triangle geometry-based displacement transfer mechanism makes the sensor capable of measuring a wide displacement range. A fiber ceramic ferrule is used to support and orient the optical fiber and a metal shell is used to package and protect the principal sensor elements. The novel sensor was employed to monitor shrinkage during the drying/curing stage of a square brick of mortar, demonstrating the utility and stability of the sensor device.

In Paper II, a fiber-optic EFPI-based optical fiber sensor for measuring three-dimensional displacements, including interfacial sliding and debonding during delamination, is developed. The idea employs three spatially arranged EFPIs as the sensing elements. In the sensor, the three EFPIs are formed by three endfaces of three optical fibers and their corresponding inclined mirrors. Two coincident roof-like metallic structures are used to support the three fibers and the three mirrors, respectively. The sensor was calibrated and then used to monitor interfacial sliding and debonding between a long square brick of mortar and its support structure (i.e., a steel base plate) during the drying/curing process.

In Paper III, a novel sensing scheme based on an open-ended hollow coaxial cable resonator (OE-HCCR) is demonstrated, which is inspired by the fiber-optic EFPI. The resonator is constructed using two reflectors along the coaxial line. The first reflector is a metal post at the RF input end, shorting the inner and outer conductors. The second reflector is the open end, where a metal plate is placed parallel and near the open end. The

resonance frequency of the open-ended coaxial resonator depends strongly on the gap distance between the metal plate and the open end of the coaxial cable, due to a modulation of the phase of the reflection coefficient that characterizes the open end. Thus, by correlating the resonance frequency to the gap distance between the metal plate and the open end (or the movement of the metal plate), the OE-HCCR can be used as a displacement sensor device. Importantly, the displacement measurement resolution of the OE-HCCR is three orders of magnitude greater than that of existing coaxial cable-based displacement sensors within a certain dynamic range (~ 0.11 mm), affording a resolution that is comparable to fiber optic sensors. The mathematical model of the OE-HCCR is discussed in detail, followed by a proof-of-concept for displacement measurements.

In Paper IV, a mechanically robust and portable gas sensor device with high chemical selectivity and sensitivity is proposed and experimentally demonstrated by combining the chemical-specific adsorption properties of metal-organic framework (MOF) materials with the dielectric sensitivity of the OE-HCCR. The changes in the dielectric property of the MOF layer in response to variations in concentrations of guest molecules modify the phase-matching condition of the microwave resonator, causing shifts in the resonance frequency of the device. By monitoring the resonance frequency shift, the adsorptions of guest molecules can be monitored in real-time and accurately quantified. In proof-of-concept demonstrations, a 200-μm layer of MOF (HKUST-1) was placed within an OE-HCCR to develop a prototype OE-HCCR-MOF sensor. The novel sensor showed high sensitivity to variations in the concentrations of carbon dioxide with good reversibility. The chemical selectivity of the prototype sensor for carbon dioxide compared to methane was also investigated.

PAPER

I. A DISPLACEMENT SENSOR WITH CENTIMETER DYNAMIC RANGE AND SUBMICROMETER RESOLUTION BASED ON AN OPTICAL INTERFEROMETER

ABSTRACT

We report a low cost and compact extrinsic Fabry-Perot interferometer-(EFPI) based optical fiber displacement sensor with a wide dynamic range, up to 2.0 cm, and 0.270 μm resolution. The fundamental design principle includes an inclined mirror, mounted on a translational stage, that combines with the endface of a single mode fiber to form a Fabry-Perot cavity. The user-configurable triangle geometry based displacement transfer mechanism makes the sensor capable of measuring a wide displacement range. A fiber ceramic ferrule is used to support and orient the optical fiber and a metal shell is used to package and protect the principal sensor elements. The novel sensor was employed to monitor shrinkage during the drying/curing stage of a square brick of mortar. The robust and easy-to-manufacture sensor can be easily commercialized and has great potential for applications in the chemical-oil industry, construction industry and other industries with harsh environments.

1. INTRODUCTION

Fiber-optic sensors have attracted extensive interests in recent years and have been widely used in various fields, such as biology, chemistry, structural health monitoring

(SHM), and in the military to measure physical parameters such as liquid level, liquid and gas concentration, strain, temperature, curvature, and displacement [1-7]. Compared with conventional sensing technologies, fiber optic sensors have a lot of attractive characteristics, such as immunity to electromagnetic field, light weight, high accuracy, ease of fabrication, the possibility of remote operation, and distributed sensing capabilities [1-7].

Displacement fiber sensors with high precision and wide operational range play an important role in scientific and technological applications as they can be used for precise movement control or position monitoring [7]. Several types of optical fiber displacement sensors have already been developed, primarily including wavelength modulated sensors, reflective intensity modulated sensors, and interferometric sensors. Wavelength modulated sensors, including fiber Bragg grating (FBG) and long-period grating (LPG), have been demonstrated to have a wide sensing range and high sensitivity [8-10]. However, their fabrication is costly and complicated, involving a phase mask, a UV laser, or a CO_2 laser. Additionally, material fatigue is always a concern for these sensors in long-term applications [11]. Intensity modulated sensors have the simplest configuration in which the light power transmitted between the fiber sensor heads and the target surface is modulated, but they suffer from low sensitivity and can be easily influenced by the intensity fluctuations of the laser source [12]. Interferometric sensors have comparable sensitivity to wavelength modulated sensors but are much easier to fabricate, and they are more stable than intensity based sensors [12]. Many types of interferometers have been reported in the literature. For instance, Wu *et al.* presented a bent singlemode multimode singlemode (SMS) structure for displacement measurement with a dynamic range of 600 μm [13]. Chen

et al. proposed a Mach-Zehnder Interferometer (MZI) displacement sensor by concatenating two core-offset joints with a measurement dynamic range of 1 mm [11]. A Michelson Interferometer (MI) with a displacement measurement limit of 3 mm was proposed by Rong *et al.* [14]. Bravo *et al.* reported a Hi-Bi fiber based Sagnac loop sensor for displacement measurements with a dynamic range of 400 μm [15]. Dash *et al.* demonstrated a photonic crystal fiber (PCF) based modal interferometer purporting a nanometer-level resolution but only with a measurement range of 700 μm [7]. The aforementioned interferometric sensors required fusion splicing during the fabrication process, which may affect the stability of the sensor. In addition, all the interferometric sensors mentioned above use bending structures which could further reduce long-term stability of the sensors.

A widely used interferometric sensor, the extrinsic Fabry-Perot interferometer (EFPI), is more suitable for displacement measurements because the phase information of an FPI signal can be directly influenced by the position of the external reflecting surface [16]. Moreover, an air gap is introduced as the resonance cavity in the EFPI, meaning the sensor will have a small temperature cross-talk. Therefore, with judicious mechanical design and packaging, EFPI sensors are excellent candidates for displacement or strain measurement devices. Zhou *et al.* proposed an EFPI displacement sensor with a very simple configuration [17]. FPI arrays along an optical fiber have also been developed for distributed strain sensing applications [18-19]. However, the dynamic range of the reported EFPI based displacement sensor is limited to several millimeters due to the maximum cavity length of the FPI that can be demodulated.

In this paper, we report and demonstrate a stable triangle compression EFPI (TC-EFPI) displacement sensor. A user-configurable triangle geometry based displacement transfer mechanism is employed, which enables the sensor to have a very wide measurement range, up to the level of multiple centimeters. Moreover, the novel mechanical design affords an adjustable dynamic range amplification factor and a substantial reduction of systematic displacement errors due to variations in temperature. In our sensor design, an optical fiber ceramic ferrule used to support the optical fiber is inserted into the metal shell through a sealing ring on the top, and an EFPI is formed by the endface of the optical fiber and a mirror mounted on an Invar slide block inside the shell. When the measurement handgrip pushes the slide block, the cavity length of the EFPI will change due to the inclination of the mirror, resulting in the free spectral range (FSR) change in the interference spectrum. The sensor is packaged and protected in a metal shell made of Invar. The displacement measurement experiments show that our displacement sensor has a sensitivity of 42.68 nm/μm (change in EFPI cavity length/displacement magnitude) over a measurement range of 2.0 cm with a measurement resolution of 0.270 μm. Monitoring shrinkage during the drying/curing stage of a long square brick of mortar was performed to verify the practicability of the novel displacement sensor.

2. SENSOR DESIGN AND MEASUREMENT PRINCIPLE

A schematic drawing of the TC-EFPI based displacement sensor is shown in Figure 1. A measurement handgrip is permanently connected to a slide block on which a gold surface mirror is mounted. The mirror with a reflectivity of 99% has an angle of inclination

(α) with respect to the longitudinal axis of the slide block. The single mode fiber, used as an input-output fiber, is inserted into the cylindrical metal container shell wall through the through-hole of the sealing ring, which has the same angle of inclination (α) with respect to the vertical direction. As a result, a Fabry-Perot cavity with an air-gap is formed by the endface of the optical fiber and the mirror. When a displacement is applied to the measurement handgrip, the rigidly-connected slide block will also move, resulting in a change in the length of the FP cavity. The change in the cavity length is smaller than the displacement applied to the measurement handgrip due to the inclination of the mirror. And the change in the cavity length can be determined by analyzing the *FSR* change in the interference spectrum of the EFPI. A tension spring is positioned on the other side of the slide block. Since the measurements are made in the direction of spring compression as well as in the direction of spring de-compression, the spring enables the slide block to return back after measurement with minimal hysteresis. The spring also maintains a tension, the stiffer the spring, the smaller amount vibrations can blur the measurement position. A metal shell is used to package the sensor structure, which not only protects the EFPI but also keeps the space between the mirror and the endface of the optical fiber dust free. The measurement handgrip and the metal shell are made of Invar which has a coefficient of thermal expansion (CTE) of about 1.2×10^{-6} K^{-1}. When temperature changes, both the length of the measurement handgrip and the size of the metal shell will change due to thermal expansion effect, which could both result in changes in the cavity length of the EFPI, leading to a displacement temperature cross-talk. The temperature cross-talk caused by the thermal expansion of the measurement handgrip and the metal shell is calculated to be 9.6×10^{-8} m/℃ and 1.966×10^{-7} m/℃, respectively. However, as shown in Figure 1,

the two effects cancel out each other. Therefore, the temperature cross-talk of the sensor is the combined effect, which is 106 nm/°C. More importantly, the sensor can achieve a full temperature compensation by properly designing the length of the measurement handgrip and the size of the metal shell (e.g., with the length of the measurement handgrip of 16.4 cm and the cross-section of the rectangular part of the shell of 1.4×1.4 cm). Through a judicious choice of the angle α, it is possible to design our sensor with full temperature compensation using a shorter length of the measurement handgrip.

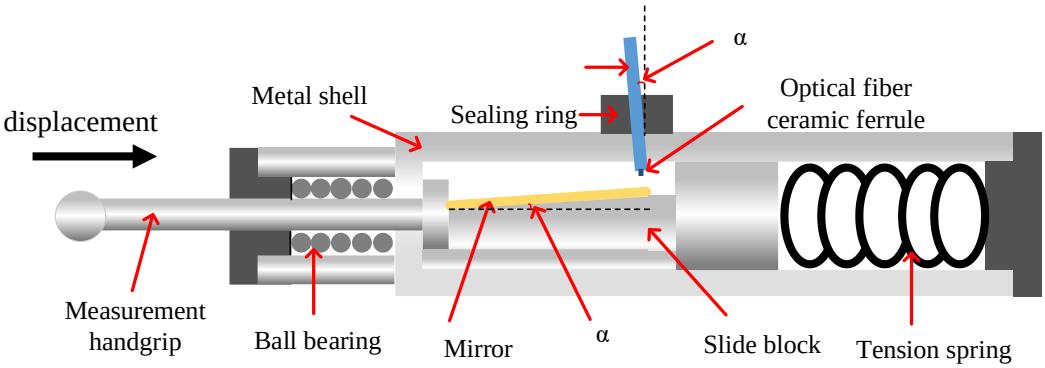

Figure 1. A schematic drawing of the TC-EFPI sensor for displacement sensing. The mirror and the input-output fiber have the same angle of inclination (α). The fiber is supported in an optical fiber ceramic ferrule, and a metal shell is used to package and protect the sensor.

As mentioned above, the endface of the optical fiber, together with the mirror form an EFPI with cavity length of L. The interference signal (I) is given by

$$I = I_1 + I_2 + 2\sqrt{I_1 I_2}\cos(\frac{4\pi nL}{\lambda} + \varphi) \quad (1)$$

where I_1 and I_2 are the light intensities reflected from the endface of the optical fiber and the mirror, respectively; φ is the initial phase difference of the interferometer; n is the

refractive index of air which is approximately 1, and L is the air cavity length [17]. The space between two successive minima of the spectrum, defined as the free spectral range (FSR), can be expressed as

$$FSR = \frac{\lambda^2}{2L} \tag{2}$$

where λ is the wavelength of the propagated light. So, the cavity length can be demodulated by determining the FSR of the interference spectrum. When the measurement handgrip experiences a displacement w, the slide block will have the same displacement in the same direction, resulting in a change ΔL of cavity length which can be determined by

$$\Delta L = \frac{\lambda^2 \Delta FSR}{2FSR_1 FSR_2} \tag{3}$$

where FSR_1, FSR_2 are the values of FSR before and after displacement. According to the geometry relationship, the displacement of the measurement handgrip can be calculated according to

$$w = \frac{\Delta L}{\sin \alpha} \tag{4}$$

horizontal direction ($0° < \alpha < 90°$). Importantly, $(\sin \alpha)^{-1}$ is the dynamic range amplification factor, which describes the relationship between the FP cavity length and the displacement applied to the measurement handgrip. Obviously, the actual external displacement is effectively contracted and transferred to the variation of cavity length of the EFPI by the triangle geometry-based displacement transfer mechanism. Moreover, the displacement measurement range of the sensor can be easily adjusted by changing the inclination of the reflective mirror and correspondingly changing the orientation of the endface of the optical

fiber, making sure that they maintain a parallel relationship. For example, a displacement measurement range of 10 cm could be realized by designing a mirror for the sensor with an inclination of 0.49°.

3. EXPERIMENTAL RESULTS AND DISCUSSIONS

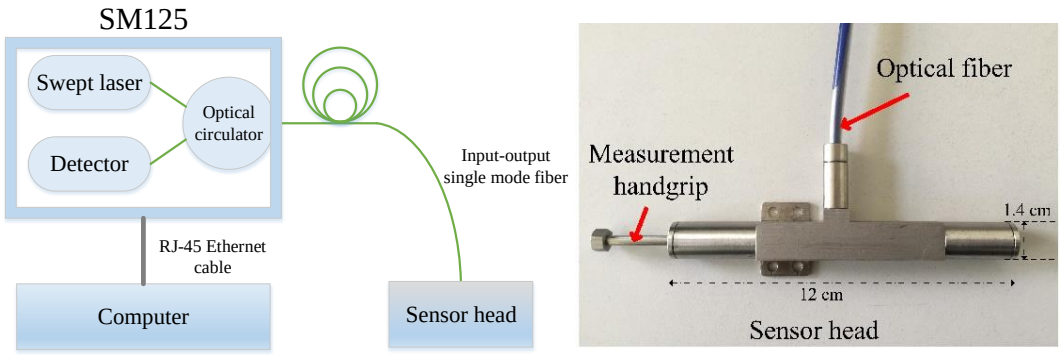

(a) (b)

Figure 2. Schematic of the experimental setup and photograph of the prototype sensor. (a) Schematic diagram of the experimental setup. Micron Optics SM125 is used as the source and demodulation device. A personal computer is used to analyze the interference spectra. (b) A photograph of the TC-EFPI based sensor for displacement measurements. The protective metal shell and the measurement handgrip are made of Invar, and the length of the main part of the metal shell is about 12 cm. The cross-section of the rectangular part of the shell is 1.4×1.4 cm. The measurement handgrip is fully extended by 2.0 cm.

The experiment setup for a 2.0 cm-range of displacement measurements is illustrated in Figure 2(a). A wavelength interrogator (Micron Optics SM125) is used as the demodulation device, which includes a swept laser source and an optical detector. The light emitted from the swept fiber laser (tuning range from 1510 nm to 1590 nm) is coupled into

the input-output fiber and then propagates to the TC-EFPI based displacement sensor through an optical circulator. Then, the optical signal modulated by the FP cavity travels back to the interrogator via the input-output fiber again. A personal computer is connected to the interrogator using an RJ-45 Ethernet Cable. Bi-directional communication between the computer and the SM125 follows the TCP/IP protocol, and is used to set acquisition parameters, acquire the data, and record the data. A personal computer is used to calculate the interference spectra. The cavity length of the FPI can then be calculated using a LabVIEW-based data processing program. A photograph of our TC-EFPI based displacement sensor is shown in Figure 2(b).

Figure 3(a) shows the interference spectra of the TC-EFPI sensor for four different displacements. Fourier transform was applied to the interference spectra and the results are shown in Figure 3(b). In our experiments, the applied displacements were precisely positioned by a Mitutoyo micrometer with a resolution of 0.1 μm and a dynamic range of 25 mm. Obviously, the *FSRs* of the spectra decrease with increasing displacements, which is consistent with (2)(4). As shown in Figure 3(b), the amplitude of the peak decreases with increasing displacement. This is because the amplitude is related to the fringe visibility of the interferogram, which decreases as a function of cavity length. When the displacement increases, the cavity length will increase, too. It should be noted that using a collimator (e.g., a graded-index fiber with a quarter-pitch length) at the tip of the optical fiber or using an endface partically-coated optical fiber can improve the fringe visibility and signal-to-noise ratio (SNR) of the sensor.

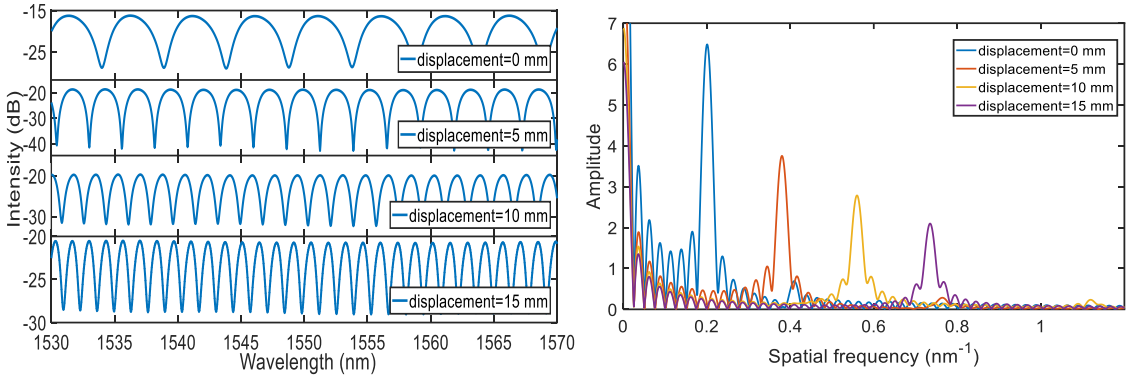

(a) (b)

Figure 3. Wavelength- and frequency-domain spectra obtained from the sensor. (a) Interference spectra of the TC-EFPI sensor for four different displacement measurements: 0 mm, 5 mm, 15 mm, and 20 mm. (b) corresponding spatial spectra of the EFPI sensor for four displacement measurements.

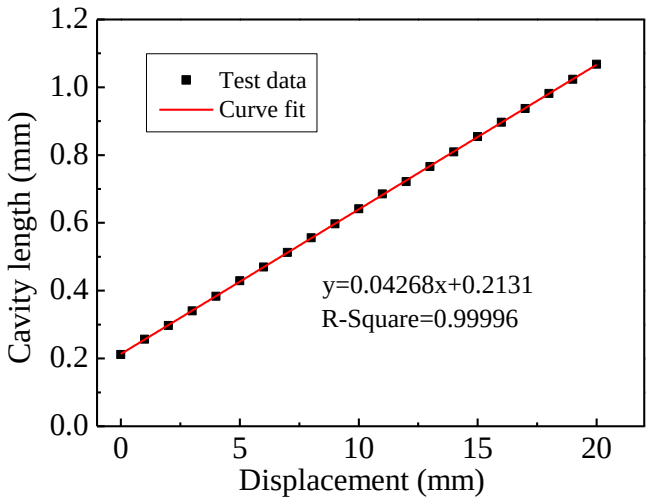

Figure 4. Measured cavity length as a function of the applied displacement. A linear fitting is applied to the experimental results. The fitting results show a good linear relation between the cavity length change and displacement, which matches well with the mathematical model (4).

The experimentally measured relationship between cavity length and displacement of our TC-EFPI based sensor is shown in Figure 4. According to the

mathematical model described in Equation (4), the relationship between the change in cavity length and the displacement of the measurement hand grip should be linear. So, a linear fitting was applied to the experimental results. The value of R-Square is 0.99996, indicating that the demodulated cavity length and the applied displacement do have a good linear relationship. From the slope of the fitted line, the sensitivity of the sensor was determined to be about 42.68 nm/μm over a dynamic range of 2.0 cm.

An experiment was also performed to quantify the long-term measurement resolution stability of the proposed sensor. The interferograms of the sensor for a fixed displacement were continuously recorded in a temperature controlled box (±1 ℃, KEEN BING) for more than 5 hours. The standard deviation of the EFPI cavity length after Fourier transform to the interferograms was calculated to be ± 5.8 nm, corresponding to a displacement uncertainty of ± 0.135 μm. In principle, the demodulated cavity length of a standard EFPI can be resolved typically to 1 nm. For our prototype sensor, the resolution is 24 nm based on (4). The machining and the assembly of our prototype sensor resulted in a measurement uncertainty of 11.6 times larger than the theoretical resolution. We considered this quite reasonable given that standard machining and assembly methods for building the prototype sensor were used. The designed sensitivity of our sensor is 40 nm/μm, resulting in a difference of 6.7% between the designed and the measured sensitivity (42.68 nm/μm). This uncertainty can be explained by the small inaccuracies in the assembly of the mirror in the metal shell and the orientation of the optical fiber. The assembly error is inconsequential because the sensor will be calibrated (see Figure 4). However, the performance of the sensor is critically dependent on the displacement temperature cross sensitivity. The response of the displacement sensor to variations in

temperature was investigated. The displacement temperature cross sensitivity was found to be around 100 nm/℃, which corresponds closely to the calculated value from the orthogonal geometric design.

To verify the practicability of our sensor, an experiment for monitoring the shrinkage during the drying/curing stage of a long square brick of mortar was conducted. In the experiment, the mortar was prepared using cement (Sakrete Portland Type-I), tap water, and sand with a weight ratio of 1:0.5:2.81. The size of the long square brick of mortar was 25.4×2.54×2.54 cm. The test was initiated after the mortar cured for one day. During this process, a rigid attachment between one end of the brick of mortar and the steel block was formed due to the bond between a roughened steel bar fixed to the steel block and the mortar. After that, the measurement handgrip was pre-compressed and attached to the steel block, and the metal shell of the sensor was fixed. When the mortar experienced a shrinkage along the long axis of the brick of mortar, the steel block moved, too, thus the measurement handgrip of the sensor also experienced a displacement due to the decompression of the spring inside the metal shell, which then could be measured by the sensor. The schematic diagram of the experiment setup is shown in the inset of Figure 5.

Figure 5 presents the experimental results for monitoring shrinkage of the long square brick of mortar. The shrinkage strain is the ratio of the measured displacement to the initial length of the long square brick of mortar in the direction of the measurement (i.e. 25.4 cm). The measured strain results matched well with [20]. The displacement monitoring experiment lasted for one month. As shown in Figure 5, our sensor can continuously function in a stable manner for a prolonged period of time, which is quite important for practical applications.

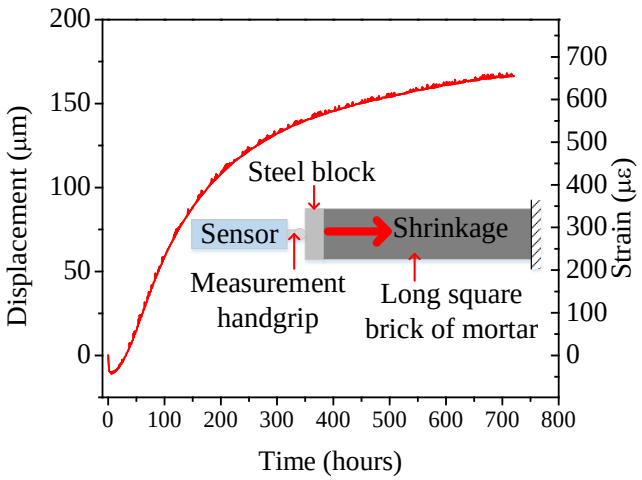

Figure 5. Continuous displacement measurement results and shrinkage strain along the direction of the displacement measurement, as a function of time. The inset is the schematic diagram of the experiment setup. The long square brick of mortar was prepared using cement (Sakrete Portland Type-I), tap water, and sand with a weight ratio of 1:0.5:2.81, and the size was 25.4×2.54×2.54 cm. The measurement handgrip of the sensor was pre-compressed and attached to the mortar by a steel block before conducting the experiment.

4. CONCLUSIONS

We invented, designed, constructed, and tested a low cost and stable TC-EFPI based optical fiber sensor for displacement measurements. In our sensor, an inclined mirror, mounted on a translational stage, combines with the endface of a single mode fiber, supported in a fiber ceramic ferrule, to form a Fabry-Perot cavity. The external displacement information can be determined by deducing the variations in the cavity length of the Fabry-Perot interferometer. A user-configurable displacement transfer mechanism based on a triangle geometry is employed in our sensor, which makes the sensor capable of a wide range of displacement measurements, up to dimensions of several centimeters. A metal shell is used to package and protect the sensor. In comparison with other

displacement sensors, our displacement sensor can realize displacement measurements with a resolution of 0.270 μm over a wide measurement range of 2.0 cm. An experiment designed to monitor the shrinkage of a long square brick of mortar during the drying/curing stage was performed to verify the practicability of our sensor. The metal shell and the measurement handgrip were made of Invar which has a small CTE, and the novel mechanical design achieves temperature compensation, leading to a low temperature cross-talk for the TC-EFPI sensor. This low-cost and robust TC-EFPI based sensor with centimeter dynamic range and submicrometer resolution can be easily commercialized and has great potential for applications in the chemical-oil industry, construction industry, and other industries with harsh environments. In addition to displacement measurements reported in this letter, the same flexible working principle can be designed to measure other physical quantities such as inclination, pressure, strain, etc.

REFERENCES

[1] S. Khaliq, W. J. Stephen, and P. T. Ralph. "Fiber-optic liquid-level sensor using a long-period grating," *Opt. Letters*, vol. 26, pp. 1224-1226, Aug. 2001.

[2] B. F. Yun, C. Na, and Y. P. Cui. "Highly sensitive liquid-level sensor based on etched fiber Bragg grating." *IEEE photonics technology letters*, vol. 19, pp. 1747-1749, Oct. 2007.

[3] B. Vikram and M. V. Ashish, "Optical fiber long-period grating sensors," *Opt. Letters*, vol. 21, pp. 692-694, May. 1996.

[4] J. Zhang, X. L. Tang, J. H. Dong, T. Wei, and H. Xiao. "Zeolite thin film-coated long period fiber grating sensor for measuring trace organic vapors." *Sensors and Actuators B: Chemical*, vol. 135, pp 420-425, Jan. 2009.

[5] Y. N. Zhang, *et al*. "High-temperature fiber-optic Fabry–Perot interferometric pressure sensor fabricated by femtosecond laser." *Optics letters*, vol. 38, pp. 4609-4612, Nov. 2013.

[6] Y. Gong, T. Zhao, Y. J. Rao, and Y. Wu. "All-fiber curvature sensor based on multimode interference." *IEEE Photonics Technology Letters*, vol. 23, pp. 679-681, Jun. 2011.

[7] J. N. Dash, *et al*. "Nano-displacement sensor based on photonic crystal fiber modal interferometer." *Optics letters*, vol. 40, pp. 467-470, Feb. 2015.

[8] Y. Zhu, *et al*. "Temperature insensitive measurements of static displacements using a fiber Bragg grating," *Opt. Express*, vol. 11,pp. 1918–1924, Aug. 2003.

[9] Y. Wang, *et al.*, "A tilt sensor with a compact dimension based on a long-period fiber grating," *Rev. Sci. Instrum.*, vol. 82, pp. 0931061-09310614, Sep. 2011.

[10] S. C. Jiang, *et al*. "A novel wide measuring range FBG displacement sensor with variable measurement precision based on helical bevel gear." *Optoelectronics Letters*, vol. 11, pp. 81-83, March. 2015.

[11] J. P. Chen, J. Zhou, and Z. H. Jia. "High-sensitivity displacement sensor based on a bent fiber Mach–Zehnder interferometer." *IEEE Photonics Technology Letters*, vol. 25, pp. 2354-2357, Dec. 2013.

[12] Y. Bai, *et al*. "All fiber Fabry–Pérot interferometer for high-sensitive micro-displacement sensing." *Optical and Quantum Electronics*, vol. 48, pp. 1-10, Feb. 2016.

[13] Q. Wu, M. H. Agus, P. F. Wang, Y. L. Y, *et al*. "Use of a bent single SMS fiber structure for simultaneous measurement of displacement and temperature sensing." *IEEE Photonics Technology Letters*, vol. 23, pp. 130-132, Jan. 2011.

[14] Q. Z. Rong, *et al*. "In-fiber quasi-Michelson interferometer with a core–cladding-mode fiber end-face mirror." *Applied optics*, vol. 52, pp. 1441-1447, Mar. 2013.

[15] M. Bravo, *et al*. "High precision micro-displacement fiber sensor through a suspended-core Sagnac interferometer." *Optics letters*, vol. 37, pp. 202-204, Jan. 2012.

[16] B. H. Lee, *et al*. "Interferometric fiber optic sensors." *Sensors*, vol. 12, pp. 2467-2486, Feb. 2012.

[17] X. L. Zhou, Q. X. Yu. "Wide-range displacement sensor based on fiber-optic Fabry–Perot interferometer for subnanometer measurement." *IEEE sensors journal*, vol. 11, pp. 1602-1606, Jul. 2011.

[18] Z. Chen, L. Yuan, G. Hefferman, T. Wei. "Ultraweak intrinsic Fabry–Perot cavity array for distributed sensing." *Optics letters*, vol. 40, pp. 320-323, Feb. 2015.

[19] J. Huang, X. Lan, M. Luo, H. Xiao. "Spatially continuous distributed fiber optic sensing using optical carrier based microwave interferometry." *Optics express*, vol. 22, pp. 18757-18769, Jul. 2014.

[20] Al-Saleh, Saleh A., and Rajeh Z. Al-Zaid. "Effects of drying conditions, admixtures and specimen size on shrinkage strains." *Cement and concrete research*, vol. 36, pp. 1985-1991, Oct. 2006.

II. AN OPTICAL INTERFEROMETRIC TRIAXIAL DISPLACEMENT SENSOR FOR STRUCTURAL HEALTH MONITORING: CHARACTERIZATION OF SLIDING AND DEBONDING FOR A DELAMINATION PROCESS

ABSTRACT

This paper presents an extrinsic Fabry–Perot interferometer-based optical fiber sensor (EFPI) for measuring three-dimensional (3D) displacements, including interfacial sliding and debonding during delamination. The idea employs three spatially arranged EFPIs as the sensing elements. In our sensor, the three EFPIs are formed by three endfaces of three optical fibers and their corresponding inclined mirrors. Two coincident roof-like metallic structures are used to support the three fibers and the three mirrors, respectively. Our sensor was calibrated and then used to monitor interfacial sliding and debonding between a long square brick of mortar and its support structure (i.e., a steel base plate) during the drying/curing process. This robust and easy-to-manufacture triaxial EFPI-based 3D displacement sensor has great potential in structural health monitoring, the construction industry, oil well monitoring, and geotechnology.

1. INTRODUCTION

Over the years, steel-reinforced concrete (RC) has been extensively used in civil infrastructures [1]. Throughout the life cycle of a reinforced concrete structure, many issues must be properly addressed to assess the safety and serviceability of the structure [2].

The interfacial bonding between the concrete and steel is always a concern. The debonding due to shrinkage of concrete or corrosion of steel can decrease the tensile

strength and ductility of the RC, leading to a catastrophic failure of the structures [3]. Additionally, the relative sliding (horizontal and vertical directions) between the concrete and steel, yielded by the insufficient shear bond strength and irregular deformation, can directly destroy the integrity of RC, causing deterioration of the interior stress state [4]. Therefore, it is very important to detect both sliding and debonding in RC in time to ensure its safety and determine its fitness for service. A number of sliding and debonding sensors have been developed with various sensing mechanisms, primarily including mechanical, electrical, and acoustic [1–3,5–7]. Acoustic emission (AE) is one of the most powerful tools to assess the integrity of the RC structure, which correlates the AE parameters with the localized changes inside the structure [5]. Another widely used technique is the piezoelectric-based approach, which is based on impedance analysis or comparisons of vibration-characteristics [8]: the operational principle of the first method is based on the electromechanical coupling properties of piezoelectric materials; the latter method employs piezoelectric transducers to actively excite and sense the vibrational characteristics of the structure, and then compares the vibrational signatures with those of a healthy-state structure. However, these kinds of sensors have demanding requirements for a stable and interference-free working environment. For instance, large temperature fluctuations, strong electromagnetic interference, and other harsh environmental factors can have significant detrimental influences on the performance of these sensors.

In recent years, optical fiber sensors have attracted considerable attention and have been widely used for structural health monitoring (SHM) [9,10]. In comparison to traditional sensing technologies, optical fiber sensors offer great advantages, such as immunity to electromagnetic field, high sensitivity, small size, ease of fabrication, and

robustness to harsh environments [11–14]. Given several choices of sensing mechanisms, such as wavelength modulation, phase modulation, and intensity modulation, optical fiber displacement sensors thrive on structural diversity and sensing properties [15–24]. The majority of the reported optical fiber displacement sensors work in a one-dimensional fashion, meaning it is impossible to measure interfacial sliding and debonding at the same time [15–20]. Several two- and three-dimensional (2D, 3D) optical fiber displacement sensors have been demonstrated [21–23]. Zhu et al. developed fiber Bragg grating (FBG) sensing bars for monitoring internal displacements of a 2D model dam [21]. Rapp et al. reported a displacement field estimation for a 2D structure using fiber Bragg grating sensors [23]. Despite the great efforts that have been made in the development of multidimensional optical fiber displacement sensors, accurate measurements of interfacial sliding and debonding still remain a great challenge. This is because the aforementioned multidimensional sensors operate based on the modal transformation method to reconstruct displacements from measured strains [23]. What these sensors can measure is the deformation of one object (e.g., the concrete), rather than the relative displacements between two objects (e.g., between concrete and steel), both of which can deform. Therefore, the sliding and debonding cannot be accurately determined at the same time.

An extensively studied interferometric sensor, the extrinsic Fabry–Perot interferometer (EFPI), has the merit of measuring displacements. An EFPI is generally formed by the endface of an optical fiber and an external reflecting surface [24]. The distance between the two reflecting surfaces can directly affect the reflection spectrum of an EFPI [24]. With proper structure design and packaging, EFPI sensors could be

considered excellent candidates for accurately measuring displacements [14,18,24,25].

In this paper, we demonstrate a stable triaxial EFPI-based optical fiber sensor for 3D relative displacement measurements, including interfacial sliding and debonding, useful for describing the delamination process. In our sensor design, two roof-like metallic structures are used to support the optical fibers and mirrors, ensuring that the endfaces and their corresponding mirrors are parallel. Three EFPIs are formed by the endfaces of optical fibers and their corresponding mirrors. When there are 3D relative displacements between the two roof-like metallic structures, the cavity lengths of the EFPIs will change correspondingly. Our sensor was firstly calibrated to determine the cavity length-displacement coefficient matrix for the sensor. Then, the utility of the triaxial displacement sensor was demonstrated by monitoring interfacial sliding and debonding between a sample of mortar and a steel base plate during the drying/curing process of the mortar.

2. SENSOR STRUCTURE AND PRINCIPLE

A schematic drawing of the sensor is illustrated in Figure 1, including the optical fiber and mirror components, each of which is fixed to a separate roof-like supporting body. The fiber component consists of three optical fibers and their supporting body, and the mirror component consists of three mirrors and their supporting body. The two roof-like supporting bodies can move independently in the 3D domain. The inclined mirror surfaces S_1, S_2, and S_3 have angles of inclination θ_1, θ_2, and θ_3 ($0° < \theta_1, \theta_2, \theta_3 < 90°$) with respect to the *XOY* plane, respectively. The flat metal surfaces of the mirror component are each

coated with a gold layer with a thickness of approximately 600 nm using the Thermal Evaporation Deposition method, each mirror achieving a reflectivity of 99%. The size of each mirror is approximately 10 mm^2. The endfaces of the optical fibers are parallel to the corresponding mirrors. As a result, three EFPIs are formed by the endfaces of three optical fibers and their corresponding mirrors.

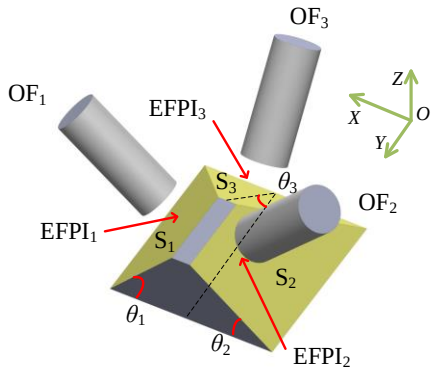

Figure 1. A schematic diagram of the triaxial displacement sensor. The sensor consists of an optical fiber component and a mirror component. OF represents optical fiber. Three EFPIs are formed by the endfaces of the three optical fibers and their corresponding mirrors. The inclined surfaces S_1, S_2, and S_3 have angles of inclination θ_1, θ_2, and θ_3 ($0° < \theta_1, \theta_2, \theta_3 < 90°$) with respect to the *XOY* plane, respectively. A 3D coordinate system, *XYZ*, is defined in the figure.

According to the established geometric relationships, the relative displacements in a 3D domain between the optical fiber component and the mirror component can be effectively compressed and transferred to variations of cavity lengths of the formed EFPIs. For instance, when there is a relative sliding along the *X* direction, the cavity lengths of $EFPI_1$ and $EFPI_2$ will change. The displacements Δx, Δy, and Δz of the optical fiber component with respect to the mirror component in a 3D domain can be calculated by

$$\begin{Bmatrix} \Delta x \\ \Delta y \\ \Delta z \end{Bmatrix} = \begin{bmatrix} \sin\theta_1 & 0 & \cos\theta_1 \\ -\sin\theta_2 & 0 & \cos\theta_2 \\ 0 & -\sin\theta_3 & \cos\theta_3 \end{bmatrix}^{-1} \begin{Bmatrix} \Delta L_1 \\ \Delta L_2 \\ \Delta L_3 \end{Bmatrix} \quad (1)$$

where ΔL_1, ΔL_2, and ΔL_3 are the changes in the cavity lengths of the three EFPIs, respectively. It should be noted that the cavity length-displacement coefficient matrix should be adjusted if the 3D coordinate system is changed. Since all three EFPIs function based on the same principle, we will only discuss the sensing and demodulation mechanism for one of them (e.g., $EFPI_1$).

As stated, $EFPI_1$ with a cavity length of L_1 is formed by the endface of OF_1 and the mirror mounted on S_1. An interference pattern is generated by the two reflected beams. The intensity for the superposition of the two waves, the interference signal I_1, is given by

$$I_1 = I_{11} + I_{12} + 2\sqrt{I_{11} I_{12}} \cos(\frac{4\pi L_1}{\lambda} + \varphi) \quad (2)$$

In Equation (2), I_{11} and I_{12} denote the reflected light intensities from the endface of OF_1 and the corresponding mirror S_1, respectively; φ is the initial phase difference of the interferometer. The difference in wavelength between two successive minima in the spectrum, defined as the free spectral range (*FSR*) [26], can then be expressed as

$$FSR_1 = \lambda_{1b} - \lambda_{1a} = \frac{\lambda_{1a}\lambda_{1b}}{2L_1} \quad (3)$$

where λ_{1a} and λ_{1b} are the wavelengths corresponding to the two peak points in the interference spectrum of $EFPI_1$; FSR_1 is the *FSR* of the interference spectrum of $EFPI_1$; L_1 is the cavity length of $EFPI_1$. According to Equation (3), the cavity length L_1 can be calculated. With reference to the demodulation principle described above, variations in the

cavity lengths of the three EFPIs can be determined. Therefore, the displacements in the 3D domain can be calculated by Equation (1). It should be noted that a displacement transfer mechanism is employed in the sensor design [14]. The user-configurable, triangle-geometry-based displacement transfer mechanism provides a means for adjusting the inclination of the mirrors to specify the dynamic range for each of the three displacement sensors and is described in detail in [14].

3. EXPERIMENTAL RESULTS AND DISCUSSIONS

3.1. SENSOR CHARACTERIZATION

The structure of the triaxial displacement sensor is shown in Figure 2(a). Three optical fibers, mounted in ceramic ferrules, are inserted into a roof-like metal shell component through the holes on the three sloping sides, respectively. Three gold surface mirrors are mounted on a similar roof-like metal shell component, which is underneath the optical fiber metal shell component. As a result, three EFPIs with air-gaps are formed by the endfaces of the optical fibers and corresponding mirrors. The sensor structure is packaged in a metal shell, which protects the space containing the EFPIs dust-free. The metal base support is used to fix the mirror component. Figure 2(b) presents a photograph of our triaxial displacement sensor. Our triaxial sensor provides high measurement resolution, up to a level of tens of nanometers. The fiber component and the mirror component can be embedded in or attached to different adjacent objects (e.g., mortar and steel plate) for measuring 3D relative displacements between the different structural elements.

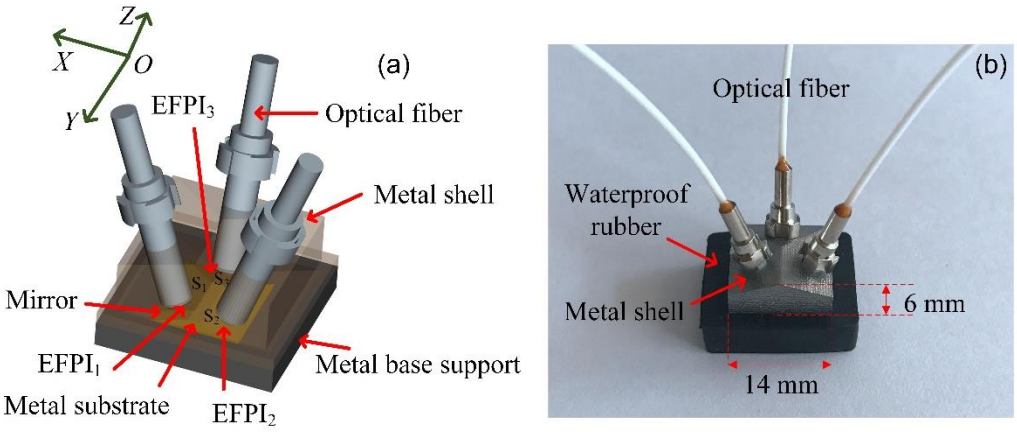

Figure 2. Three-dimensional rendering and photograph of the sensor. (a) Three-dimensional rendering of the triaxial sensor model for 3D relative displacement sensing. The mirrors and endfaces of the corresponding optical fibers are parallel, such that three EFPIs are formed. Both the optical fibers and mirrors are supported on separate roof-like structures. (b) A photograph of the sensor. The sensor is packaged and protected by a metal shell and a waterproof rubber casing. The size of the metal shell is 14 mm × 14 mm × 6 mm.

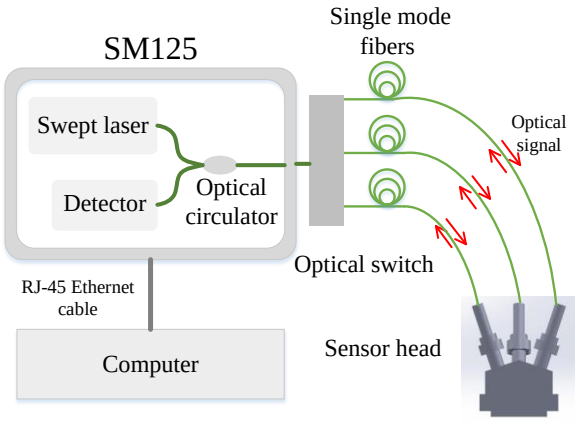

Figure 3. A schematic diagram of the experimental setup. Three input–output channels are connected to the three single mode fibers, which terminate and form three EFPIs in the sensor head. An integrated optical switch is used for rapid switching between EFPIs.

The experimental setup used for the calibration of the triaxial displacement sensor is illustrated in Figure 3. A wavelength interrogator/demodulator (SM125, Micron Optics,

Inc., Atlanta, GA USA) is used as the light source, detector, and demodulator. The interrogator has four optical channels and an internal optical switch that allows computer-controlled switching between the four channels. The incident light beam from the swept laser is directed to each of the EFPI sensors in a continuous round-robin sequence by the optical switch. The reflected interference signal described by Equation (2) consists of a reflected beam from the end face of the optical fiber and a reflected beam from the corresponding inclined gold mirror. The interference signal is routed through the optical circulator to the detector. The interference spectrum is obtained by sweeping the wavelength of the laser from 1510 to 1590 nm in equal intervals (i.e., 0.005 nm) and by recording the corresponding intensities of the reflected signals. The update rate of the interrogation unit can be up to 1 Hz. A personal computer is connected to the interrogator using an RJ-45 Ethernet (Micron Optics, Inc., Atlanta, GA USA) cable. Bi-directional communication between the computer and the SM125 follows the TCP/IP protocol, and is used to set acquisition parameters, acquire the data, and store the data. The personal computer is also used to process the interference spectra. The cavity length of each of the EFPIs can then be determined using a LabVIEW-based data processing program employing the demodulation mechanism described in [25]. It should be noted that an intensity-based demodulation system can also be used for the proposed sensor. If a single-wavelength light source is used, the output intensity of the reflected wave will be a sinusoidal function of the cavity length, which is the superposition of the two light beams, one reflected by the optical fiber endface and the other by the corresponding mirror. However, the measurement range of the single-wavelength light source based intensity

system will be limited—less than a wavelength (i.e., 1.5 μm)—since the linear response region of the sensor will be the rising/falling curve of the sinusoidal function.

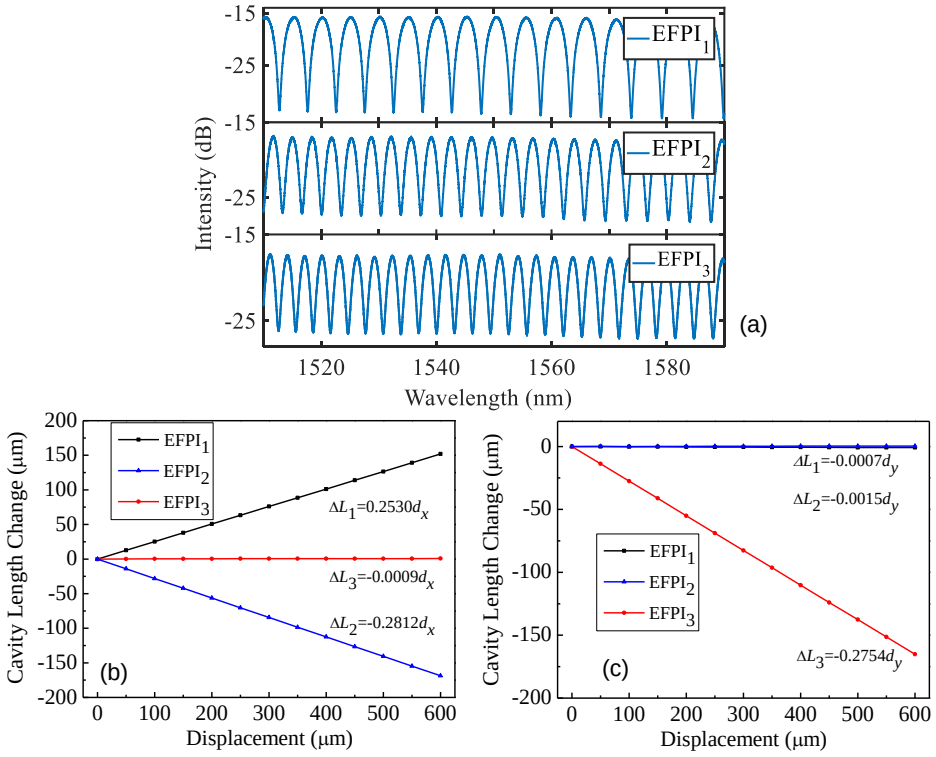

Figure 4. Calibration results of the triaxial displacement sensor. (a) Interference spectra recorded from the triaxial displacement sensor for the initial cavity length settings. (b) The changes in cavity lengths of the three EFPIs as a function of applied displacements along the *X* direction (d_x). (c) The changes in cavity lengths of the three EFPIs as a function of applied displacements along the *Y* direction (d_y). In the experiment, the mirror component was fixed on an optical table, and the optical fiber component was positioned by an optical stage. The coordinate system used in the experiment is the same as the *XYZ* system shown in Figure 2(a).

Figure 4(a) shows the interference spectra of the triaxial sensor at the initial cavity length settings. The initial cavity lengths of the three EFPIs were 233.725 μm, 338.913 μm, and 381.935 μm, respectively. We report results for displacement calculations that contain six significant figures because an EFPI can typically resolve a 1 nm change in cavity length.

In our calibration experiment, the mirror component was fixed on an optical table, and the optical fiber component was positioned using an optical translation stage. The calibration experiment was conducted at room temperature. The coordinate system used in the experiment was the same as that shown in Figure 2(a). Displacements along the *X* and *Y* directions (d_x, d_y) were applied to the optical fiber component of the sensor. The magnitudes of the applied displacements were accurately determined using a Mitutoyo micrometer (resolution, 0.1 μm; dynamic range, 25 mm) [14]. The relationships between the displacements and the corresponding changes in cavity lengths of the EFPIs for a sequence of changes along the two different directions are shown in Figure 4(b) and Figure 4(c). The results matched well with theoretical expectations. When the optical fiber component of the sensor was subjected to a displacement along the *X* direction, the cavity lengths of $EFPI_1$ and $EFPI_2$ changed in opposite directions while that of $EFPI_3$ did not change. On the contrary, when the optical fiber component moved along the *Y* direction, the cavity length of $EFPI_3$ varied with the applied displacement, while the cavity lengths of $EFPI_1$ and $EFPI_2$ remained constant. The small differences between the theoretical and experimental results are ascribed to machining errors for the flatness of the sloping sides of the mirror component of the sensor. According to the calibration results shown in Figure 4(b) and Figure 4(c), the inclinations of the three mirrors were calculated to be 14.656°, 16.332°, and 15.987°, respectively. The dynamic ranges in the *X*, *Y*, and *Z* directions of the sensor are designed to be ±1.5 mm, ±1.5 mm, and 1.0 mm, respectively. As mentioned above, the dynamic ranges can be flexibly modified by designing the inclinations of the three mirrors and the package size of the sensor. The coefficient matrix in Equation (1) that describes the relationships between changes in the cavity lengths and

the corresponding 3D displacements for the sensor is calculated to be

$$\begin{bmatrix} 0.2530 & 0 & 0.9675 \\ -0.2812 & 0 & 0.9596 \\ 0 & -0.2754 & 0.9613 \end{bmatrix}^{-1}.$$

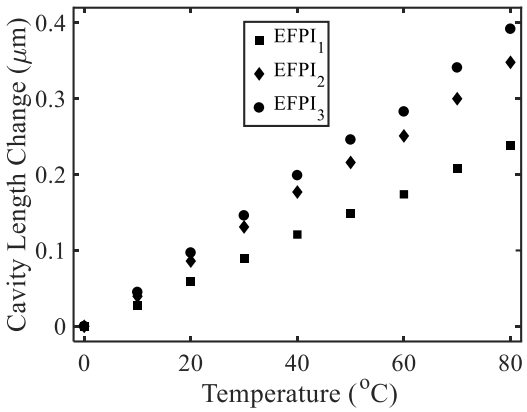

Figure 5. Measured cavity length change of $EFPI_1$, $EFPI_2$, and $EFPI_3$ with respect to temperature.

The temperature response of the triaxial displacement sensor was also investigated by placing the sensor in a temperature-controlled box (±1 °C, KEEN BING) [14]. The measured temperature response of the sensor is shown in Figure 5. Linear curve fits were applied to the three measured data sets, and the results showed that the temperature sensitivities of the $EFPI_1$, $EFPI_2$, and $EFPI_3$ were 0.00298 μm/°C, 0.004314 μm/°C, and 0.00488 μm/°C, respectively. The three slopes for a 1 °C change are fairly small compared to the cavity lengths of the three EFPIs. However, in field applications where the ambient temperature could change by tens of degrees, the temperature influence on the sensor for displacement measurements should be compensated. For instance, an FBG could be

inserted in the lead-in single-mode fiber for real-time compensation of changes in the cavity lengths due to temperature fluctuations. The corrections to the cavity lengths of the three EFPIs would be based on the measured temperature dependence coefficients.

3.2. SENSOR TESTING

To demonstrate the practicability of the sensor, an experiment designed to monitor the interfacial sliding and debonding between a long square brick of mortar and a steel base plate during the drying/curing process of the mortar was conducted. The schematic diagram of the experiment is shown in Figure 6(a). For the experiment, the mortar was prepared using cement (Sakrete Portland Type-I), tap water, and sand with a weight ratio of 1.0:0.5:2.81. The size of the long square brick of mortar was 25.40 × 2.54 × 2.54 cm. Prior to conducting the test experiment, a square section, 2 cm by 2 cm and 3 mm deep, was machined on the top of the steel base plate, which was used to mount and fix (using a machine screw) the mirror component of the sensor. It is important that the top surface plane of the metal base support of the mirror component matches the top surface plane of the steel plate for accurate measurement of interfacial sliding and debonding. The optical fiber component was mounted right above the mirror component, and a waterproof rubber cover was used to protect the sensor structure, as shown in Figure 6(a). The next step was to pour the cement. As a result, the mirror component (fixed to the steel plate with a machine screw) shared a common surface with the steel plate, while the optical fiber component was integrated within and bonded to the concrete. Thus, the relative displacements between the concrete and the steel base plate could be measured by our sensor. We added a thin film of oil between the brick of mortar and the steel base plate to

ensure weak interfacial bonding. The experiment began after the mortar was cured for one day. During the initial curing period, one end of the brick of mortar was rigidly bonded to the vertical steel side plate using two roughened steel rods fixed to the vertical steel side plate and protruding into the brick of mortar, as shown in Figure 6(a).

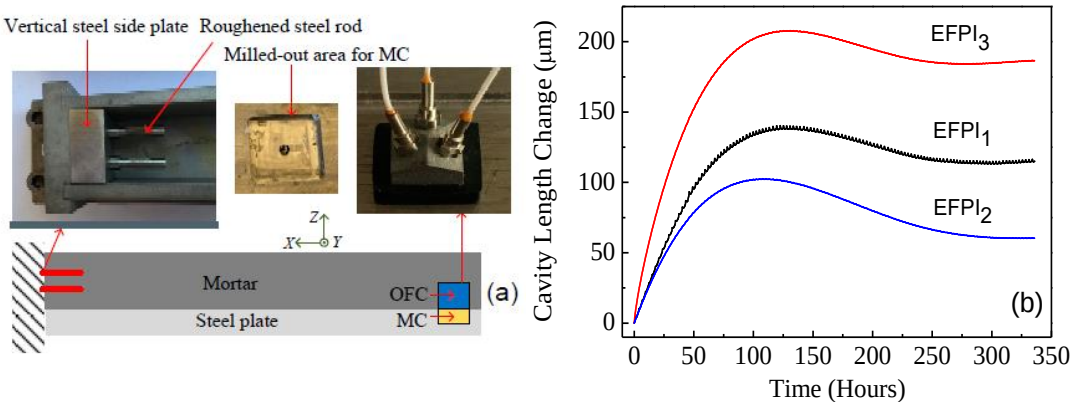

Figure 6. Continuous displacement measurements. (a) The schematic diagram of the experiment setup for monitoring delamination and sliding. Note that the mirror component (MC) is embedded in a milled-out square area that is 3 mm deep so that the top surface of the metal base support of the MC matches the top surface of the steel plate. (b) Cavity length changes as a function of time from three EFPIs during continuous displacement measurements for a brick of mortar during the drying/curing process. OFC and MC represent the optical fiber component and the mirror component, respectively. Mortar components and weight ratios: Sakrete Portland Type-1 cement, 1.0; tap water, 0.5; sand, 2.8. Brick of mortar size: 254.0 mm × 25.4 mm × 25.4 mm.

Figure 6(b) presents the experimental results for monitoring the interfacial sliding and debonding between the long brick of mortar and the steel base plate. During the mortar shrinkage process, the relative 3D displacements were metered by our sensor and interpreted as interfacial sliding along the *X* direction, buckling along the *Y* direction, and debonding along the *Z* direction between the brick of mortar and the steel base plate. The monitoring experiment lasted for 14 days. Throughout the period of the experiment, the

mortar/steel structure was contained in a temperature-controlled box. According to the experimental results presented in Figure 6(b), our sensor operated continuously for a long period of time, which is a key factor in practical applications.

Using the transformation coefficient matrix, the interfacial sliding and debonding described in the 3D domain can be calculated and plotted, as shown in Figure 7. The insets in Figure 7(a)–(c) are plots of the time derivatives of the displacements along the *X*, *Y*, and *Z* directions with respect to time, respectively. The time derivatives were calculated after a low-pass filter was applied to the displacement vs. time data for the *X*, *Y*, and *Z* directions. The displacement along the *X* direction, representing the shrinkage along the long axis of the brick of mortar, increased with time. The *X*-displacement reveals a sliding between the brick of mortar and the steel base plate. The magnitude of the displacement along the +*X* direction is due in part to the rigid interfacial bond between the vertical steel side plate and the brick of mortar. The time rate of change in the *X*-displacement peaks at approximately 43 h into the drying/curing process; we anticipate that this peak displacement rate is a function of the composition, geometry, configuration, etc. of the brick of mortar specimen. Along the negative *Y* direction, the magnitude of the displacement initially increased dramatically with time. The *Y*-displacement data reveals a buckling effect, amplified by the attachment of the brick of mortar to the vertical steel side plate. The time rate of change of the *Y*-displacement drops dramatically in the first 29 h of the drying/curing process and depicts the complex dynamics of compression buckling. The displacement along the positive *Z* direction firstly increased, then decreased, and finally flatted with time. The displacement along the positive *Z* direction represents debonding between the brick of mortar and the steel base plate. The time rate of change of the *Z*-displacement increases

rapidly and peaks in the first 12 h of the drying/curing process. Interestingly, the time rate of change in the *Z*-displacement as a function of time reveals that the debonding between the brick of mortar and the steel base plate turned negative at 119 h, meaning that the gap size between the brick of mortar and the steel base plate started collapsing. It is conceivable that the non-monotonic displacements along the *Z* direction were the consequences of combined effects from both the shrinkage of the mortar and the constant force of gravity. Beyond 300 h, the gravitational force and the shrinkage of the mortar along the *Z* direction reached a balance (note that the *X*-displacement continues to increase beyond 300 h, indicating that the drying/curing process is not yet complete). As shown in Figure 7(d), the position of the optical fiber component changed from the initial point (0, 0, 0) to the final position (101.198 μm, −354.327 μm, and 92.572 μm) at the conclusion of the experiment. The small ripples in the displacement curves were caused by the periodic temperature variations in the temperature-controlled box (±1 °C, KEEN BING), due to the regulation of refrigeration (around 2.9-h cycle), which matched well with the time interval between the two peaks of the ripples. Please note that the small ripples represent the temperature-induced fluctuations in the dimensions of the brick of mortar and the steel base plate. As can be seen, due to the long length of the concrete and base plate in the *X* direction (i.e., 25.4 cm), the amplitude of the small ripples in the *X*-displacement (i.e., Figure 7(a)) is larger than the *Y*- and *Z*-displacements. For example, a 1 °C change in temperature could induce an approximately 3 μm relative displacement in the *X* direction between the base plate and the concrete.

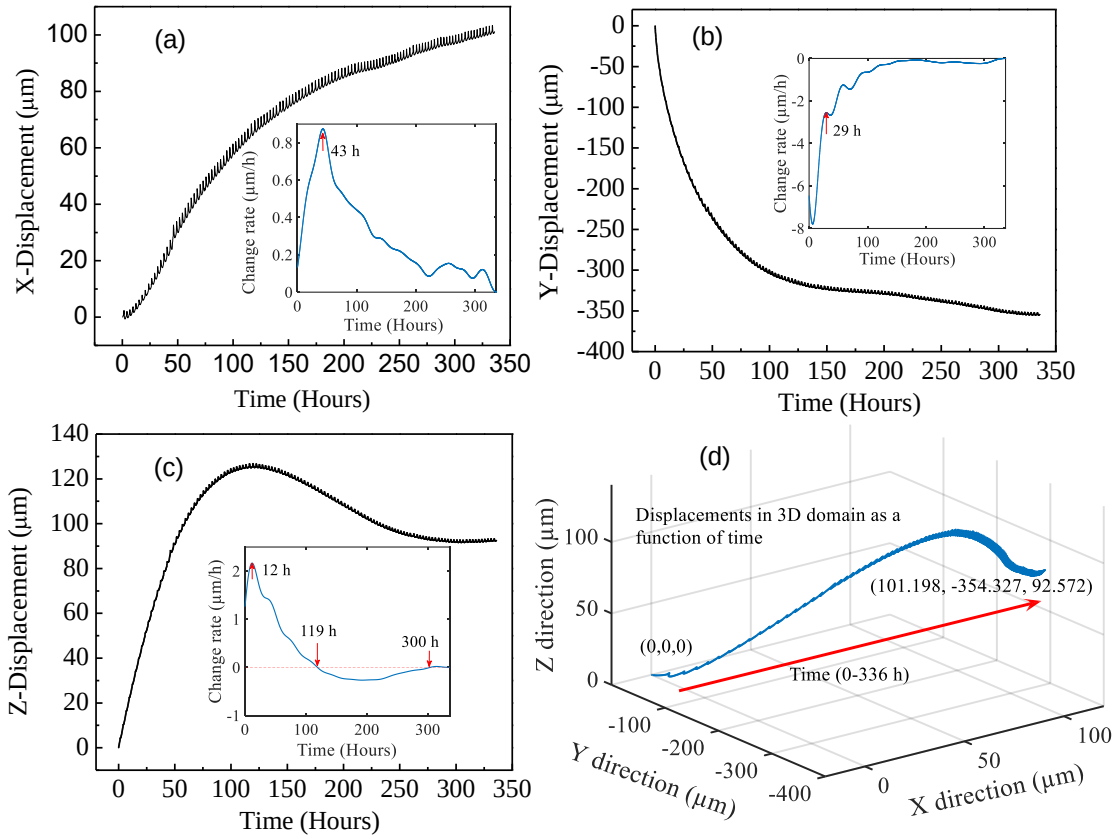

Figure 7. Real-time monitoring of 3D displacements between the long square brick of mortar and the steel base plate during the mortar curing/drying process. (a–c) Displacements versus time data for the *X*, *Y*, *Z* coordinates, respectively. The insets are plots of the time derivatives of the displacements as a function of measurement time for the *X*, *Y*, and *Z* directions. (d) Measured displacements plotted in the 3D domain parameterized by a time variable. The coordinate system used in the experiment was the same as the *XYZ* coordinate system shown in Figure 6(a). The displacements along the *X*, *Y*, and *Z* directions revealed the interfacial sliding along the *X* direction, the buckling along the *Y* direction, and the debonding along the *Z* direction between the mortar and the steel base plate, respectively.

During the experiment, the displacement along the *X* direction was also monitored using a commercial linear variable displacement transducer (LVDT) for comparison. Figure 8 shows a plot of the *X* displacement as a function of time measured by our prototype sensor and the LVDT. As can be seen, the results match well. However, it is obvious that our displacement sensor has a much better measurement resolution than the LVDT, and it

can perfectly quantify the displacement evolution process with a continuous and reliable output, while the LVDT data only shows discrete data points displaced back and forth every micrometer. An analogous setup and process can be used to check and qualify the displacements in the *Y* and *Z* directions.

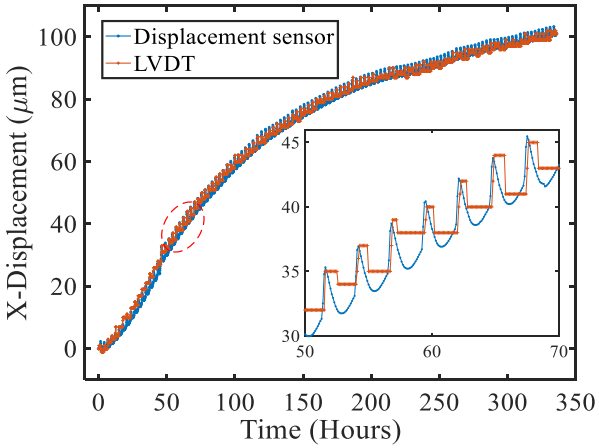

Figure 8. The displacement along the *X* direction measured by our prototype sensor and the LVDT. The inset shows the data collected during a period between 50 and 70 h.

4. CONCLUSIONS

In conclusion, we invented, fabricated, and demonstrated a low-cost and robust prototype of an optical fiber sensor for measuring relative displacements in the 3D domain. The fundamental idea employs three spatially arranged EFPIs as a combined triaxial sensing device. In our sensor design, the three EFPIs are formed by the endfaces of three optical fibers and three corresponding parallel mirrors. The optical fibers collectively and the mirrors collectively are supported by independent roof-like metal structures. The optical fiber component is suspended above the mirror component. When there are 3D

relative displacements between the two roof-like metallic structures, the cavity lengths of the EFPIs will change. A displacement transfer scheme that is user configurable and based on the geometry of a triangle was employed to adjust the dynamic range of each of the three EFPI sensors. Our triaxial sensor was calibrated and a cavity length-displacement coefficient matrix was calculated. Then, monitoring interfacial sliding and debonding between a long square brick of mortar and a steel base plate during the drying/curing process of the mortar was conducted to demonstrate the practicability of the triaxial displacement sensor. The experimental results show that our sensor is capable of accurately measuring the dynamics of the sliding and debonding process between a brick of mortar and the steel base plate, revealing interesting time points throughout the drying/curing process where the time rates of change for displacements peaked and plateaued. This resilient and simple-to-manufacture 3D displacement sensor has great potential for applications in SHM, the construction industry, oil well monitoring, geotechnology, and a wide range of other practical areas.

REFERENCES

[1] Shi, X.; Xie, N.; Fortune, K.; Gong, J. Durability of steel reinforced concrete in chloride environments: An overview. *Constr. Build. Mate.* 2012, *30*, 125-138.

[2] Li, W.; Xu, C.; Ho, S.C.M.; Wang, B.; Song, G. Monitoring Concrete Deterioration Due to Reinforcement Corrosion by Integrating Acoustic Emission and FBG Strain Measurements. *Sensors* 2017, *17*, 657.

[3] Wang, C.S; Wu, F.; Chang, F.K. Structural health monitoring from fiber-reinforced composites to steel-reinforced concrete. Smart Mater. Struct. 2001, 10, 548.

[4] Guo, T.T.; Wang, Q.Y.; Wu, L.H. Experimental research on distributed fiber sensor for sliding damage monitoring. Opt. Lasers Eng. 2009, 47, 156-160.

[5] Degala, S.; Rizzo, P.; Ramanathan, K.; Harries, K.A. Acoustic emission monitoring of CFRP reinforced concrete slabs. Constr. Build. Mater. 2009, 23, 2016-2026.

[6] Park, S.; Kim, J.W.; Lee, C.; Park, S.K. Impedance-based wireless debonding condition monitoring of CFRP laminated concrete structures. NDT E. Int. 2011, 44, 232-238.

[7] Li, W. J.; Fan, S., Ho, S.C.M.; Wu, J.; Song, G. Interfacial debonding detection in fiber-reinforced polymer rebar–reinforced concrete using electro-mechanical impedance technique. Struct. Health Monit. 2017, 1475921717703053.

[8] Song, G.; Gu, H.; Mo, Y.L. Smart aggregates: multi-functional sensors for concrete structures—a tutorial and a review. Smart Mater. Struct. 2008, 17, 033001.

[9] Bremer, K.; Weigand, F.; Zheng, Y.; Alwis, L.S.; Helbig, R. and Roth, B. Structural Health Monitoring Using Textile Reinforcement Structures with Integrated Optical Fiber Sensors. Sensors 2017, 17, 345.

[10] Tang, Y. and Wu, Z. Distributed long-gauge optical fiber sensors based self-sensing FRP bar for concrete structure. *Sensors* 2016, *16*, 286.

[11] Chen, Z.; Yuan, L.; Hefferman, G.; Wei, T. Ultraweak intrinsic Fabry–Perot cavity array for distributed sensing. *Opt. Lett.* 2015, *40*, 320-323.

[12] Huang, J.; Lan, X.; Luo, M.; Xiao, H. Spatially continuous distributed fiber optic sensing using optical carrier based microwave interferometry. *Opt. Express* 2014, *22*, 18757-18769.

[13] Wei, T., Han, Y.; Li, Y.; Tsai, H.L.; Xiao, H. Temperature-insensitive miniaturized fiber inline Fabry-Perot interferometer for highly sensitive refractive index measurement. *Opt. Express* 2008, *16*, 5764-5769.

[14] Zhu, C.; Chen, Y.; Du, Y.; Zhuang, Y.; Liu, F.; Gerald, R.E.; Huang J. A Displacement Sensor with Centimeter Dynamic Range and Submicrometer Resolution Based on an Optical Interferometer. *IEEE Sens. J.* 2017, *17*, 5523-5528.

[15] Jia, B.; He, L.; Yan, G. and Feng, Y.A differential reflective intensity optical fiber angular displacement sensor. *Sensors* 2016, *16*, 1508.

[16] Liu, J.; Hou, Y.; Zhang, H.; Jia, P.; Su, S.; Fang, G.; Liu, W. and Xiong, J. A wide-range displacement sensor based on plastic fiber macro-bend coupling. *Sensors* 2017, *17*, 196.

[17] Chen, J.P.; Zhou, J.; Jia, Z.H. High-sensitivity displacement sensor based on a bent fiber Mach–Zehnder interferometer. *IEEE Photon. Technol. Lett.* 2013, *25*, 2354-2357.

[18] Salceda-Delgado, G.; Martinez-Rios, A.; Selvas-Aguilar, R.; Álvarez-Tamayo, R.I.; Castillo-Guzman, A.; Ibarra-Escamilla, B.; Durán-Ramírez, V.M. and Enriquez-Gomez, L.F. Adaptable Optical Fiber Displacement-Curvature Sensor Based on a Modal Michelson Interferometer with a Tapered Single Mode Fiber. *Sensors* 2017, *17*, 1259.

[19] Bravo, M.; Pinto, A.M.; Lopez-Amo, M.; Kobelke, J.; Schuster, K. High precision micro-displacement fiber sensor through a suspended-core Sagnac interferometer. *Opt. Lett.* 2012, *37*, 202-204.

[20] Wu, Q.; Agus, M.H.; Wang, P.F.; Semenova, Y.; Farrell, G. Use of a bent single SMS fiber structure for simultaneous measurement of displacement and temperature sensing. *IEEE Photon. Technol. Lett.* 2011, *23*, 130-132.

[21] Zhu, H.H; Yin, J.H.; Zhang, L.; Jin, W.; Dong, J. Monitoring internal displacements of a model dam using FBG sensing bars. *Adv. Struct. Eng.* 2010, *13*, 249-261.

[22] Habel, W. R.; Hofmann, D.; Hillemeier, B. Deformation measurements of mortars at early ages and of large concrete components on site by means of embedded fiber-optic microstrain sensors. *Cem. Concr. Compos. 1997*, *19*, 81-102.

[23] Rapp, S.; Kang, L.H.; Han, J.H.; Mueller, U.C.; Baier, H. Displacement field estimation for a two-dimensional structure using fiber Bragg grating sensors. *Smart Mater. Struct.* 2009, *18*, 025006.

[24] Lee, B. H.; Kim, Y.H.; Park, K.S.; Eom, J.B.; Kim, M.J.; Rho, B.S.; Choi, H.Y. Interferometric optical fiber sensors. *Sensors* 2012, *12*, 2467-2486.

[25] Zhou, X. L.; Yu, Q. X. Wide-range displacement sensor based on fiber-optic Fabry–Perot interferometer for subnanometer measurement. *IEEE Sens. J.* 2011**,** *11*, 1602-1606.

[26] Bhatia, V.; Murphy, K.A.; Claus, R.O.; Jones, M.E.; Grace, J.L.; Tran, T.A. and Greene, J.A. Optical fibre based absolute extrinsic Fabry-Perot interferometric sensing system. *Meas. Sci. Technol*. 1996, *7*, 58-61.

III. PROBING THE THEORETICAL ULTIMATE LIMIT OF COAXIAL CABLE SENSING: MEASURING NANOMETER SCALE DISPLACEMENTS

ABSTRACT

Open-ended coaxial probes have been widely explored and commercialized for dielectric spectroscopy at microwave frequencies over the past decades. The working principle of the probes relies on the dependence of the fringing field on the complex permittivity of the material in front of the open end. In this paper, inspired by the optical fiber extrinsic Fabry-Perot interferometer, we propose a novel sensing scheme based on an open-ended hollow coaxial cable resonator (OE-HCCR). The resonator is constructed using two reflectors along the coaxial line. The first reflector is a metal post at the RF input end, shorting the inner and outer conductors. The second reflector is the open end, where a metal plate is placed parallel and near the open end. The resonance frequency of the open-ended coaxial resonator depends strongly on the gap distance between the metal plate and the open end of the coaxial cable, due to a modulation of the phase of the reflection coefficient that characterizes the open end. Thus, by correlating the resonance frequency to the gap distance between the metal plate and the open end (or the movement of the metal plate), the OE-HCCR can be used as a displacement sensor device. Importantly, the displacement measurement resolution of the OE-HCCR is three orders of magnitude greater than that of existing coaxial cable-based displacement sensors within a certain dynamic range (~ 0.11 mm), affording a resolution that is comparable to fiber optic sensors. The mathematical model of the OE-HCCR is discussed in detail, followed by a proof-of-concept for displacement measurements. The novel OE-HCCR device is suitable for

sensing applications in harsh environments and will advance the field of physical/chemical sensing.

1. INTRODUCTION

With many well-known advantages such as being diminutive in size, lightweight, highly-sensitive, immune to electromagnetic interference, and capable of remote operation, fiber-optic sensors have been extensively studied for the past three decades [1]-[3]. One of the major issues for fiber-optic sensors is that optical fibers are in general fragile and easily broken, especially in harsh environments, making installation and maintenance of optical fiber sensors a challenge in real-world scenarios [4]. Recently, a series of optical fiber extrinsic Fabry-Perot interferometers (OF-EFPIs) were reported for field applications, such as for monitoring displacement [5], inclination [6], [7], pressure [8], strain [9], and sliding/debonding [10]. However, the demodulation units for these EFPI-sensors involved an optical spectrum analyzer (OSA) or a high-speed spectrometer, both of which are bulky and expensive, hindering the way forward for fiber-optic sensors in real-world applications.

A coaxial cable is another type of cylindrical waveguide widely used in telecommunications. Described by the same electromagnetic (EM) theory, both optical fibers and coaxial cables can transmit EM waves over long distances. However, the frequencies of the EM waves supported by them are quite different, i.e., optical frequency (e.g., THz) for optical fibers and radio frequency (e.g., GHz) for coaxial cables. Therefore, optical fibers and coaxial cables have evolved along quite different pathways over the years. Recently, researchers have attempted to translate mature concepts that govern fiber-

optic sensors to coaxial cable sensors because coaxial cables are generally larger in diameter, made of durable metal and plastic components, and offer much greater robustness [11]-[20]. Coaxial cable-based sensor devices provide a promising solution for some challenging issues faced by their optical counterparts, optical fiber-based sensor devices, for example, fragility, the difficulties associated with installation, stringent requirements regarding fabrication, and stringent alignment requirements. Examples of successfully-demonstrated coaxial cable sensors include the coaxial cable Bragg grating (CCBG) [11], [12] and the coaxial cable Fabry-Perot interferometer (CCFPI) [13], both of which have been demonstrated for large strain measurements (e.g., up to 50000 με). Material limitations attributed to the dielectric layer inside a coaxial cable (e.g., polyethylene, which can only survive up to 200 °C), hinder the development of coaxial cable-based sensors for high-temperature and harsh environments. However, very recently, a hollow coaxial cable Fabry-Perot resonator (HCC-FPR) was reported for measuring strain and displacement at elevated temperatures (up to 1000 °C), in which an all-stainless steel hollow coaxial cable with air as the dielectric layer was introduced [21]. The salient point is that such an HCC can be modified for other sensing applications to further address the issues faced by the optical fiber counterparts [22], [23]. However, the HCC-FPR is essentially an analog of the optical fiber intrinsic Fabry-Perot interferometer (OF-IFPI), offering limited structural flexibility [24]. Also, the measurement resolution of the HCC-FPR-based sensor is limited to one micrometer [23], [25], which is three orders of magnitude lower than that of a typical OF-EFPI device.

Open-ended coaxial probes have been widely demonstrated and commercialized for dielectric spectroscopy at microwave frequencies [26]-[30]. A gap-coupled open-ended

coaxial line resonator was proposed in the 1980s, in which the fringing field at the open end of the resonator was perturbed by an unknown dielectric material for the purpose of analysis of the material [31], [32]. The complex permittivity of the dielectric material was then correlated to the measured changes in the resonance frequency and quality factor (Q-factor) of the resonator. Other applications of the open-ended coaxial probes were also studied over the years, all of which were based on dielectric spectroscopy [33]-[37]. However, examining the working principles, one realizes that the open-ended coaxial probes are essentially analogs of the OF-EFPI, raising interesting questions: Can the OF-EFPI-based sensing configuration be adapted to open-ended coaxial probes? Can the displacement measurement resolution of open-ended coaxial probes, as an example, be comparable to the resolution of OF-EFPI devices?

In this paper, an open-ended hollow coaxial cable resonator (OE-HCCR) is proposed for general sensing applications, and displacement measurements are experimentally demonstrated as a proof of concept. The all-stainless steel HCC used in the prototype sensor offers strong mechanical strength and the potential capability for accurate measurements of displacement-related parameters conducted at high temperatures. A metal post, shorting the inner and outer conductors, serves as the first reflector of the resonating coaxial structure. A parallel conductive surface is placed a specified distance away from the open end, serving as an element that can undergo displacement. Importantly, the open end of the HCC, with the external conducting surface (e.g., a metal plate), and a dielectric, (e.g., air) sandwiched in between, serves as the second reflector of the resonating coaxial structure. In a prototype OE-HCCR, when the gap distance between the movable metal plate and the open end of the coaxial cable varies, the fringing capacitance changes, leading

to variations in the reflection coefficient of the second reflector of both magnitude and phase [38]. The change in the phase of the reflection coefficient results in a shift of the reflection spectrum of the OE-HCCR. Thus, correlating the parameters of interest (e.g., various physical or chemical quantities, pressure, acceleration, force, etc.) to the gap distance between the metal plate and the open end of the coaxial cable, which can be monitored by tracking the shift of the resonance frequency, the OE-HCCR can function as a sensor device after proper calibration. The mathematical model of the OE-HCCR in closed form is discussed in Section 2. The calculation results based on the mathematical model and a demonstration experiment for displacement measurements, as a proof of concept, are presented in Section 3. The potential sensing applications of the OE-HCCR are also discussed.

2. MATHEMATICAL MODEL OF THE OE-HCCR

Figure 1 shows a schematic diagram of the OE-HCCR. The diameter of the inner conductor and the outer conductor are denoted as 2a and 2b, respectively. Compared to traditional coaxial cables, the dielectric layer of the HCC is removed and replaced by air between the inner and outer conductors. A metal plate is placed at the open end of the HCC, and the thickness of the air dielectric in the gap between the open end and the metal plate is d. A grounded flange with an infinite diameter is assumed for the model [39]. A metal post is welded within the HCC at the RF input end. The metal post shorts the inner conductor to the outer conductor, giving rise to the storage of magnetic energy in proximity to the post. Thus, a large impedance mismatch results, providing a high reflection point to

the EM wave traveling within the coaxial cable. From the perspective of an equivalent circuit, the metal post is identical to a shunt inductor L and a series shunt resistor R. Thus, the reflection coefficient (r_1) caused by the metal post can be expressed as [40]:

$$r_1 = \Gamma_1 e^{j\phi_1} = \frac{R + j\omega L - Z_0}{R + j\omega L + Z_0}$$
$$\phi_1 = \pi - \tan^{-1}\frac{\omega L}{Z_0 - R} - \tan^{-1}\frac{\omega L}{Z_0 + R} \quad (1)$$

where Γ_1 and ϕ_1 represent the magnitude and phase of the reflection coefficient, respectively; Z_0 is the characteristic impedance of the HCC; and, ω is the angular frequency of the input signal. In the high-frequency region (e.g., > 3 GHz), a capacitor (ΔC) should also be considered in the equivalent circuit model.

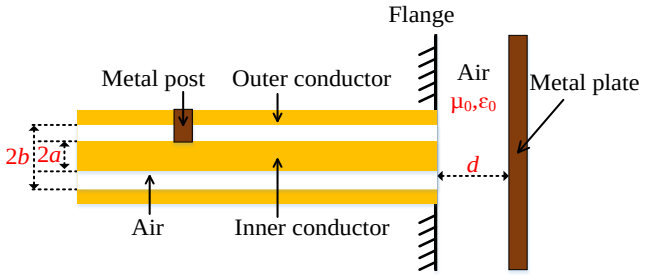

Figure 1. Schematic diagram of an OE-HCCR terminated by a metal plate-backed air dielectric layer with a gap thickness of d. The metal post serves as the first reflector, and the open end serves as the second reflector. μ_0 and ε_0 are the permeability and permittivity of air, respectively.

The open end of the HCC can be considered as an open circuit, causing approximately 100% reflection of the EM wave. From the perspective of an equivalent

circuit, the open end can be modeled simply by a shunt capacitance *C*. Thus, the reflection coefficient (r_2) for the open end can be expressed as:

$$r_2 = \Gamma_2 e^{j\phi_2} = \frac{1 - j\omega Z_0 C}{1 + j\omega Z_0 C}$$
$$\phi_2 = -2\tan^{-1}(\omega Z_0 C) \tag{2}$$

where Γ_2 and ϕ_2 represent the magnitude and phase of the reflection coefficient, respectively. The shunt capacitance due to the disturbed fringing field at the open end, employing the spectral domain analysis, is given by [41]:

$$C = C_1 + C_2 \tag{3}$$

where

$$C_1 = \frac{2\varepsilon_0}{[\ln(b/a)]^2}\int_a^b\int_a^b\int_0^\pi \frac{\cos\phi' d\rho d\rho' d\phi'}{\sqrt{[\rho^2 + \rho'^2 - 2\rho\rho'\cos\phi']}} \tag{4}$$

$$C_2 = \frac{4\varepsilon_0}{[\ln(b/a)]^2}\sum_{n=1}^{\infty}\int_a^b\int_a^b\int_0^\pi \frac{\cos\phi' d\rho d\rho' d\phi'}{\sqrt{[\rho^2 + \rho'^2 + 4n^2d^2 - 2\rho\rho'\cos\phi']}} \tag{5}$$

where ρ and ρ' denote the radial direction, and ϕ' denotes the azimuthal direction. Note that C_1 is essentially the static capacitance at the open end when the gap distance *d* is infinite; C_2 is an additional variable to compensate for the finite thickness of the air dielectric.

Our analysis begins with the assumption that a microwave signal with a frequency *f* is launched into the OE-HCCR. The input signal will be partially reflected by the metal post. The transmitted portion of the signal resonates in the coaxial structure, being reflected back and forth between the two reflectors, i.e., the metal post and the open end. With each

reflection at the metal post, the signal is partially coupled out of the OE-HCCR. Summation of all waves coupled out at the first reflector yields the reflection coefficient (r) of the OE-HCCR:

$$r = \frac{r_1^* - r_2 e^{-\alpha 2d_0 - j\delta}}{1 - r_1 r_2 e^{-\alpha 2d_0 - j\delta}} = \frac{\Gamma_1 e^{-j\phi_1} - \Gamma_2 e^{j\phi_2} e^{-\alpha 2d_0 - j\delta}}{1 - \Gamma_1 e^{-j\phi_1} \Gamma_2 e^{j\phi_2} e^{-\alpha 2d_0 - j\delta}} \tag{6}$$

where d_0 is the distance between the first reflector and the second reflector; α is the transmission loss of the HCC; $\delta = \frac{4\pi d_0 f}{c}$ denotes the round-trip phase delay between two partially reflected waves; and, c is the speed of light in vacuum. The superscript asterisk "*" denotes the complex conjugate. The magnitude (M) of the reflection coefficient can then be obtained:

$$M = \sqrt{\frac{\Gamma_1^2 - 2\Gamma_1\Gamma_2 e^{-\alpha 2d_0}\cos(\delta - \phi_1 - \phi_2) + \Gamma_2^2 e^{-\alpha 4d_0}}{1 - 2\Gamma_1\Gamma_2 e^{-\alpha 2d_0}\cos(\delta - \phi_1 - \phi_2) + \Gamma_1^2\Gamma_2^2 e^{-\alpha 4d_0}}} \tag{7}$$

Further evolving Equation (7), we have

$$M = \sqrt{1 + \frac{(\Gamma_1 - \Gamma_2 e^{-\alpha 2d_0})^2 - (1 - \Gamma_1\Gamma_2 e^{-\alpha 2d_0})^2}{(1 - \Gamma_1\Gamma_2 e^{-\alpha 2d_0})^2 + 4\Gamma_1\Gamma_2 e^{-\alpha 2d_0}\sin^2\frac{\delta - \phi_1 - \phi_2}{2}}} \tag{8}$$

It is clear that the magnitude of the reflection coefficient of the OE-HCCR reaches a minimum when the phase term in Equation (8) satisfies the following condition [42]:

$$\sin^2\frac{\delta - \phi_1 - \phi_2}{2} = 0 \Rightarrow \delta - \phi_1 - \phi_2 = 2m\pi, m = 0,1,2,3... \tag{9}$$

The “analytical” expression for the resonance frequencies (i.e., when the magnitudes reach a series of local minimum values) can be obtained by substituting $\delta = \frac{4\pi d_0 f}{c}$ into Equation (9):

$$f_{res} = \frac{c(2m\pi + \phi_1 + \phi_2)}{4\pi d_0} \tag{10}$$

Equation (10) clearly reveals that the fundamental resonance frequency of the OE-HCCR is a function of ϕ_1 and ϕ_2 (i.e., the phases of the reflection coefficients of the two reflectors). The sensing capability of the OE-HCCR is predicated on changes to ϕ_2. To be specific, according to Equation (2), the phase of r_2 is a function of the fringing capacitance at the open end, which depends exponentially upon the gap distance between the metal plate and the open end of the coaxial cable. Consequently, when d varies slightly, the fringing capacitance changes, leading to changes in both the magnitude and phase of r_2. The change in ϕ_2 results in a shift of the resonance frequency. By tracking the frequency shift of the reflection spectrum, the movement of the metal plate can be accurately determined. Thus, any physical parameter that can be correlated to the movement of the metal plate (e.g., displacement, or deflection under pressure) can be accurately measured by the proposed OE-HCCR by tracking the resonance frequency shift. However, since both ϕ_1 and ϕ_2 are functions of frequency, Equation (10) has no analytical solution. The following section presents the numerical solutions to Equation (10).

3. NUMERICAL CALCULATIONS AND PROOF OF CONCEPT

3.1. NUMERICAL CALCULATIONS

The reflection coefficients of the two reflectors must first be determined to solve Equation (10) numerically. Since the working principle of the OE-HCCR for sensing applications relies on correlating parameters of interest to the reflection coefficient at the open end, to decrease the approximation errors from employing the equivalent circuit model, the reflection coefficient of the first reflector is numerically determined employing full-wave simulation software, ANSYS HFSS. Figure 2 presents the results calculated using HFSS: (a) magnitude plot, and (b) phase plot. The parameters used in the simulation are: a = 3 mm; b = 7 mm; and, diameter of the metal shorting post D = 3 mm. As can be seen, both the magnitude and phase of the reflection coefficient decrease as frequency increases, which matches well with Equation (1).

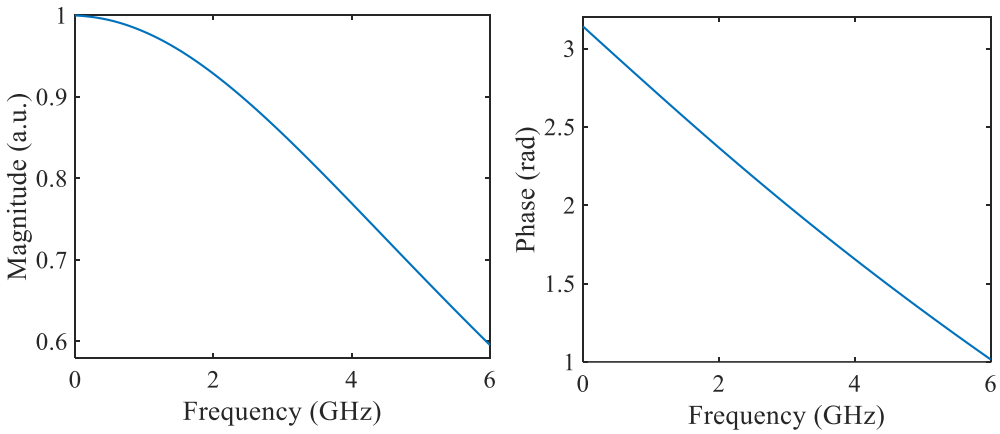

(a) (b)

Figure 2. Calculated reflection coefficient of the first reflector as a function of frequency employing ANSYS HFSS: (a) Magnitude component plot (Γ_1 vs. $\omega/2\pi$); (b) Phase component plot (ϕ_1 vs. $\omega/2\pi$).

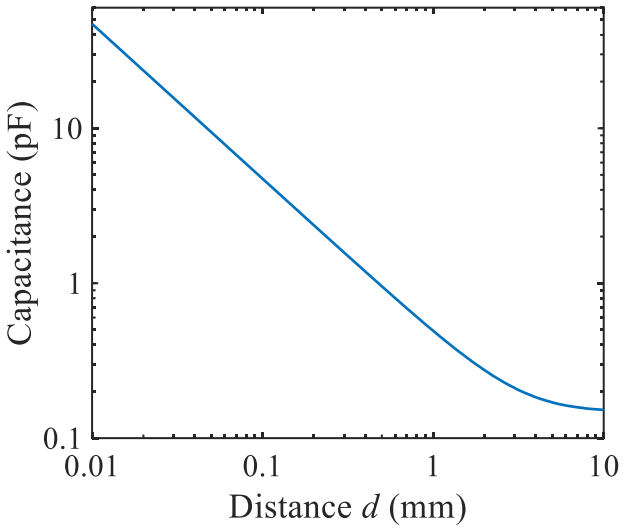

(a)

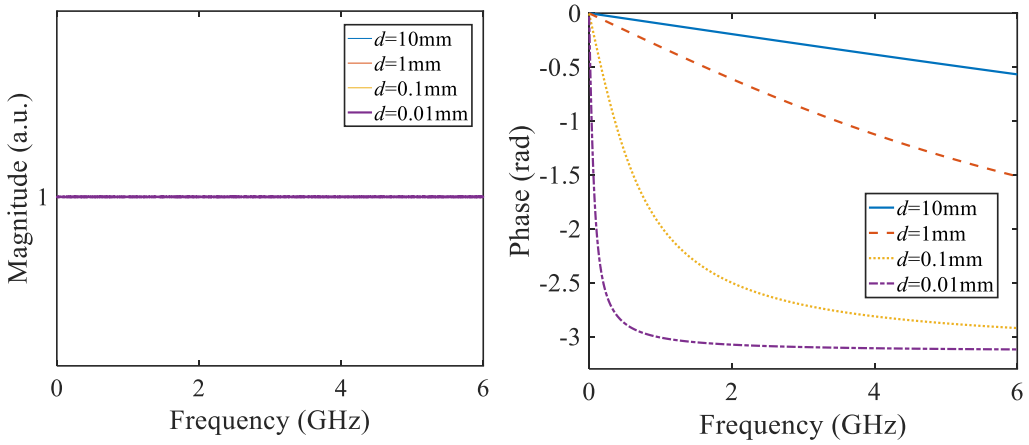

(b) (c)

Figure 3. Investigation results of the open end of the OE-HCCR. (a) Calculated static capacitance as a function of the gap distance between the metal plate and the open end of the coaxial cable; (b) Magnitude component plot (Γ_2 vs. $\omega/2\pi$); (c) Phase component plot (ϕ_2 vs. $\omega/2\pi$) for four values of d.

Figure 3 shows the numerical calculation results for the second reflector, i.e., the open end. Based on Equations (3)-(5), the static capacitance at the open end as a function

of the gap distance between the metal plate and the open end (*d*) is plotted (using a log-log scale) in Figure 3(a). The calculated capacitance increases exponentially as the gap distance

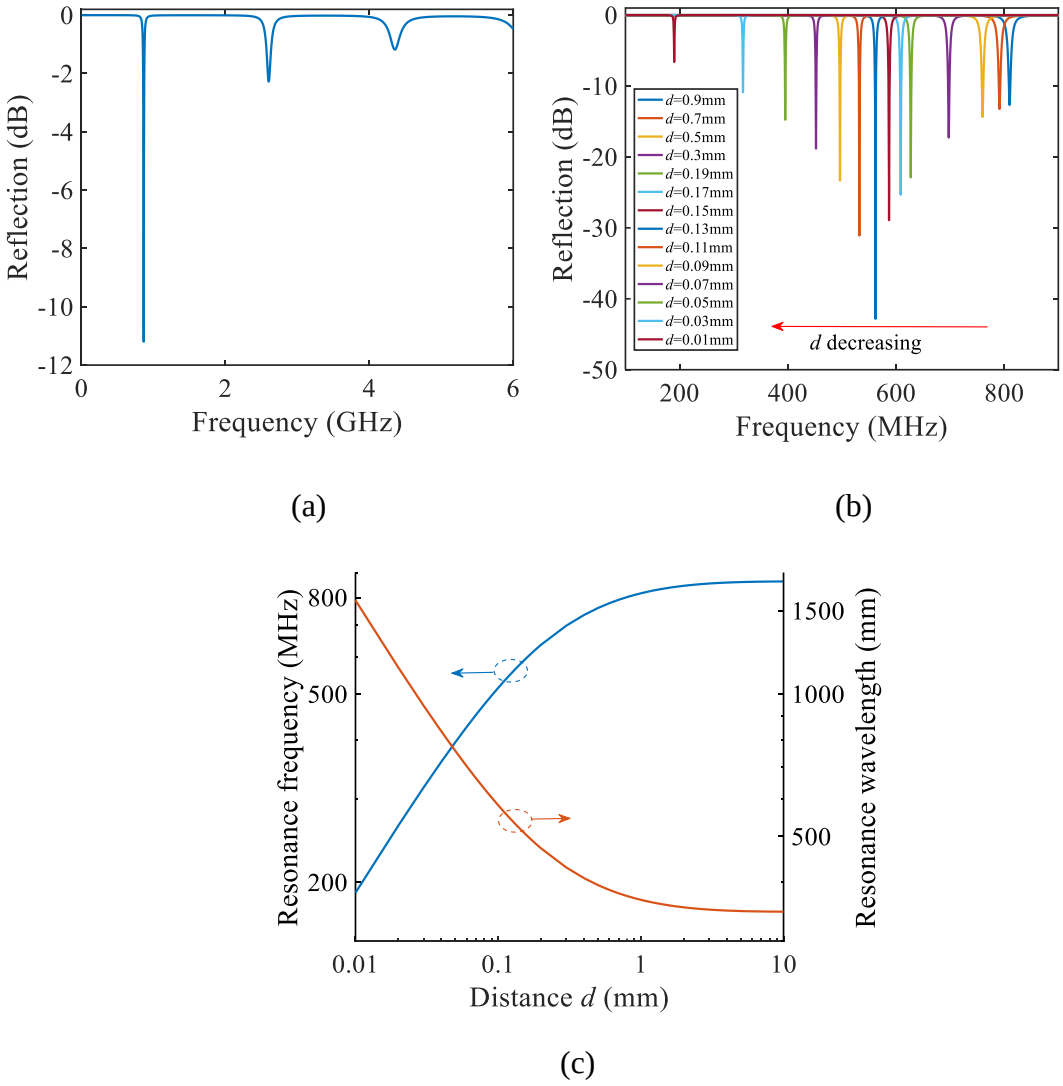

Figure 4. Numerical calculation results of the OE-HCCR. (a) Calculated reflection spectrum of the OE-HCCR when the gap distance between the open end of the coaxial cable and the metal plate, *d*, is 10 mm. (b) Evolution of the reflection spectrum of the OE-HCCR at different gap settings of *d*. (c) Fundamental resonance frequency/wavelength of the OE-HCCR as a function of the gap distance *d* between the open end of the coaxial cable and the metal plate.

decreases, which matches well with a previous study [41]. Figure 3(b) and (c) plot the magnitude and phase spectra of the open-end reflection coefficient, respectively for *d* equal to 0.01 mm, 0.1 mm, 1 mm, and 10 mm. As can be seen from Figure 3(b), the magnitude of r_2 remains constant over the frequency range investigated and is approximately equal to 1, indicating that the wave reaching the open end is nearly completely reflected. The phase of r_2 decreases as frequency increases. As the metal plate approaches the open end of the coaxial cable, the phase decreases rapidly as a function of frequency and approaches π. The strong dependence of the phase on the gap distance between the open end of the coaxial cable and the metal plate reveals the fundamental basis for proposing the utility of the OE-HCCR for sensing applications.

Substituting the calculated reflection coefficients of the two reflectors into Equation (6), the reflection coefficient of the OE-HCCR can be obtained. Figure 4(a) is a plot of the magnitude of the reflection coefficient of the OE-HCCR versus frequency when the gap distance between the open end of the coaxial cable and the metal plate, *d*, is 10 mm. The physical length between the metal shorting post and the open end of the coaxial cable is set to 75 mm. Within the observation bandwidth that spans from 1 MHz to 6 GHz, discrete resonance frequencies can be seen at 0.860 GHz (fundamental resonance frequency), 2.602 GHz (2^{nd} harmonic) and 4.356 GHz (3^{rd} harmonic). As can be seen, the signal-to-noise ratio (SNR) of the resonance dip decreases as the frequency increases. This observation is reasonable because the reflectivities of the two reflectors become unbalanced as the frequency increases (compare Figure 2(a) and Figure 3(b)). Figure 4 (b) plots the fundamental resonance frequency in the reflection spectra of the OE-HCCR when the gap distance *d* between the metal plate and the open end of the coaxial cable decreases from

0.9 mm to 0.01 mm. Clearly, the fundamental resonance frequency shifts to the lower frequency region as the gap distance *d* decreases. The calculated fundamental resonance frequency/wavelength of the OE-HCCR as a function of the gap distance *d* between the open end and the metal plate is shown in Figure 4(c). The fundamental resonance frequency (wavelength) decreases (increases) exponentially as the gap distance *d* decreases. When the gap distance *d* is beyond 10 mm, the movement of the metal plate has little influence on the fringing field at the open end of the coaxial cable, thus barely affecting the resonance frequency of the OE-HCCR.

The calculation results demonstrate that the proposed OE-HCCR could be employed for sensing external parameters that are correlated to the gap distance *d* between the open end of the coaxial cable and the metal plate after it is properly calibrated. Moreover, the resolution of the OE-HCCR device for displacement measurements depends on the initial setting of the gap distance between the metal plate and the open end of the coaxial cable. Through numerical calculations (i.e., as shown in Figure 4(c)), we found that the displacement measurement sensitivity increases exponentially as the gap distance decreases. Importantly, when the gap distance decreases down to ~0.11 mm, the measurement sensitivity (i.e., wavelength shift/distance change) is determined to be larger than 2000 mm/mm and keeps increasing as the gap distance decreases. Considering our previous studies on an HCC-FPR [25], which has a sensitivity of 2 mm/mm and a displacement resolution of 1 μm, the gap distance measurement resolution of the OE-HCCR could reach up to 1 nm in the range of 0 ~ 0.11 mm. Therefore, the one-dimensional spatial-metering resolution of the OE-HCCR is comparable to that of an OF-EFPI.

Table 1. Comparisons between the OE-HCCR and its optical counterpart, the OF-EFPI.

Device characteristics	OE-HCCR	OF-EFPI
Sensing platform	Coaxial cable	Optical fiber
Operating frequency	DC – 100 GHz	200 – 400 THz
Dynamic range (displacement of the movable reflector)	~ 8 mm (user-configurable)	~ 2 mm
Displacement measurement (dynamic range: resolution)	User-configurable 0 – 0.11 mm: 0.1 – 1 nm 0.11 – 4 mm: 1 nm – 0.1 μm 4 – 8 mm: ~1 μm	2 mm: 0.1 nm – 1 nm
Immunity to electromagnetic interference	No	Yes
Measurement accuracy	High	High
Q-factor	100 – 1,000	2 – 100,000
Interrogator/sensor extension length	0.1 – 1,000 m	0.1 – 100,000 m
Multiplexing arrangement	Parallel	Parallel and serial
Temperature-displacement crosstalk	1 – 10 ppm	0.1 – 10 ppm
Temperature tolerance	-200 – 1500 ^{o}C	-200 – 800 ^{o}C
Ease of fabrication	High	Low
Reflector alignment requirements	Low	High
Size of sensor element (diameter: length)	0.5 – 5 cm: 1 – 10 cm	0.01 – 1 mm: 0.1 – 2 mm
Mass of sensor element	1 – 100 g	0.001 – 0.1 g
Fabrication cost	Low	High
Interrogation apparatus cost	$100 – $5,000	$10,000 – $50,000

A detailed comparison between the OE-HCCR and its optical counterpart, the OF-EFPI, is shown in Table 1. The unique features of the OE-HCCR, i.e., the high sensitivity and high resolution in a certain range, suggests various potential sensing applications where accurate measurements over a small dynamic range are needed. For example, accurate

displacement measurements in high-temperature, harsh environments can be achieved by correlating the displacement under test to the movement of the metal plate. High-temperature, static/dynamic pressure measurements can also be realized by replacing the metal plate with a thin metal sheet (diaphragm). The metal sheet can be directly fixed to the flange at the open end of the coaxial cable, and the gap distance between the sheet and the open end can be constrained and defined by a circular spacer (e.g., a gasket). When the metal sheet deflects in response to pressure variations, the effective gap distance between the metal sheet and the open end of the coaxial cable changes, leading to a frequency shift of the reflection spectrum from the OE-HCCR. Thus, static/dynamic pressures can be monitored. Probing nanoradian changes in tilt measurements can also be achieved by engineering a pendulum structure at the open end of the coaxial cable [6]. In addition, based on judicious mechanical designs, different sensor devices based on the OE-HCCR can be further employed for sensing various parameters, such as acceleration, vibration, corrosion, etc., especially for those involving heavy duty, large strain, high temperature, and other variables associated with harsh environments.

Examining Figure 4(b), an interesting observation is that as the gap distance *d* decreases, the SNR of the fundamental resonance dip first increases and reaches a maximum at about 40 dB, and then decreases. Figure 5 presents the reflection at the fundamental resonance frequency of the OE-HCCR as a function of the gap distance *d* between the metal plate and the open end of the coaxial cable. The changes in the reflection at the fundamental frequency as a function of gap distance *d* reveals an evolution of the coupling status of the OE-HCCR. As the gap distance *d* decreases, the fundamental resonance frequency shifts to a lower frequency region, where the magnitude of the

reflection coefficient of the first reflector increases, as shown in Figure 2(a). Therefore, the coupling status of the OE-HCCR evolves through states from *over coupling* to *critical coupling* and then to *loose coupling*. It should be noted that for a fixed resonance frequency (corresponding to a fixed gap distance *d*), the SNR of the fundamental frequency can be tuned via modifying the coupling coefficient of the first reflector (i.e., the metal post) by changing the shape/size of the metal post [20]. On the other hand, the resonance frequencies and the SNR can also be tuned by making the first reflector movable or inserting a dielectric into the initial hollow coaxial line.

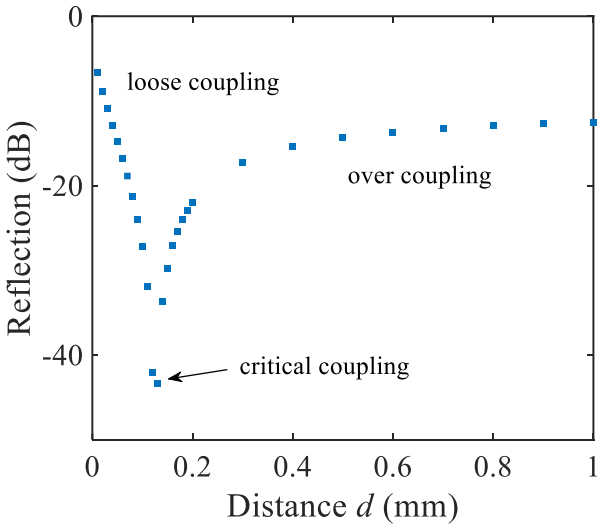

Figure 5. Reflection at the fundamental resonance frequency as a function of the gap distance *d* between the open end of the coaxial cable and the metal plate.

The results of additional calculations performed to investigate the dependence of the resonance frequency and the sensitivity of the OE-HCCR on the gap distance *d* for a series of values for the physical length between the metal shorting post and the open end of the coaxial cable, d_0, are shown in Figure 6. Figure 6(a) presents the fundamental

resonance frequency as a function of the gap distance *d* between the metal plate and the open end of the coaxial cable when the physical cavity length between the metal post and the open end of the coaxial cable is set to 100 mm, 90 mm, 80 mm, 70 mm, and 60 mm. In all five cases, the resonance frequency of the OE-HCCR decreases exponentially as the gap distance *d* decreases, as expected. The evolution of the sensitivity (i.e., fundamental resonance frequency shift/distance change) as a function of the gap distance *d* can be obtained by differentiating the fundamental resonance frequency with respect to the gap distance *d*, as shown in Figure 6(b). As can be seen, the measurement sensitivity increases exponentially as the gap distance *d* decreases in all of the five cases, as expected. Clearly, the smaller the cavity length between the metal shorting post and the open end of the coaxial cable, the higher the measurement sensitivity; this observation proffers a potential optimization of the proposed OE-HCCR as a sensor device.

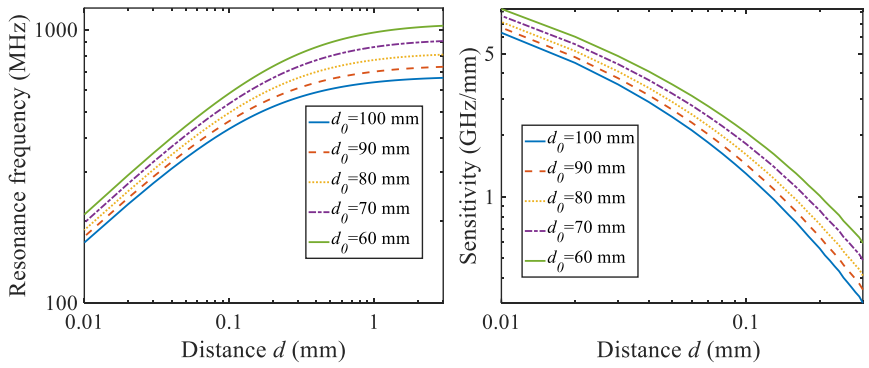

(a) (b)

Figure 6. Investigations of the resonance frequency and sensitivity of the OE-HCCR for several physical distances between the metal shorting post and the open end of the coaxial cable. (a) Fundamental resonance frequency of the OE-HCCR as a function of the gap distance *d* between the open end of the coaxial cable and the metal plate. (b) Measurement sensitivity (fundamental resonance frequency shift/distance change) as a function of the gap distance *d* between the open end of the coaxial cable and the metal plate.

3.2. PROOF OF CONCEPT, DISPLACEMENT MEASUREMENTS

A prototype sensor was designed, fabricated, and demonstrated for displacement measurements based on a home-fabricated hollow coaxial cable to demonstrate the proposed concept of the OE-HCCR for sensing applications. Figure 7 includes an image of a prototype OE-HCCR and a schematic of a basic application employing the prototype OE-HCCR. Figure 7(a) shows a photograph of the OE-HCCR device fabricated from a stainless steel tube and flange. The inner and outer diameters of the stainless steel coaxial cable were designed to be 6 mm and 14 mm, respectively, resulting in a characteristic impedance of approximately 50.8 Ω (the dielectric is air). This design also makes the home-fabricated cable end compatible with a standard N-Type connector. Therefore, the home-fabricated hollow coaxial cable can be connected to a commercial coaxial line using a standard N-Type to SMA connector. A metal post with a diameter of 3 mm was welded within the hollow coaxial cable, shorting the inner and outer conductors. The length between the metal post and the open end was set to 75 mm. The parameters used in the fabrication of the prototype sensor were the same as the parameters used in the calculations discussed above. The diameter of the flange at the open end is 48 mm. The experimental setup for a displacement measurement demonstration is schematically illustrated in Figure 7(b). A vector network analyzer (VNA, Agilent 8753ES) was used as the interrogator for the OE-HCCR device. The OE-HCCR was connected to port 1 of the VNA via a commercial 50 Ω coaxial cable. A metal plate was connected to a cylindrical rod, which was used as the displacement element. The rod was attached to a translation stage, which afforded a lateral displacement resolution of 10 μm. A personal computer (PC) was interfaced to the VNA and the translation stage to record the data autonomously in real-time.

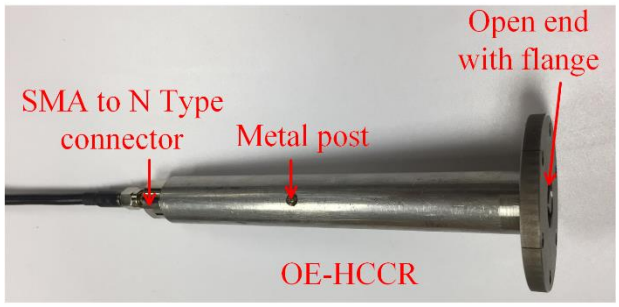

(a)

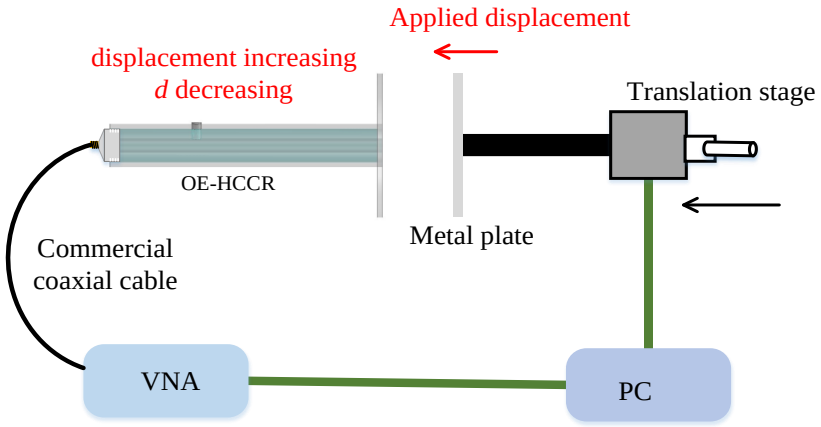

(b)

Figure 7. Overview image and corresponding schematic of the OE-HCCR sensor device and ancillary apparatus useful for accurately measuring small displacements (~1nm-8mm). (a) Photograph of the prototype OE-HCCR sensor. The outer diameter of the flange at the open end of the coaxial cable is 48 mm. (b) Schematic diagram of the experimental setup for displacement measurement demonstrations using the OE-HCCR device. The applied displacement was inversely correlated to the gap distance *d* between the open end of the coaxial cable and the metal plate, i.e., increasing the displacement causes the gap distance *d* to decrease.

The measured reflection spectrum magnitude (i.e., S_{11}) versus frequency for the prototype OE-HCCR device is plotted in Figure 8(a). The gap distance *d* between the metal plate and the open end of the coaxial cable was set to approximately 10 mm. Discrete resonance frequencies were recorded, including the fundamental frequency at 0.857 GHz,

and the higher-order harmonics, as expected. The broad feature at ~5.6 GHz is a spurious result. The trend of the magnitudes of the resonance dips matches well with the calculation results, as shown in Figure 4(a). Small periodic ripples can also be observed in the measured reflection spectrum, which are due to the multiple reflections originating from port 1 of the VNA and the interface between the 50 Ω commercial coaxial cable and the ~50.8 Ω OE-HCCR. The high transmission loss in the high-frequency region of the commercial coaxial cable leads to a downward trend of the reflection spectrum, as indicated in Figure 8(a). Additionally, an approximately 0.3% frequency discrepancy was obtained between the measured fundamental resonance frequency (0.857 GHz) and the calculated result (0.860 GHz). We believe that the frequency discrepancy is mainly due to modeling/numerical errors combined with experimental errors.

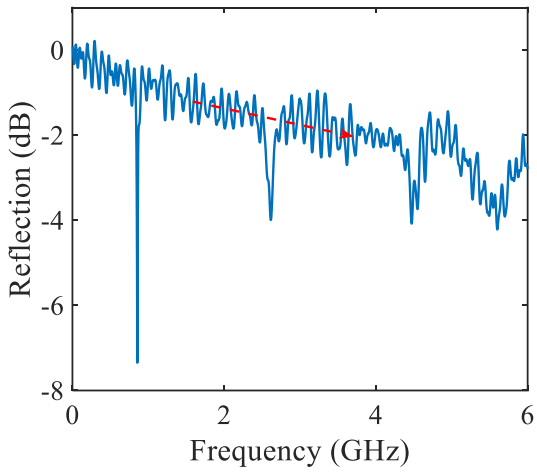

(a)

Figure 8. Experimental results of a prototype OE-HCCR device for applied displacement measurements. (a) Measured reflection spectrum of a prototype OE-HCCR when the gap distance *d* between the metal plate and the open end of the coaxial cable is set to 10 mm. (b) Evolution of the reflection spectrum (fundamental frequency) of the OE-HCCR for different applied displacement settings. (c) Fundamental resonance frequency of the OE-HCCR as a function of applied displacement.

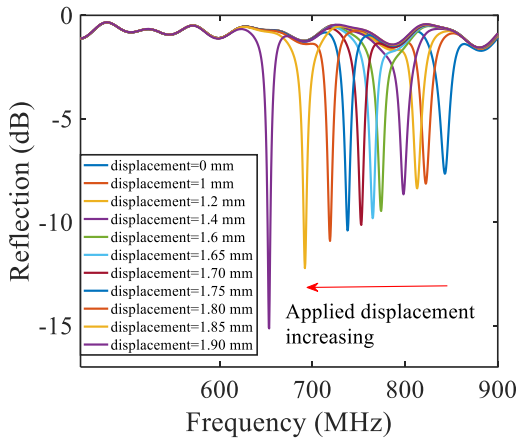

(b)

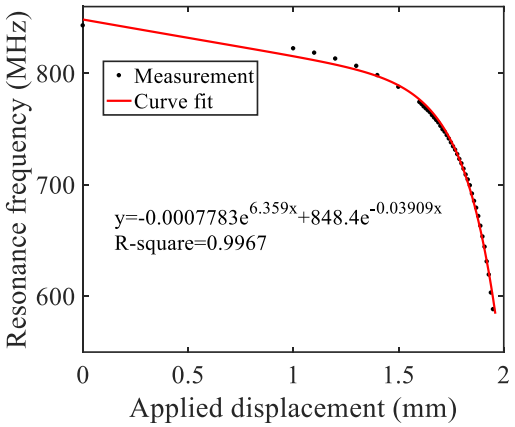

(c)

Figure 8. Experimental results of a prototype OE-HCCR device for applied displacement measurements. (a) Measured reflection spectrum of a prototype OE-HCCR when the gap distance *d* between the metal plate and the open end of the coaxial cable is set to 10 mm. (b) Evolution of the reflection spectrum (fundamental frequency) of the OE-HCCR for different applied displacement settings. (c) Fundamental resonance frequency of the OE-HCCR as a function of applied displacement. (cont.)

Figure 8(b) includes plots of the reflection spectra of the prototype OE-HCCR displacement sensor for different displacement settings. The initial position of the metal plate was set to approximately 2.1 mm away from the open end of the coaxial cable. As an applied displacement to the OE-HCCR sensor increased, the metered gap distance *d*

between the open end of the coaxial cable and the metal plate decreased, leading to a decrease in the resonance frequency, which matched well with the trend depicted in Figure 4(c). Also, the signal strength of the resonance reflection dip kept increasing, indicating that the OE-HCCR was approaching critical coupling from over coupling, according to Figure 5. Figure 8(c) shows the measured fundamental resonance frequency of the prototype OE-HCCR as a function of applied displacement. The resonance frequency decreased exponentially and the rate of decrease increased as the applied displacement increased (gap distance *d* decreased), which matched well with the previous modeling. A curve fit was applied to the measured data, and an exponential relationship was revealed with an R-square of 0.9967. Although the relationship between the applied displacement and frequency shift is not linear, the OE-HCCR could be used as a sensor device after proper calibration. On the other hand, in some applications where a small dynamic range of applied displacement/deflection is needed (e.g., tens of microns), such as the sensing of vibration, acceleration, inclination, or pressure, the response of the OE-HCCR can be considered linear over a narrow specified dynamic range.

4. CONCLUSIONS

We proposed a novel sensing scheme based on an OE-HCCR, from which a series of low-cost, robust, and highly sensitive sensors with high measurement resolution could be developed. First, the mathematical modeling of the OE-HCCR was discussed in detail, revealing the capability of the OE-HCCR as a sensor device with high sensitivity and variable dynamic range. A displacement demonstration experiment was performed to

demonstrate the sensor concept. The experimental results verified that the resonance frequency decreased exponentially as a function of an increased applied displacement (corresponding to a decreased gap distance), indicating that the OE-HCCR could be used as a one-dimensional displacement sensor device after it is properly calibrated. According to the calculation results, over a certain dynamic range (~0.11 mm), the displacement measurement resolution of the proposed OE-HCCR could be three orders of magnitude larger than that for previously reported coaxial cable-based sensing devices. Compared to the OF-EFPI, the OE-HCCR offers comparable measurement sensitivity and resolution over a specified dynamic range, but is much more robust and can survive heavy-duty, large-strain, and high-temperature harsh environments. In addition, the system cost of the OE-HCCR (including sensor fabrication and interrogation unit) is lower than its optical fiber counterpart and can be further reduced by employing a feedback loop interrogation unit [43]. It is envisioned that the proposed OE-HCCR sensor might revolutionize and advance the sensing field, and enable many important applications that have long been desired but are currently unavailable.

REFERENCES

[1] K. Grattan and T. Sun, "Fiber optic sensor technology: an overview," *Sens. Actuators A Phys.*, vol. 82, no. 1-3, pp. 40-61, May. 2000.

[2] Z. Chen, L. Yuan, G. Hefferman, and T. Wei, "Ultraweak intrinsic Fabry–Perot cavity array for distributed sensing," *Opt. Lett.*, vol. 40, no. 3, pp. 320-323, Feb. 2015.

[3] X. Zhang, H. Shao, Y. Yang, H. Pan, F. Pang, and T. Wang, "Refractometry with a tailored sensitivity based on a single-mode-capillary-single-mode fiber structure," *IEEE Photon. J.*, vol. 9, no. 2, pp. 1-8, Apr. 2017.

[4] E. Udd and W. B. Spillman Jr., *Fiber Optics Sensors*. Hoboken, NJ, USA: Wiley, 2011.

[5] C. Zhu *et al.*, "A displacement sensor with centimeter dynamic range and submicrometer resolution based on an optical interferometer," *IEEE Sens. J.*, vol. 17, no. 17, pp. 5523-5528, July 2017.

[6] Y. Zhuang, Y. Chen, C. Zhu, R. E. Gerald, and J. Huang, "Probing changes in tilt angle with 20 nanoradian resolution using an extrinsic Fabry-Perot interferometer-based optical fiber inclinometer," *Opt. Express*, vol. 26, no. 3, pp. 2546-2558, Feb. 2018.

[7] Y. Yang, X. Ma, K. Chen, E. Wang, Z. Yu, and Q. Yu, "A high-resolution dynamic fiber-optic inclinometer," *Sens. Actuators A Phys.,* vol. 283, pp. 305-312, Nov. 2018.

[8] C. Zhu, Y. Chen, Y. Zhuang, G. Fang, X. Liu, and J. Huang, "Optical Interferometric Pressure Sensor Based on a Buckled Beam With Low-Temperature Cross-Sensitivity," *IEEE Trans. Instrum. Meas.*, vol. 67, no. 4, pp. 950-955, Jan. 2018.

[9] Y. Du, Y. Chen, Y. Zhuang, C. Zhu, F. Tang, and J. Huang, "Probing nanostrain via a mechanically designed optical fiber interferometer," *IEEE Photon. Technol. Lett.*, vol. 29, no. 16, pp. 1348-1351, Jun. 2017.

[10] C. Zhu *et al.*, "An optical interferometric triaxial displacement sensor for structural health monitoring: characterization of sliding and debonding for a delamination process," *Sensors*, vol. 17, no. 11, p. 2696, Nov. 2017.

[11] T. Wei, S. Wu, J. Huang, H. Xiao, and J. Fan, "Coaxial cable Bragg grating," *Appl. Phys. Lett.*, vol. 99, no. 11, p. 113517, Sep. 2011.

[12] J. Huang, T. Wei, X. Lan, J. Fan, and H. Xiao, "Coaxial cable Bragg grating sensors for large strain measurement with high accuracy," *Proc. SPIE*, vol. 8345, pp. 83452Z-1–83452Z-9, Apr. 2012.

[13] J. Huang, T. Wang, L. Hua, J. Fan, H. Xiao, and M. Luo, "A coaxial cable Fabry-Perot interferometer for sensing applications," *Sensors*, vol. 13, no. 11, pp. 15252-15260, Nov. 2013.

[14] S. Zeng, A. Trontz, W. Zhu, H. Xiao, and J. Dong, "A metal-ceramic coaxial cable Fabry-Pérot microwave interferometer for monitoring fluid dielectric constant," *Sens. Actuators A Phys.*, vol. 257, pp. 1-7, Apr. 2017.

[15] B. Cheng, L. Yuan, W. Zhu, Y. Song, and H. Xiao, "A coaxial cable magnetic field sensor based on ferrofluid filled Fabry-Perot interferometer structure," *Sens. Actuators A Phys.*, vol. 257, pp. 194-197, Apr. 2017.

[16] J. Huang, T. Wei, T. Wang, J. Fan, and H. Xiao, "Control of critical coupling in a coiled coaxial cable resonator," *Rev. Sci. Instrum.*, vol. 85, no. 5, p. 054701, May. 2014.

[17] G. Hefferman, Z. Chen, and T. Wei, "Two-slot coiled coaxial cable resonator: Reaching critical coupling at a reduced number of coils," *Rev. Sci. Instrum.*, vol. 85, no. 11, p. 115106, Nov. 2014.

[18] J. Huang *et al.*, "Interferogram reconstruction of cascaded coaxial cable Fabry-Pérot interferometers for distributed sensing application," *IEEE Sens. J.*, vol. 16, no. 11, pp. 4495-4500, Feb. 2016.

[19] S. Wu, T. Wei, J. Huang, H. Xiao, and J. Fan, "Modeling of coaxial cable bragg grating by coupled mode theory," *IEEE Trans. Microw. Theory Tech.*, vol. 62, no. 10, pp. 2251-2259, Aug. 2014.

[20] M. F. Ahmed, T. Xue, B. Wu, and J. Huang, "High quality factor coaxial cable Fabry-Perot resonator for sensing applications," *IEEE Sens. J.*, vol. 17, no. 10, pp. 3052-3057, Mar. 2017.

[21] C. Zhu, Y. Chen, Y. Zhuang, and J. Huang, "Displacement and Strain Measurement up to 1000° C Using a Hollow Coaxial Cable Fabry-Perot Resonator," *Sensors*, vol. 18, no. 5, May. 2018.

[22] C. Zhu, Y. Zhuang, Y. Chen, and J. Huang, "A hollow coaxial cable Fabry–Pérot resonator for liquid dielectric constant measurement," *Rev. Sci. Instrum.*, vol. 89, no. 4, p. 045003, Apr. 2018.

[23] C. Zhu, Y. Zhuang, Y. Chen, and J. Huang, "A Liquid-Level Sensor Based on a Hollow Coaxial Cable Fabry-Perot Resonator With Micrometer Resolution," *IEEE Trans. Instrum. Meas.*, no. 99, pp. 1-6, May. 2018.

[24] B. H. Lee *et al.*, "Interferometric fiber optic sensors," *Sensors*, vol. 12, no. 3, pp. 2467-2486, Feb. 2012.

[25] C. Zhu, Y. Chen, Y. Zhuang, and J. Huang, "A Centimeter-Range Displacement Sensor Based on a Hollow Coaxial Cable Fabry–Perot Resonator," *IEEE Sens. J.*, vol. 18, no. 11, pp. 4436-4442, Apr. 2018.

[26] T. W. Athey, M. A. Stuchly, and S. S. Stuchly, "Measurement of radio frequency permittivity of biological tissues with an open-ended coaxial line: Part I," *IEEE Trans. Microw. Theory Tech.*, vol. 30, no. 1, pp. 82-86, Jan. 1982.

[27] J. R. Mosig, J.-C. Besson, M. Gex-Fabry, and F. E. Gardiol, "Reflection of an open-ended coaxial line and application to nondestructive measurement of materials," *IEEE Trans. Instrum. Meas.,* vol. 1001, no. 1, pp. 46-51, Mar. 1981.

[28] D. Popovic *et al.,* "Precision open-ended coaxial probes for in vivo and ex vivo dielectric spectroscopy of biological tissues at microwave frequencies," *IEEE Trans. Microw. Theory Tech.,* vol. 53, no. 5, pp. 1713-1722, May. 2005.

[29] P. De Langhe, K. Blomme, L. Martens, and D. De Zutter, "Measurement of low-permittivity materials based on a spectral-domain analysis for the open-ended coaxial probe," *IEEE Trans. Instrum. Meas.,* vol. 42, no. 5, pp. 879-886, Oct.1993.

[30] P. M. Meaney, A. P. Gregory, J. Seppälä, and T. Lahtinen, "Open-ended coaxial dielectric probe effective penetration depth determination," *IEEE Trans. Microw. Theory Tech.,* vol. 64, no. 3, pp. 915-923, Jan. 2016.

[31] E. Tanabe and W. T. Joines, "A nondestructive method for measuring the complex permittivity of dielectric materials at microwave frequencies using an open transmission line resonator," *IEEE Trans. Instrum. Meas.,* vol. 1001, no. 3, pp. 222-226, Sep. 1976.

[32] D. Xu, L. Liu, and Z. Jiang, "Measurement of the dielectric properties of biological substances using an improved open-ended coaxial line resonator method," *IEEE Trans. Microw. Theory Tech.,* vol. 35, no. 12, pp. 1424-1428, Dec 1987.

[33] M. A. Stuchly and S. S. Stuchly, "Coaxial line reflection methods for measuring dielectric properties of biological substances at radio and microwave frequencies-A review," *IEEE Trans. Instrum. Meas.,* vol. 29, no. 3, pp. 176-183, Sep. 1980.

[34] A. La Gioia *et al.,* "Open-ended coaxial probe technique for dielectric measurement of biological tissues: Challenges and common practices," *Diagnostics,* vol. 8, no. 2, p. 40, Jun. 2018.

[35] J. Z. Bao, M. L. Swicord, and C. C. Davis, "Microwave dielectric characterization of binary mixtures of water, methanol, and ethanol," *The J. Chem. Phys.,* vol. 104, no. 12, pp. 4441-4450, Mar. 1996.

[36] S. Van Damme, A. Franchois, D. De Zutter, and L. Taerwe, "Nondestructive determination of the steel fiber content in concrete slabs with an open-ended coaxial probe," *IEEE Trans. Geosci. Remote Sens.,* vol. 42, no. 11, pp. 2511-2521, Nov. 2004.

[37] N. Wagner, M. Schwing, and A. Scheuermann, "Numerical 3-D FEM and experimental analysis of the open-ended coaxial line technique for microwave dielectric spectroscopy on soil," *IEEE Trans. Geosci. Remote Sens.,* vol. 52, no. 2, pp. 880-893, Mar 2014.

[38] S. Bakhtiari, S. I. Ganchev, and R. Zoughi, "Analysis of radiation from an open-ended coaxial line into stratified dielectrics," *IEEE Trans. Microw. Theory Tech.*, vol. 42, no. 7, pp. 1261-1267, July 1994.

[39] P. De Langhe, L. Martens, and D. De Zutter, "Design rules for an experimental setup using an open-ended coaxial probe based on theoretical modelling," *IEEE Trans. Instrum. Meas.*, vol. 43, no. 6, pp. 810-817, Dec. 1994.

[40] D. M. Pozar, *Microwave Engineering*. New York, NY, USA: Wiley, 2009.

[41] S. Fan, K. Staebell, and D. Misra, "Static analysis of an open-ended coaxial line terminated by layered media," *IEEE Trans. Instrum. Meas.*, vol. 39, no. 2, pp. 435-437, Apr. 1990.

[42] N. Hodgson and H. Weber, *Laser Resonators and Beam Propagation*, 2nd ed. New York, NY, USA: Springer-Verlag, 2005, chs. 8 and 12

[43] J. Fu, X. Wang, T. Wei, M. Wei, and Y. Shen, "A cost-effective geodetic strainmeter based on dual coaxial cable Bragg gratings," *Sensors*, vol. 17, no. 4, p. 842, Apr. 2017.

IV. METAL-ORGANIC FRAMEWORK PORTABLE CHEMICAL SENSOR

ABSTRACT

Combining the chemical-specific adsorption properties of metal-organic framework (MOF) materials with the dielectric sensitivity of a novel open-ended hollow coaxial cable resonator (OE-HCCR), a mechanically-robust and portable gas sensor device (OE-HCCR-MOF) with high chemical selectivity and sensitivity is proposed and experimentally demonstrated. The operating principle of the device is based on changes in the dielectric property of the host MOF layer in response to variations in the types and concentrations of guest molecules. The changes in the dielectric property of the MOF layer modify the phase-matching condition of the microwave resonator, causing shifts in the resonance frequency of the device. By monitoring the resonance frequency shift, the adsorptions of guest molecules can be monitored in real-time and accurately quantified. In proof-of-concept demonstrations, a 200-μm layer of MOF (HKUST-1) was placed within an OE-HCCR to develop a prototype OE-HCCR-MOF sensor. The novel sensor showed high sensitivity to variations in the concentrations of carbon dioxide with good reversibility. The chemical selectivity of the prototype sensor for carbon dioxide compared to methane was also investigated.

1. INTRODUCTION

Sensing common gases and volatile organic compounds (VOCs) with high sensitivity and selectivity is of significant importance for monitoring environmental pollutants, controlling greenhouse gas emissions, and homeland security needs (e.g., detection of harmful or dangerous target analytes at airport check-points) [1]. Gas chromatography-mass spectroscopy (GC-MS) is an effective tool for separating, identifying, and quantifying complex mixtures of gas analytes. However, the utilization of GC-MS methods involves cumbersome instrumentation, troublesome sample condensation, and sophisticated method development [2]. Therefore, innovations that advance reliable, portable, and cost-effective sensors for *in situ* and real-time monitoring of gaseous targets are highly desirable. Nanoporous material-assisted portable sensing devices have gained broad research interest in the past decade. These devices operate based on measurements of changes in the physical/chemical properties of the nanoporous material due to selective chemical interactions or physical adsorption of the target analyte. The high surface-to-volume ratio and high porosity of nanoporous materials enable efficient inclusion of gaseous target analytes inside host materials and thereby drastically improve the measurement sensitivity and facilitates the detection of target analytes down to lower limits [3-6]. One of the most popular and well-established nanoporous materials that have been continuously explored for this application is the zeolite family, a microporous aluminosilicate crystalline material with nanometer-scale or angstrom-scale pore systems [7, 8], which is chemically and thermally stable in harsh-environments. However, zeolite materials present a rather limited variety of chemical functionalities

tailored for adsorption of chemical species due to the challenges of fine-tuning specific pore sizes and chiral channels [9].

Metal-organic frameworks (MOFs) are a newer category of crystalline nanoporous materials that have been extensively investigated recently in the areas of storage of greenhouse gases, gas separation, catalysis, and removal of impurities in natural gas [10-12]. MOFs are formed by the coordination of metal cations and organic linkers. The variety of metal ions, organic linkers, and how the metal ions are joined with the organic linkers provide MOFs with unparalleled design features compared to other classes of nanoporous materials. These design features include a high degree of tunability, structural diversity, and tailorable chemical and physical properties. The possibilities of employing MOFs for sensing applications were only explored recently [1]. Particularly, the tailorable chemical selectivity, as well as high mechanical, thermal, and chemical stability make MOFs appealing to researchers in the fields of chemical sensing and instrumentation.

Optical fibers and coaxial cables are the two most widely used transmission lines in telecommunications for transmitting signals over long distances. Apart from communication applications, the two waveguides have also been investigated as platforms for various sensing purposes, i.e., fiber-optic sensors and coaxial-cable sensors. The surge in popularity of these sensor devices came about because they offer unique features such as high sensitivity, harsh-environment survivability, remote operation, and capability for multiplexing [13-16]. Examples include refractometers for measurements of the dielectric property of an analyte, i.e., fiber-optic refractometers and coaxial-cable devices for dielectric spectroscopy [17-20].

Recent studies revealed that the dielectric properties of MOFs are dependent on the types, amounts, and the states of the molecular guests loaded in the pores of the MOF crystals [21, 22]. Loading and unloading guest molecules in host MOF crystals result in changes in permittivity of the host MOF. Therefore, combining the chemical selectivity of MOFs and the high sensitivity of waveguide-based dielectric spectroscopy might provide a solution for *in-situ*, reliable, low-cost, and rapid detection of target chemicals. However, there is currently limited literature on this topic [23-32]. The majority of existing reports focused on developing optical fiber-based MOF sensors, where thin films of MOF were coated on the cleaved end facet of a telecommunication optical fiber [27, 28] or the cylindrical outer surface of a microstructured optical fiber [23-26, 29-31]. These novel devices are diminutive in size and present prominent sensing performances such as rapid response time (~10 s), low detection limit (~ppm level), and excellent stability and reversibility. The concerning issues of fiber-optic MOF devices include the bonding strength between the MOF thin films and the silica fiber surface, the precise control of the MOF film thickness, the uniformity of the thin films, and the mechanical robustness of the whole sensor head, making mass production and real-world applications of these devices challenging. On the other hand, coaxial-cable sensors, in general, offer much higher mechanical strength and ease of fabrication and thereby provide high potential for mass production [14-16, 19, 20, 33-36]. Open-ended coaxial probes have been extensively investigated, standardized, and commercialized for dielectric spectroscopy at microwave frequencies (i.e., 300 MHz~300 GHz) over the past five decades [18, 37-40]. A dielectric material positioned at the open end of a coaxial transmission line perturbs the fringing electric field and thereby modifies the amplitude and phase of the electromagnetic signals

reflected by the open end. Consequently, the permittivity of the unknown dielectric material can be resolved by analyzing the complex reflection coefficient that characterizes the open end. However, traditional open-ended coaxial cable probes suffer from low measurement sensitivity and resolution and require complicated data analysis. Therefore, a new sensing scheme is desirable to enhance measurement sensitivity. A new scheme should facilitate the combination of MOFs and coaxial-cable sensors for the development of highly-sensitive portable and powerful analytical devices for chemical sensing.

In this work, we propose and demonstrate a porous metal plate-backed open-ended hollow coaxial cable resonator (OE-HCCR) combined with, for the first time, a crystalline MOF dielectric material (OE-HCCR-MOF) for selective gas sensing with high sensitivity. The porous metal plate serves two purposes: (1) It greatly improves the dependence of the fringing electric field on the dielectric material (e.g., MOF) in front of the open end (i.e., it enhances the measurement sensitivity of dielectric spectroscopy by concentrating the fringing electric field); and, (2) It creates a convenient chamber at the open end of the resonator for containing the dielectric MOF layer. The MOF layer not only enables the chemical selectivity of the device but also serves as an analyte concentrator, due to the high surface-to-volume ratio, which enhances the measurement sensitivity of the OE-HCCR-MOF device. The paper continues by deriving a mathematical model of the novel microwave sensing technique and discusses the sensitivity enhancement capability of the device. Experimental results are then presented, based on a prototype chemically-selective OE-HCCR-MOF device, for quantitative measurements of carbon dioxide (CO_2). Finally, the chemical selectivity of the prototype device is further demonstrated by investigating the device's temporal responses to the competitive adsorption of methane (CH_4) and CO_2.

2. METHODS AND MATERIALS

2.1. WORKING PRINCIPLE OF OE-HCCR FOR DIELECTRIC MEASUREMENTS

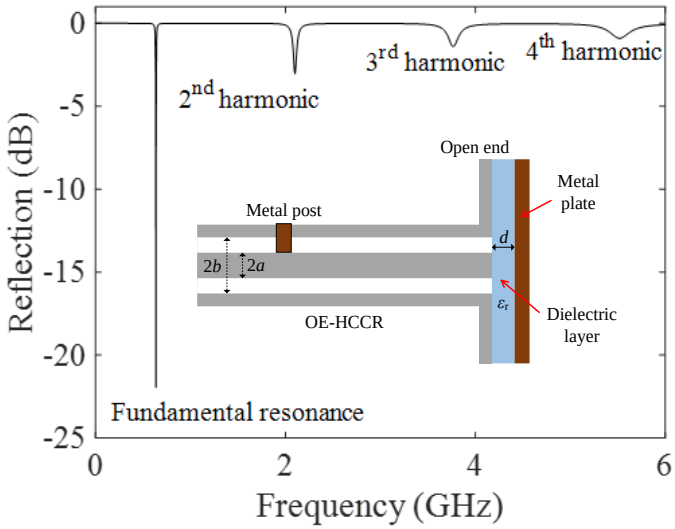

Figure 1. An overview of the OE-HCCR design and signal output. The graph shows a plot of the calculated reflection spectrum of the OE-HCCR. The inset shows a schematic of the cross-section of the OE-HCCR. The OE-HCCR is terminated by a metal plate-backed dielectric layer. The dielectric layer has a thickness of d and a relative permittivity of ϵ_r. The diameters of the inner and outer conductors are denoted as $2a$ and $2b$, respectively. For the numerical calculations, the physical parameters of the OE-HCCR were set to the same parameters used to fabricate the prototype device: a = 3.0 mm; b = 7.0 mm; L = 75 mm (the distance between the metal post and the open end of the coaxial cable); and, D = 3.0 mm (diameter of the metal post). The thickness and the relative permittivity of the dielectric layer were set to 0.2 mm and 1, respectively.

We start by discussing the working principle of the device, the OE-HCCR, for dielectric measurements with high sensitivity. An overview of the OE-HCCR is presented in Figure 1. The (sensor) resonator output response is plotted in Figure 1 as a typical frequency-domain reflection spectrum over a 6 GHz bandwidth. The inset in Figure 1

shows a schematic of the cross-section of the OE-HCCR. Importantly, a conductive metal plate is included in the OE-HCCR as an electric field concentrator and termination plane; the gap between the open end of the coaxial cable and the metal plate is filled with a dielectric layer. The OE-HCCR is designed based on a homemade hollow coaxial cable with air as the dielectric layer for the transmission line. Hollow coaxial cables with air dielectrics have operational advantages at elevated temperatures where conventional dielectrics (e.g., PTFE, PE) are not mechanically and chemically stable for sensing applications in harsh environments. The coaxial cable resonator is formed between two microwave reflectors. A metal post welded within the RF input end shorts the inner conductor and the outer conductor, inducing a large impedance mismatch and serves as the first reflector of the resonator; the open end together with the conductive metal plate-backed dielectric layer serves as the second reflector. Detailed studies of the OE-HCCR can be found in our recent work [41]. Multiple resonance dips can be observed in the resonator output within the observation frequency bandwidth spanning from 10 MHz to 6 GHz, including the fundamental resonance (~0.636 GHz) and higher-order harmonics (i.e., 2^{nd}, 3^{rd}, and 4^{th} harmonics at 2.100 GHz, 3.767 GHz, and 5.519 GHz, respectively). The fundamental resonance dip provides the highest signal-to-noise ratio and is employed as the reference signal for sensing applications. The resonance frequencies (f_{res}) of the OE-HCCR are given by:

$$f_{res} = \frac{c(2m\pi + \phi_1 + \phi_2)}{4\pi L} \tag{1}$$

where c is the speed of light in vacuum; m is a non-negative integer denoting the resonance order; L is the physical distance between the metal post and the open end; ϕ_1 and ϕ_2 are the

phases of the reflection coefficients of the first reflector (i.e., the metal post) and the second reflector (the open end combined with the conductive metal plate-backed dielectric layer), respectively. The fundamental basis for chemical sensing by the OE-HCCR is based on correlating the dielectric property of the layer under test to the resonance frequency (e.g., fundamental resonance frequency). Specifically, the change in permittivity of the dielectric layer modifies the phase reflection coefficient of the open end (ϕ_2), resulting in a change in the resonance frequency of the microwave resonator according to Equation (1). By monitoring shifts of the fundamental resonance frequency, variations of the permittivity of the dielectric layer can be determined. The conductive metal plate further enhances the dependence of the phase reflection coefficient (ϕ_2) on the permittivity of the dielectric layer, as discussed below. We will focus on deriving the mathematical model for ϕ_2; ϕ_1 can be determined using a full-wave simulation.

In our previous work [41], the phase reflection coefficient of the open end was derived as:

$$\phi_2 = -2\tan^{-1}(2\pi f Z_0 C) \tag{2}$$

where f is the frequency of the microwave signal; Z_0 is the characteristic impedance of the coaxial cable; and, C is the static capacitance at the open end that contains the fringing electric field. C is given by [42]:

$$C = \epsilon_r \left\{ \frac{2\epsilon_0}{[\ln(b/a)]^2} \int_a^b \int_a^b \int_0^\pi \frac{\cos\phi'\, d\rho\, d\rho'\, d\phi'}{\sqrt{[\rho^2 + \rho'^2 - 2\rho\rho'\cos\phi']}} + \frac{4\epsilon_0}{[\ln(b/a)]^2} \sum_{n=1}^{\infty} \int_a^b \int_a^b \int_0^\pi \frac{\cos\phi'\, d\rho\, d\rho'\, d\phi'}{\sqrt{[\rho^2 + \rho'^2 + 4n^2d^2 - 2\rho\rho'\cos\phi']}} \right\} \tag{3}$$

where ρ and ρ' denote the radial direction, and ϕ' denotes the azimuthal direction; a and b are the radii of the inner and outer conductors of the coaxial cable; ϵ_0 is the permittivity of vacuum; ϵ_r is the relative permittivity of the material in the gap; and, d is the gap distance between the open end of the coaxial cable and the porous metal plate. We demonstrated that for a given dielectric material, e.g., air (ϵ_r = 1), the static capacitance increases exponentially as the thickness of the air dielectric layer d decreases, resulting in the resonance frequency of the OE-HCCR decreasing exponentially [41]. Examining Equation (3), one realizes that for a given thickness d, the static capacitance C is linearly proportional to the relative permittivity of the dielectric layer. Therefore, Equation (3) can be simplified as:

$$C = \psi(d) \cdot \epsilon_r \tag{4}$$

where $\psi(d)$ corresponds to the part of the equation inside the braces in Equation (3), indicating a linear relationship between the static capacitance and the relative permittivity of the dielectric layer. As discussed above, $\psi(d)$ increases exponentially as the thickness d decreases. As the thickness of the dielectric layer d decreases, the static capacitance C is expected to have a greater dependence on the relative permittivity of the layer. Therefore, the resonance frequency will have a greater dependence on the relative permittivity of the layer. Hence, a decrease in the thickness of the dielectric layer can enhance the sensitivity of the OE-HCCR to variations of the dielectric properties of the layer in front of the open end, revealing a novel sensitivity enhancement mechanism of the OE-HCCR for chemical sensing applications. Figure 2 presents the results of numerical investigations of the sensitivity enhancement mechanism. Figure 2(a) shows the calculated relative shift in the fundamental resonance frequency (i.e., the shift in resonance frequency/initial resonance

frequency, $\Delta f/f$) of the OE-HCCR as a function of the relative permittivity of the dielectric layer for five different settings of the thickness of the dielectric layer, d. As the thickness d decreased from 2 mm to 0.2 mm, larger negative shifts in the resonance frequency were obtained as the relative permittivity of the layer increased from 1 to 5. Nonlinear relationships were revealed as shown in Figure 2(a). Figure 2(b) shows the calculated dielectric measurement sensitivity of the OE-HCCR, i.e., relative frequency shift/change in relative permittivity (changing from 1 to 1.5), as a function of the thickness of the dielectric layer. The dielectric measurement sensitivity increased as the thickness of the dielectric layer decreased, as expected. Figure 2(b) predicts the potential for developing a

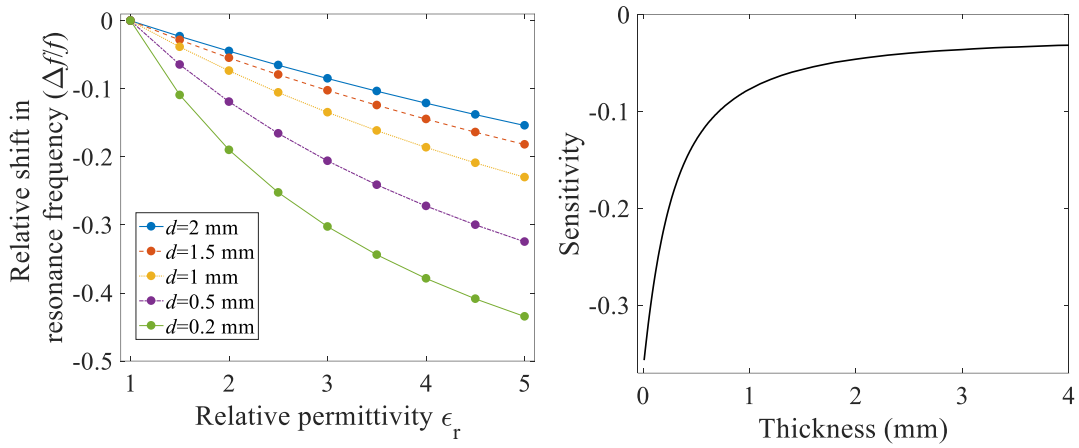

(a) (b)

Figure 2. Numerical investigations of the OE-HCCR for chemical sensing with enhanced sensitivity. (a) The relative shift in the resonance frequency of the OE-HCCR as a function of the relative permittivity of the dielectric layer for five different values of the layer thickness (2, 1.5, 1, 0.5, and 0.2 mm). (b) The dielectric measurement sensitivity of the OE-HCCR as a function of the thickness of the dielectric layer. The measurement sensitivity is obtained by differentiating the relative frequency shift with respect to the change in the relative permittivity of the dielectric layer (increment of 0.5, increasing from 1 to 1.5).

highly-sensitive chemical sensor based on the OE-HCCR. A proof of concept for the dielectric sensitivity enhancement can be found in our recent work [43]. The limit of detection of the prototype OE-HCCR with respect to a change in relative permittivity of the dielectric layer in the gap is estimated to be approximately 4 ppm given that a change in the resonance frequency can be resolved to 1 kHz by a state-of-the-art RF interrogator.

2.2. OE-HCCR-MOF SENSOR DESIGN

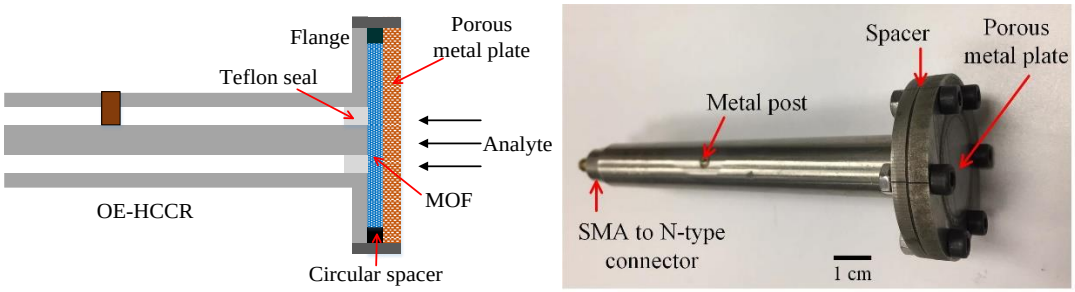

(a) (b)

Figure 3. The OE-HCCR-MOF gas sensor. (a) A schematic of the probe. The thickness of the MOF layer is defined by the thickness of the circular spacer (i.e., a gasket), which can be varied by using spacers with different thicknesses. A porous metal plate was used to back the MOF layer and allow the gas analyte to enter into the MOF layer. (b) A photograph of a prototype probe. The prototype OE-HCCR-MOF probe was fabricated using a homemade hollow coaxial cable made of stainless steel, which can be connected to a commercial 50-Ω coaxial cable using an SMA to N-type connector.

Based on the OE-HCCR platform, a highly-sensitive gas sensor was invented, the OE-HCCR-MOF probe. An overview of the OE-HCCR-MOF probe is presented in Figure 3, including a schematic and a photograph of a prototype probe. Figure 3(a) shows a schematic of the proposed gas sensor based on an OE-HCCR and a thin layer of metal-organic framework (MOF) placed within the gap volume. The thin layer of MOF powder

(~200 μm thickness, commercial HKUST-1) filled the gap between the microporous metal plate and the open end of the coaxial cable. Note that the thickness of the MOF is defined by the thickness of the circular spacer (i.e., a gasket) and can be varied by using spacers with different thicknesses. In the sensor design, the thickness of the dielectric layer (MOF) was designed to be 0.2 mm because this setting offers a relatively high measurement sensitivity (see Figure 2). Over a small dynamic range (e.g., ~0.2 change in permittivity), the relationship between the frequency shift and variations in permittivity of the dielectric layer can be considered a linear function. Figure 3(b) shows a photograph of a prototype device. The center part of the porous metal plate was made of PM-35 permeable steel with pore sizes of 25±15 μm. The OE-HCCR was used to interrogate changes in the relative permittivity of the MOF layer due to the adsorption of guest molecules from the surrounding environment. Specifically, since the MOF has a large surface-to-volume ratio and most of the MOF's volume consists of open pores, adsorption of guest molecules from the surrounding environment into these open pores will increase the relative permittivity of the guest-loaded MOF layer. Consequently, the responses from all of the empty or filled pores are summed to produce permittivity changes by the entire guest-loaded MOF layer. The change in the relative permittivity of the MOF layer results in the variation of the total capacitance at the open end, leading to a change in the phase reflection coefficient associated with the open end. The change in the phase reflection coefficient at the open end will change the phase-matching condition of the microwave cavity resonator and thereby shift the resonance frequency. Therefore, by tracking the shift of the resonance frequency, the overall change in the relative permittivity of the MOF layer can be monitored in real-time. In other words, the changes in the overall relative permittivity of

the MOF layer, induced by the loading and unloading of guest molecules within the porous structure can, in turn, be employed to measure the temporal process of guest adsorption and desorption. Furthermore, it is possible to determine the concentration of the guests in the host (after sensor calibration) at any time by simply tracking the resonance frequency shift of the microwave cavity resonator.

2.3. MATERIAL

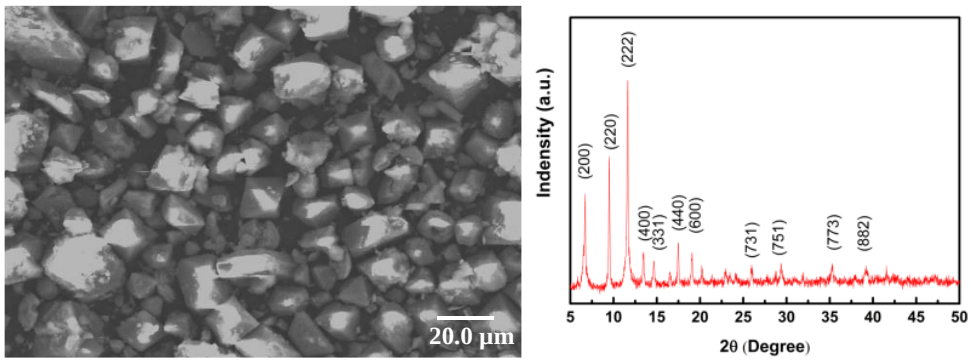

(a) (b)

Figure 4. Characterization of HKUST-1 MOF powder sourced from ACS Material LLC. (a) An SEM image of the commercial HKUST-1. (b) XRD spectra of the commercial HKUST-1 [44].

The MOF used in the prototype device was HKUST-1, purchased from ACS Material LLC (Pasadena CA, USA). The MOF was prepared by a hydrothermal method and yielded particles ranging in size from 10 to 20 µm. The MOF pore size was approximately 0.6 nm. The tapped density of the MOF powder was ~0.45 g/ml. Figure 4 contains characterization information of the MOF powder obtained from ACS Material LLC [44], including an SEM image and X-Ray diffraction (XRD) analysis results. Discrete

intensive diffraction peaks at 200, 220, 222, 400, etc., were observed in the XRD spectra. The XRD spectra were measured with Cu Kα radiation. HKUST-1 was chosen for our proof-of-concept demonstration because it has well-known physical and chemical properties (e.g., CO_2 selectivity), and is commercially available. It is also a well-behaved dielectric material such that variations of the dielectric property due to loading and unloading of guest molecules can be interrogated using the microwave probe.

2.4. EXPERIMENTAL SETUP

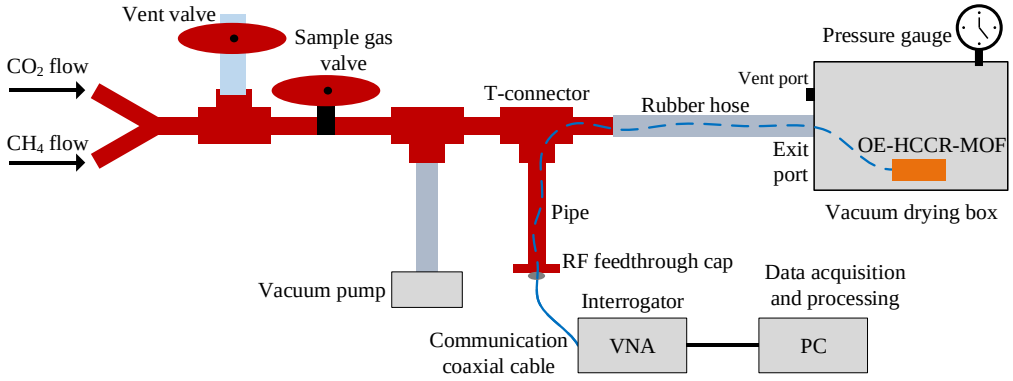

Figure 5. Schematic of the experimental setup employed for gas adsorption tests using the OE-HCCR-MOF sensor. The OE-HCCR-MOF sensor was tested in a vacuum drying box where the composition of the gas atmosphere and the temperature was controlled.

The experimental setup for demonstrating the gas sensing capability of the prototype OE-HCCR-MOF device is illustrated in Figure 5. The OE-HCCR-MOF sensor was connected to a vector network analyzer (VNA, Agilent 8753ES) via a communication coaxial cable through the vacuum tubing as shown in Figure 5. The sensor was placed in a vacuum drying box where the ambient atmosphere (0.1-1.0, ±0.1 atm) and the temperature (290-500, ±3 K) could be controlled by built-in heating and cooling accessories. A vacuum

pressure gauge was also connected to the vacuum drying box to measure the pressure. The exit port of the vacuum drying box was connected to a home-built manifold, through which the box could be evacuated using a vacuum pump (EasyVac-7, ACROSS INTERNATIONAL) and gases of interest (e.g., CO_2 and CH_4) could be injected into the box for adsorption studies.

3. RESULTS

A series of reflection spectra near the fundamental resonance frequency for the prototype sensor device is shown in Figure 6. The red-dashed curve represents the reflection spectrum of the prototype device before the gap between the open end and the metal plate was filled with the MOF layer, i.e., the gap was filled with a layer of air dielectric; the solid blue and yellow curves correspond to the reflection spectra of the prototype OE-HCCR-MOF device before and after thermal activation (TA) of the MOF layer, respectively. After the air gap between the open end and the metal plate was filled with a MOF layer, the resonance frequency (i.e., the dip in the reflection spectrum) of the device shifted to the lower frequency region, as expected, since the MOF has a larger relative permittivity ($\epsilon_r \sim 2$) compared to air ($\epsilon_r \sim 1$) in the interrogation frequency regime. After thermal activation of the MOF, the resonance frequency of the device shifted to a higher frequency. This observation is reasonable because the evacuation of the adsorbed molecules (e.g., H_2O, CO_2) in the interior MOF volume during TA resulted in a decrease in the relative permittivity of the MOF layer. The quality-factor (Q-factor) of the reflection spectrum decreased greatly as the gap between the open end and the metal plate was filled

with the MOF layer (before TA). After TA, the Q-factor increased, indicating that the MOF became less lossy to the microwave signal since the polarizable water molecules were evacuated.

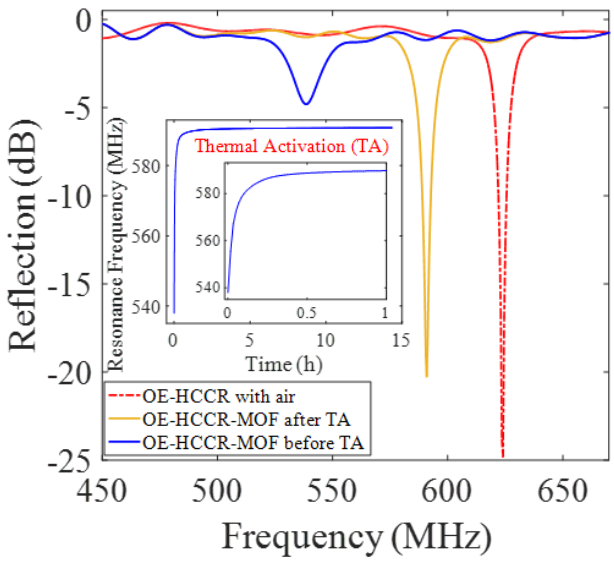

Figure 6. Reflection spectra in the region of the fundamental resonance frequency for the prototype OE-HCCR-MOF sensor device under different conditions of the MOF layer dielectric. The red-dashed curve represents the reflection spectrum of the prototype device *before* the MOF layer was filled in the gap between the open end and the metal plate, i.e., the gap was filled with a layer of air dielectric. The solid blue and yellow curves represent the reflection spectra of the prototype device with a layer of MOF filled in the gap before and after the thermal activation (TA) process, respectively. The inset shows the evolution of the resonance frequency of the OE-HCCR-MOF sensor during the overnight TA process; an expanded view of the first hour of the TA process is also shown.

The inset in Figure 6 shows the continuously-monitored evolution of the resonance frequency of the OE-HCCR-MOF device during the overnight TA process; an expanded view of the first hour of the TA process is also shown. The resonance frequency of the OE-HCCR-MOF sensor device stabilized at approximately 592 MHz after TA. The resonance

frequency of the OE-HCCR with air filling the gap between the open end and the metal plate was found to be 624 MHz, which differed from the calculated frequency of 636 MHz. This discrepancy is primarily due to the Teflon seal in the prototype device, which was not considered in the calculation. After TA, the OE-HCCR-MOF resonated at 592 MHz, indicating that a decrease of 32 MHz in resonance frequency was observed as the dielectric changed from air to the MOF. According to numerical calculations, the effective relative permittivity of the dehydrated HKUST-1 layer was estimated to be ~1.29 at ~590 MHz. The effective relative permittivity of the hydrated HKUST-1 layer (i.e., the MOF layer before TA) was estimated to be ~1.76 at ~550 MHz.

The detection of CO_2 gas using the OE-HCCR-MOF sensor was first demonstrated at room temperature (~23°C). In the experiment, the box was first evacuated until the reflection spectrum of the sensor stabilized, indicating that the MOF layer was fully activated. Then the box was backfilled with pure CO_2 gas to reach the desired pressure inside the vacuum box for the adsorption test. The reflection spectrum was monitored *in situ* and data processing was performed to determine the response of the OE-HCCR-MOF sensor (i.e., resonance frequency shift) in real-time. Each measurement took approximately 3 seconds for the interrogation and data-processing. After the sensor stabilized (no frequency shift), the box was evacuated again and another volume of CO_2 was allowed to flow into the box (i.e., at another pressure setting), followed by a re-measurement. The experimental results for the CO_2 adsorption tests are presented in Figure 7. Figure 7(a) shows the absolute value of the measured resonance frequency shift (Δf) as a function of time for five different settings of CO_2 pressure inside the hermetically-sealed vacuum drying box. The evolution of the resonance frequency revealed a strong dependence of the

relative permittivity of the MOF layer on the concentration of CO_2 in the surrounding atmosphere. After approximately four minutes, the resonance frequency of the sensor no longer shifted, revealing an equilibrium state of the guest/host system (CO_2@MOF). Figure 7(b) shows the shift in the resonance frequency (Δf) as a function of CO_2 pressure at steady-state conditions. Higher pressures of CO_2 (i.e., higher concentrations) in the vacuum drying box resulted in larger frequency shifts, consistent with larger increases in the relative permittivity of the MOF layer due to the adsorption of CO_2. Given the probe resonated at ~592 MHz, the averaged sensitivity, i.e., relative resonance frequency shift vs. change in pressure, was determined to be approximately -0.003/atm. The effective relative permittivity of the MOF layer after adsorption of CO_2 at a pressure setting of 1 atm increased by approximately 0.012. Note that the response curve of the OE-HCCR (i.e., without the MOF layer in the gap between the open end and the metal plate) was also included as a control experiment in Figure 7(b) for comparison. The resonance frequency shifted by approximately 0.050 MHz as the pressure of CO_2 increased from 0 to 1.0 atm, which only accounted for 3% of the response of the OE-HCCR-MOF device (the case where the MOF layer was included). Therefore, the use of the MOF layer improved the gas sensing sensitivity of the OE-HCCR for CO_2. The experimental results demonstrated that the prototype OE-HCCR-MOF device could be employed for highly-sensitive and quantitative detection of CO_2 after proper calibration. Note that the measurement sensitivity of the OE-HCCR-MOF sensor also relies on the adsorption capacity of the MOF material, the higher the adsorption capacity, the larger the sensitivity [32]. The CO_2 sensitivity of the prototype OE-HCCR-MOF sensor was comparable to the CO_2 sensitivity reported in [32] where a microwave active-resonator and MOF-199-M2 were used.

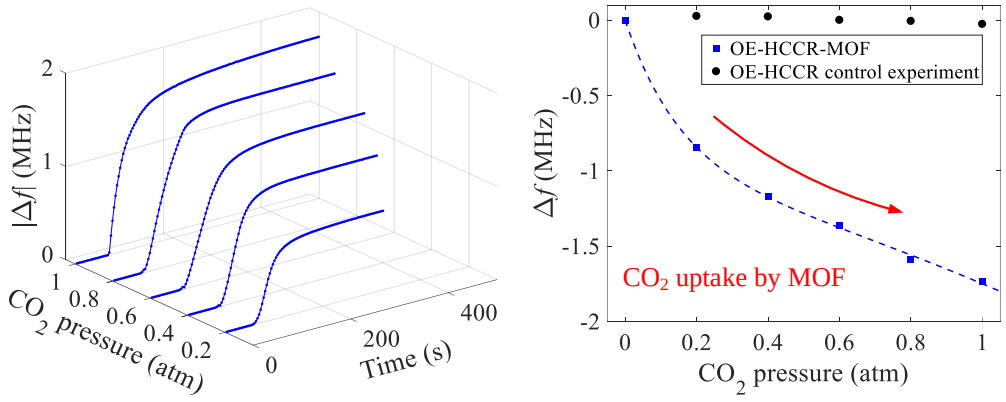

(a) (b)

Figure 7. Adsorption tests of CO_2 by HKUST-1 using the OE-HCCR-MOF sensor at room temperature (23°C). (a) The evolution of the resonance frequency of the sensor for different CO_2 pressures in the vacuum drying box. (b) The resonance frequency shift (Δf) of the OE-HCCR-MOF sensor at steady-state conditions as a function of the CO_2 pressure in the box (blue solid squares). The frequency decreased by ~1.74 MHz overall for the pressure range 0-1.0 atm of the CO_2 gas atmosphere. The responses of the OE-HCCR (without the MOF layer in the gap between the metal plate and the open end) were also included as a control experiment, showing a frequency shift of approximately 0.050 MHz as the CO_2 pressure increased from 0 to 1.0 atm (black solid circles). The blue-dashed curve is fitted using an exponential model and included to guide the eye.

The reproducibility of the OE-HCCR-MOF sensor was demonstrated by repeating the evacuation/backfill process using CO_2 gas. CO_2 gas was injected into the vacuum drying box until the pressure reached 1.0 atm, followed by evacuation after an equilibrium state was reached. Figure 8 shows the resonance frequency shift (Δf) as a function of time during the test. The OE-HCCR-MOF device exhibited completely reversible and fast response times for adsorption/desorption of CO_2. The resonance frequency of the sensor decreased as CO_2 was injected into the vacuum drying box and plateaued after approximately four minutes, indicating that equilibrium was reached in the system. The resonance frequency increased as the vacuum drying box was evacuated due to the removal

of the CO_2 adsorbed in the pores of the MOF. After the vacuum drying box was evacuated for approximately ten minutes, the resonance frequency returned to the initial value, indicating that all of the adsorped CO_2 was removed from the pores. The four-cycle evacuation/backfill test demonstrated good signal reproducibility by the prototype OE-HCCR-MOF sensor device. Note that the response time of the probe device for CO_2 adsorption is expected to be faster than the time shown in Figure 8 (~a few minutes) because the volume of the vacuum drying box used in the experiment was large and additional time was required for the CO_2 pressure to reach 1.0 atm in the box.

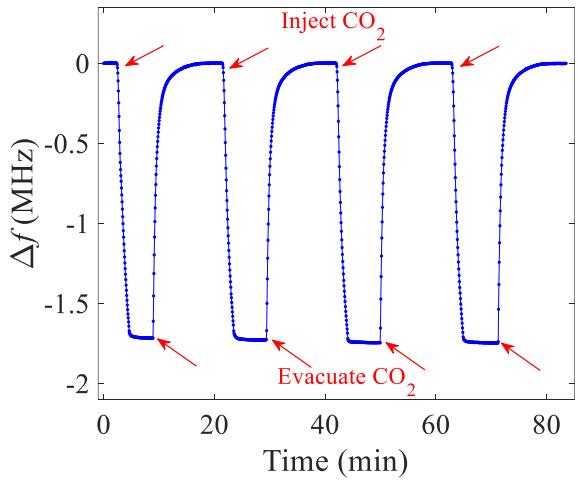

Figure 8. Signal reproducibility test of the OE-HCCR-MOF sensor for adsorption of CO_2 by HKUST-1. CO_2 gas was injected into the vacuum drying box until the pressure reached 1.0 atm, followed by the evacuation of the gas after an equilibrium state was reached. The OE-HCCR-MOF device exhibited completely reversible and fast response times for the adsorption/desorption of CO_2 by the MOF throughout the four-cycle evacuation/backfill test.

Further experiments were performed to demonstrate the selectivity of the prototype OE-HCCR-MOF probe when utilized for gas sensing. Since it was previously reported that HKUST-1 has a differential CO_2/CH_4 selectivity, with a greater adsorption propensity for

CO_2 [45], both gases were employed as the guest molecules to demonstrate the capability of the prototype OE-HCCR-MOF gas sensor for competitive chemical selectivity. In a competitive gas adsorption experiment, the vacuum drying box was first evacuated to avoid interferences caused by other vapors (e.g., humidified air) and then continuous flows of pure CH_4 and pure CO_2 gases were alternately directed into the box. The vent port was kept open to maintain the pressure in the box at 1.0 atm. For each gas (CH_4 or CO_2), the equilibrium state of the guest-loaded MOF was reached before switching to the flow of the other gas. Figure 9 shows the recorded temporal evolution of the resonance frequency shift (Δf) during the competitive gas adsorption demonstration test. When CH_4 gas first directed into the box, the resonance frequency of the device decreased due to the adsorption of CH_4 molecules in the pores of the MOF and then plateaued, as expected. The injection of CO_2 gas resulted in further decreases in the resonance frequency. The decreasing trend of the resonance frequency was reasonable since the HKUST-1 layer has a larger adsorption propensity for CO_2 compared to CH_4 and CO_2 gas adsorption by the MOF layer causes a larger frequency shift. An increase in the density of diamagnetic guests and the consequent change in the relative permittivity of the MOF layer were expected to occur when CO_2 replaced CH_4. After the sensor stabilized in a 100% CO_2 environment, the input gas was switched to CH_4. As CH_4 replaced CO_2 in the pores of the MOF layer (due to the large excess of CH_4 in the vacuum drying box), the relative permittivity of the MOF layer decreased due to the smaller adsorption propensity by the MOF for CH_4, increasing the resonance frequency. We found that less than 10 minutes were required for CO_2 to replace CH_4 in the pores of the MOF layer; conversely, approximately 50 minutes were required for CH_4 to replace CO_2 in the MOF pores. The time response verified that the MOF powder

(HKUST-1) in the OE-HCCR-MOF sensor had a larger adsorption propensity for CO_2, which matched well with previous studies [45].

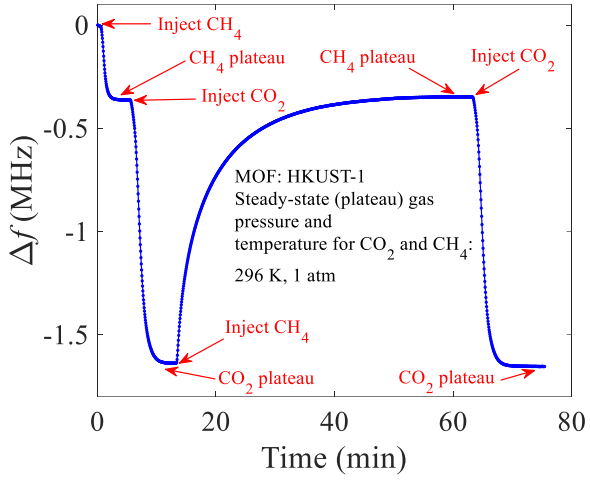

Figure 9. A demonstration test of the competitive gas adsorption between CH_4 and CO_2 in HKUST-1. The evolution of the resonance frequency of the OE-HCCR-MOF sensor when CH_4 and CO_2 were alternately directed into the vacuum drying box, bathing the MOF dielectric. For each gas, the equilibrium state (plateau) was reached before switching to the other gas. Both the magnitudes of the frequency shifts and the time responses demonstrated that the MOF layer exhibited a larger adsorption propensity for CO_2 compared to CH_4.

4. DISCUSSIONS

The present work demonstrated a novel chemical sensor platform, the open-ended coaxial cable resonator (OE-HCCR). With the coupling of the OE-HCCR to a microporous MOF-crystal layer, a new gas sensor probe, the OE-HCCR-MOF, was formed. The MOF-crystal layer used in the demonstration was the commercially available HKUST-1 MOF. The OE-HCCR-MOF probe is a sensitive, low-cost, easy-to-fabricate, user-configurable, robust, and portable chemical sensor with quantitative chemical selectivity and real-time

monitoring capability. Different dielectric MOFs targeting specific analytes can be easily integrated into the sensor platform, offering a universal strategy for chemical sensing applications. Currently, the interrogator unit for the device used in the demonstration is a benchtop VNA. However, there are various portable VNAs (e.g., Anritsu MS46121B) that also offer good performance. Alternatively, a positive feedback system can be built to interrogate the OE-HCCR-MOF probe to further decrease the size and the system cost of the interrogation unit [46]. The proposed OE-HCCR is essentially a scientific advancement of the well-known open-ended coaxial probes. By fabricating a resonating structure from an all-metal hollow coaxial cable, the resultant OE-HCCR provides additional advantages, including ease of signal processing, improved dielectric sensitivity, and enhanced mechanical robustness. The proposed OE-HCCR provides a novel route for developing a new generation of coaxial cable-based gas sensors. Compared to other microwave gas sensors, e.g., planar ring resonators [47], cavity resonators [48], and capacitive resonators [49], the OE-HCCR is featured in a ruggedized all-metal structure, which makes it a portable device and suitable for sensing applications in elevated-temperature harsh environments. Note that the prototype OE-HCCR shown in this work is relatively bulky. The size dimensions of the hollow coaxial cable (i.e., the diameters of the inner and outer conductors) can be further reduced based on transmission line theory. The distance between the metal post and the open end of the coaxial cable (L) can be reduced to the mm-scale. The reduction in the size dimensions of the OE-HCCR will increase the operating frequency. On the other hand, the operating frequency can also be tuned by adjusting the initial gap distance between the open end of the coaxial cable and the porous metal plate [41].

It is well known that some MOFs, e.g., HKUST-1, can strongly adsorb water molecules from the ambient environment and that the adsorbed water molecules will block the specific affinity of the MOFs for CO_2 molecules [50]. The presence of N_2, O_2, or dry air will not interfere with the detection of the analyte of interest, e.g., CO_2. The porous structure of HKUST-1 could change irreversibly, i.e., collapse, due to water absorption, degrading the performance of the MOF-based sensor probe. In fact, in our investigations, an OE-HCCR-MOF prototype device with HKUST-1 as the MOF layer was exposed to open-air conditions for nine months. The sensing performance was then tested by investigating the sensor response to CO_2. The device exhibited an approximately 1 MHz shift in the resonance frequency as the CO_2 pressure increased from 0 to 1.0 atm. The measured frequency shift, i.e., 1 MHz, was ~ 57% of the frequency shift for the device shown in Figure 7, where a fresh MOF layer dielectric was employed. The decrease in the magnitude of the frequency shift indicated reduced adsorption of CO_2. We postulate that the main reason for the diminished change in the frequency shift upon CO_2 adsorption was due to the collapse or other modifications of the porous structure in the MOF because of water adsorption from the ambient environment. Therefore, additional protection of the sensor probe should be considered in order to prevent humidity from interfering and degrading the probe's sensing capability. For instance, a layer of regenerable desiccant can be coated on the outside surface of the porous metal plate so that the water molecules could be adsorbed by the desiccant layer [51] and the water-free gaseous analyte could then enter the MOF layer. Furthermore, the temperature crosstalk should be investigated since the OE-HCCR-MOF device essentially functions based on the principles of dielectric spectroscopy, and temperature variations could change the dielectric property of the MOF

layer. We envision that a differential method can be employed by using a reference resonator for temperature compensation [52]. Further studies and optimizations of the OE-HCCR-MOF device are underway.

5. CONCLUSIONS

We have invented and demonstrated a novel probe that combines a dielectric composed of a MOF layer (HKUST-1) with tailored chemical properties and a novel open ended-hollow coaxial cable resonator (OE-HCCR) for sensitive and selective chemical sensing applications. We demonstrated that the adsorption and desorption of guest molecules in the MOF host system resulted in changes to the dielectric property of the MOF layer. The variations of the dielectric property of the MOF layer can be accurately determined by monitoring shifts of the resonance frequency of the microwave resonator in real-time. In addition to a layer made of MOF powders, a MOF single-crystal can also be integrated within the active volume of the OE-HCCR. The resultant OE-HCCR-single-crystal-MOF device may provide a potential route to probe the weighted positions and orientations of guest molecules in the pores of MOF using different electric field polarizations for interrogation. The proposed OE-HCCR-MOF is essentially a new portable chemical sensor platform, and its capability for dielectric measurements could find potential applications in various chemical fields due to its high sensitivity, chemical selectivity, robustness, ease of fabrication, user-configurability, and ease of signal interrogation. The proposed OE-HCCR-MOF structure paves the way for developing a new generation of low-cost, real-time, portable, and powerful *in situ* devices for chemical

analyses. A promising application of the OE-HCCR-MOF device is the detection of VOCs for diagnosis of chronic diseases in medical applications; the OE-HCCR would virtually function as an electronic nose [53].

REFERENCES

[1] L. E. Kreno, K. Leong, O. K. Farha, M. Allendorf, R. P. Van Duyne, and J. T. Hupp, "Metal–organic framework materials as chemical sensors," Chem. Rev., vol. 112, no. 2, pp. 1105-1125, 2011.

[2] A. H. Khoshaman and B. Bahreyni, "Application of metal organic framework crystals for sensing of volatile organic gases," *Sensors and Actuators B: Chemical,* vol. 162, no. 1, pp. 114-119, 2012.

[3] P. Kumar, A. Deep, and K.-H. Kim, "Metal organic frameworks for sensing applications," *TrAC Trends in Analytical Chemistry,* vol. 73, pp. 39-53, 2015.

[4] M. H. Zarifi, P. Shariaty, Z. Hashisho, and M. Daneshmand, "A non-contact microwave sensor for monitoring the interaction of zeolite 13X with CO2 and CH4 in gaseous streams," *Sensors and Actuators B: Chemical,* vol. 238, pp. 1240-1247, 2017.

[5] M. Fayaz *et al.*, "Monitoring the residual capacity of activated carbon in an emission abatement system using a non-contact, high resolution microwave resonator sensor," *Sensors and Actuators B: Chemical,* vol. 282, pp. 218-224, 2019.

[6] N. R. Tanguy, B. Wiltshire, M. Arjmand, M. H. Zarifi, and N. Yan, "Highly Sensitive and Contactless Ammonia Detection Based on Nanocomposites of Phosphate-Functionalized Reduced Graphene Oxide/Polyaniline Immobilized on Microstrip Resonators," *ACS Applied Materials & Interfaces,* vol. 12, no. 8, pp. 9746-9754, 2020.

[7] H. Xiao, J. Zhang, J. Dong, M. Luo, R. Lee, and V. Romero, "Synthesis of MFI zeolite films on optical fibers for detection of chemical vapors," *Opt. Lett.*, vol. 30, no. 11, pp. 1270-1272, 2005.

[8] J. Zhang, X. Tang, J. Dong, T. Wei, and H. Xiao, "Zeolite thin film-coated long period fiber grating sensor for measuring trace organic vapors," *Sensors and Actuators B: Chemical,* vol. 135, no. 2, pp. 420-425, 2009.

[9] A. Venkatasubramanian, J.-H. Lee, R. J. Houk, M. D. Allendorf, S. Nair, and P. J. Hesketh, "Characterization of HKUST-1 crystals and their application to MEMS microcantilever array sensors," *ECS Transactions,* vol. 33, no. 8, pp. 229-238, 2010.

[10] J. R. Long and O. M. Yaghi, "The pervasive chemistry of metal–organic frameworks," *Chem. Soc. Rev.,* vol. 38, no. 5, pp. 1213-1214, 2009.

[11] J. Lee, O. K. Farha, J. Roberts, K. A. Scheidt, S. T. Nguyen, and J. T. Hupp, "Metal–organic framework materials as catalysts," *Chem. Soc. Rev.,* vol. 38, no. 5, pp. 1450-1459, 2009.

[12] U. Mueller, M. Schubert, F. Teich, H. Puetter, K. Schierle-Arndt, and J. Pastre, "Metal–organic frameworks—prospective industrial applications," *J. Mater. Chem.,* vol. 16, no. 7, pp. 626-636, 2006.

[13] E. Udd and W. B. Spillman Jr, Fiber optic sensors: an introduction for engineers and scientists. John Wiley & Sons, 2011.

[14] J. Huang, T. Wang, L. Hua, J. Fan, H. Xiao, and M. Luo, "A coaxial cable Fabry-Perot interferometer for sensing applications," *Sensors,* vol. 13, no. 11, pp. 15252-15260, 2013.

[15] T. Wei, S. Wu, J. Huang, H. Xiao, and J. Fan, "Coaxial cable Bragg grating," *Appl. Phys. Lett.,* vol. 99, no. 11, p. 113517, 2011.

[16] C. Zhu, Y. Chen, Y. Zhuang, and J. Huang, "A centimeter-range displacement sensor based on a hollow coaxial cable Fabry–Perot resonator," *IEEE Sens. J.,* vol. 18, no. 11, pp. 4436-4442, 2018.

[17] A. Urrutia, I. D. Villar, P. Zubiate, and C. R. Zamarreño, "A Comprehensive Review of Optical Fiber Refractometers: Toward a Standard Comparative Criterion," *Laser & Photonics Reviews,* p. 1900094, 2019.

[18] M. A. Stuchly and S. S. Stuchly, "Coaxial line reflection methods for measuring dielectric properties of biological substances at radio and microwave frequencies-A review," *IEEE Trans. Instrum. Meas.,* vol. 29, no. 3, pp. 176-183, 1980.

[19] C. Zhu, Y. Zhuang, Y. Chen, and J. Huang, "A hollow coaxial cable Fabry–Pérot resonator for liquid dielectric constant measurement," *Rev. Sci. Instrum.,* vol. 89, no. 4, p. 045003, 2018.

[20] S. Zeng, A. Trontz, Z. Cao, H. Xiao, and J. Dong, "Characterizing the gas adsorption-dependent dielectric constant for silicalite nanoparticles at microwave frequencies by a coaxial cable Fabry-Pérot interferometric sensing method," *Madridge J. Nanotechn. Nanosci,* vol. 3, no. 1, pp. 100-107, 2018.

[21] S. Eslava *et al.,* "Metal-organic framework ZIF-8 films as low-κ dielectrics in microelectronics," *Chem. Mater.,* vol. 25, no. 1, pp. 27-33, 2012.

[22] G. Lu and J. T. Hupp, "Metal− organic frameworks as sensors: a ZIF-8 based Fabry− Pérot device as a selective sensor for chemical vapors and gases," *J. Am. Chem. Soc.,* vol. 132, no. 23, pp. 7832-7833, 2010.

[23] J. Hromadka, B. Tokay, S. James, R. P. Tatam, and S. Korposh, "Optical fibre long period grating gas sensor modified with metal organic framework thin films," *Sensors and Actuators B: Chemical,* vol. 221, pp. 891-899, 2015.

[24] K.-J. Kim, P. Lu, J. T. Culp, and P. R. Ohodnicki, "Metal–organic framework thin film coated optical fiber sensors: a novel waveguide-based chemical sensing platform," *ACS sensors,* vol. 3, no. 2, pp. 386-394, 2018.

[25] X. Chong *et al.,* "Near-infrared absorption gas sensing with metal-organic framework on optical fibers," *Sensors and Actuators B: Chemical,* vol. 232, pp. 43-51, 2016.

[26] J. Hromadka, B. Tokay, R. Correia, S. P. Morgan, and S. Korposh, "Highly sensitive volatile organic compounds vapour measurements using a long period grating optical fibre sensor coated with metal organic framework ZIF-8," *Sensors and Actuators B: Chemical,* vol. 260, pp. 685-692, 2018.

[27] M. Nazari *et al.,* "UiO-66 MOF end-face-coated optical fiber in aqueous contaminant detection," *Opt. Lett.,* vol. 41, no. 8, pp. 1696-1699, 2016.

[28] C. Zhu, J. A. Perman, R. E. Gerald, S. Ma, and J. Huang, "Chemical Detection Using a Metal–Organic Framework Single Crystal Coupled to an Optical Fiber," *ACS applied materials & interfaces,* vol. 11, no. 4, pp. 4393-4398, 2019.

[29] J. Hromadka, B. Tokay, R. Correia, S. P. Morgan, and S. Korposh, "Carbon dioxide measurements using long period grating optical fibre sensor coated with metal organic framework HKUST-1," *Sensors and Actuators B: Chemical,* vol. 255, pp. 2483-2494, 2018.

[30] E. Miliutina *et al.,* "Fast and All-Optical Hydrogen Sensor Based on Gold-Coated Optical Fiber Functionalized with Metal-Organic Framework Layer," *ACS sensors,* 2019.

[31] K.-J. Kim *et al.,* "Alkylamine-Integrated Metal–Organic Framework-Based Waveguide Sensors for Efficient Detection of Carbon Dioxide from Humid Gas Streams," *ACS applied materials & interfaces,* vol. 11, no. 36, pp. 33489-33496, 2019.

[32] M. H. Zarifi, A. Gholidoust, M. Abdolrazzaghi, P. Shariaty, Z. Hashisho, and M. Daneshmand, "Sensitivity enhancement in planar microwave active-resonator using metal organic framework for CO2 detection," *Sensors and Actuators B: Chemical,* vol. 255, pp. 1561-1568, 2018.

[33] C. Zhu, Y. Zhuang, Y. Chen, and J. Huang, "A liquid-level sensor based on a hollow coaxial cable Fabry–Perot resonator with micrometer resolution," *IEEE Trans. Instrum. Meas.,* vol. 67, no. 12, pp. 2892-2897, 2018.

[34] C. Zhu, Y. Zhuang, Y. Chen, B. Zhang, and J. Huang, "Contactless liquid interface measurement based on a hollow coaxial cable resonator," *Sens. Actuators A Phys.,* vol. 285, pp. 623-627, 2019.

[35] C. Zhu, Y. Chen, Y. Zhuang, and J. Huang, "Displacement and Strain Measurement up to 1000° C Using a Hollow Coaxial Cable Fabry-Perot Resonator," *Sensors (Basel, Switzerland),* vol. 18, no. 5, 2018.

[36] S. Zeng, A. Trontz, W. Zhu, H. Xiao, and J. Dong, "A metal-ceramic coaxial cable Fabry-Pérot microwave interferometer for monitoring fluid dielectric constant," *Sens. Actuators A Phys.,* vol. 257, pp. 1-7, 2017.

[37] P. De Langhe, K. Blomme, L. Martens, and D. De Zutter, "Measurement of low-permittivity materials based on a spectral-domain analysis for the open-ended coaxial probe," *IEEE Trans. Instrum. Meas.,* vol. 42, no. 5, pp. 879-886, 1993.

[38] A. La Gioia *et al.*, "Open-ended coaxial probe technique for dielectric measurement of biological tissues: Challenges and common practices," *Diagnostics,* vol. 8, no. 2, p. 40, 2018.

[39] D. Xu, L. Liu, and Z. Jiang, "Measurement of the dielectric properties of biological substances using an improved open-ended coaxial line resonator method," *IEEE Trans. Microw. Theory Tech.,* vol. 35, no. 12, pp. 1424-1428, 1987.

[40] S. Fan and D. Misra, "A study on the metal-flanged open-ended coaxial line terminating in a conductor-backed dielectric layer," in *7th IEEE Conference on Instrumentation and Measurement Technology,* 1990: IEEE, pp. 43-46.

[41] C. Zhu, R. E. Gerald, Y. Chen, and J. Huang, "Probing the Theoretical Ultimate Limit of Coaxial Cable Sensing: Measuring Nanometer-Scale Displacements," *IEEE Trans. Microw. Theory Tech.,* 2019.

[42] S. Fan, K. Staebell, and D. Misra, "Static analysis of an open-ended coaxial line terminated by layered media," *IEEE Trans. Instrum. Meas.,* vol. 39, no. 2, pp. 435-437, 1990.

[43] N. Pfeiffenberger, G. Pickrell, K. Kokal, and A. Wang, "Sapphire photonic crystal fibers," *Optical Engineering*, vol. 49, no. 9, p. 090501, 2010.

[44] https://www.acsmaterial.com/metal-organic-framework-cu-btc-hkust-1.html.

[45] L. Hamon, E. Jolimaître, and G. D. Pirngruber, "CO2 and CH4 separation by adsorption using Cu-BTC metal− organic framework," *Ind. Eng. Chem. Res.*, vol. 49, no. 16, pp. 7497-7503, 2010.

[46] J. Fu, X. Wang, T. Wei, M. Wei, and Y. Shen, "A cost-effective geodetic strainmeter based on dual coaxial cable Bragg gratings," *Sensors*, vol. 17, no. 4, p. 842, 2017.

[47] M. H. Zarifi, M. Fayaz, J. Goldthorp, M. Abdolrazzaghi, Z. Hashisho, and M. Daneshmand, "Microbead-assisted high resolution microwave planar ring resonator for organic-vapor sensing," *Appl. Phys. Lett.*, vol. 106, no. 6, p. 062903, 2015.

[48] H. El Matbouly, N. Boubekeur, and F. Domingue, "Passive microwave substrate integrated cavity resonator for humidity sensing," *IEEE Trans. Microw. Theory Tech.*, vol. 63, no. 12, pp. 4150-4156, 2015.

[49] A. Abdelghani *et al.*, "Capacitive microwave resonator printed on a paper substrate for CNT based gas sensor," in *2017 IEEE MTT-S International Microwave Symposium (IMS)*, 2017: IEEE, pp. 513-516.

[50] N. Nijem, K. Fürsich, S. T. Kelly, C. Swain, S. R. Leone, and M. K. Gilles, "HKUST-1 thin film layer-by-layer liquid phase epitaxial growth: film properties and stability dependence on layer number," *Crystal Growth & Design*, vol. 15, no. 6, pp. 2948-2957, 2015.

[51] S. Tao, L. Xu, and J. C. Fanguy, "Optical fiber ammonia sensing probes using reagent immobilized porous silica coating as transducers," *Sensors and Actuators B: Chemical*, vol. 115, no. 1, pp. 158-163, 2006.

[52] P. Bahoumina *et al.*, "Microwave flexible gas sensor based on polymer multi wall carbon nanotubes sensitive layer," *Sensors and Actuators B: Chemical*, vol. 249, pp. 708-714, 2017.

[53] F. Röck, N. Barsan, and U. Weimar, Electronic nose: current status and future trends. *Chemical reviews*, vol, 108, pp. 705-25, 2008.

SECTION

2. CONCLUSIONS AND FUTURE WORK

2.1. CONCLUSIONS

The objective of this research is to advance the frontiers of sensing technologies, specifically, to advance the waveguide interferometry-based sensing technologies. To this end, the two most widely used cylindrical waveguides, i.e., optical fiber and coaxial cable, were employed as the platform, and one of the simplest configuration, i.e., Fabry-Perot interferometers, was employed as the fundamental sensing principle in this research.

We proposed a user-configurable triangle geometry-based displacement transfer mechanism, from which a novel one-dimensional fiber-optic EFPI displacement sensor with an unprecedented dynamic range, up to 2.0 cm, was successfully developed. We employed the sensor to monitor the shrinkage during the drying/curing stage of a square brick of mortar, demonstrating its high sensitivity, high resolution, and stability in practical applications. The robust and easy-to-manufacture sensor can be easily commercialized and has great potential for applications in the chemical-oil industry, construction industry, and other industries with harsh environments. Based on the triangle geometry-based displacement transfer mechanism, we reported a fiber-optic sensor that was capable of measuring three-dimensional displacements, including interfacial sliding and debonding during delamination. The sensor was calibrated and then used to monitor interfacial sliding and debonding between a long square brick of mortar and its support structure (i.e., a steel base plate) during the drying/curing process. This robust and easy-to-manufacture triaxial

EFPI-based 3D displacement sensor has great potential in structural health monitoring and other applications. These two novel sensors further expanded the application scope of fiber-optic EFPI-based sensor devices.

Open-ended coaxial probes have been widely explored and commercialized for dielectric spectroscopy at microwave frequencies over the past decades. The working principle of the probes relies on the dependence of the fringing field on the complex permittivity of the material in front of the open end. Inspired by the fiber-optic EFPI, we developed an innovative and universal ultra-sensitive microwave sensing platform based on an open-ended hollow coaxial cable resonator (OE-HCCR, i.e., coaxial cable EFPI). Two highly-reflective microwave reflectors were fabricated in a coaxial cable to form a microwave Fabry-Perot etalon. Although the operating wavelength of the proposed device is increased by five orders of magnitude compared to the fiber-optic EFPI (e.g., from 1500 nm to 150 mm), the resolution of the proposed OE-HCCR device is as high as one nanometer, which is comparable to that of the EFPI. The resolution can be further increased by high-precision machining of the device. Due to its low cost, high sensitivity, all-metal structure, robustness, and ease of signal demodulation, it is envisioned that the proposed device will revolutionize the sensing field and enable many important sensing applications that take place in harsh environments. Compared to a fiber-optic EFPI, the discrete resonance pattern of the OE-HCCR device makes it easier to monitor parameters of interest (e.g., displacement) by simply tracking the resonance frequency. The system cost of the OE-HCCR device is much lower than a fiber-optic EFPI system, including sensor fabrication and the interrogation unit. Note that although a VNA was employed in the demonstration, a less expensive scalar network analyzer can be used to interrogate the OE-

HCCR device. The ruggedized all-metal structure of the OE-HCCR device offers high mechanical stability, robustness, and drastically enhanced temperature tolerances, making the OE-HCCR device an excellent candidate for high-temperature applications. Conducting materials with higher melting points (e.g., tungsten, graphite) can be used to construct the OE-HCCR device for applications at extremely high temperatures. Although the size of the prototype OE-HCCR device was larger than a bare optical fiber with a cladding diameter of 125 μm, the dimensional size of the OE-HCCR device can be further reduced to the micrometer scale according to transmission line theory. One major limitation of the OE-HCCR device is its susceptibility to electromagnetic interference (EMI). The device should be carefully packaged in a metal container (Faraday cage) to avoid EMI in harsh environments. However, the packaging could increase the size and weight of the OE-HCCR device. Therefore, it is preferable to use the proposed OE-HCCR device in EMI-free harsh environments that experience high temperatures, high pressures, and that involve heavy-duty circumstances.

In addition to measurements of the movement of the metal plate, the OE-HCCR was also sensitive to variations of the dielectric properties of the gap medium between the open end of the coaxial cable and the metal plate. Therefore, combining the chemical-specific adsorption properties of metal-organic framework (MOF) materials with the dielectric sensitivity of the OE-HCCR, we reported a mechanically-robust and portable gas sensor device (OE-HCCR-MOF) with high chemical selectivity and sensitivity. The proposed OE-HCCR-MOF is essentially a new portable chemical sensor platform, and its capability for dielectric measurements could find potential applications in various chemical fields due to its high sensitivity, chemical selectivity, robustness, ease of fabrication, user-

configurability, and ease of signal interrogation. The proposed OE-HCCR-MOF structure paves the way for developing a new generation of low-cost, real-time, portable, and powerful *in situ* devices for chemical analyses. A promising application of the OE-HCCR-MOF device is the detection of VOCs for diagnosis of chronic diseases in medical applications; the OE-HCCR would virtually function as an electronic nose.

2.2. FUTURE WORK

It is envisioned that couplings of the metal conductor to the open end of the OE-HCCR device, using judicious mechanical designs, will produce flexibly-designed sensor devices capable of measurements of a variety of physical parameters, such as temperature, acoustic pressure, static pressure, vibration, acceleration, and tilt with high sensitivity. Figure 2.1 includes schematic diagrams of several examples of sensors that can be fabricated using the OE-HCCR device platform, mimicking the well-known fiber-optic EFPI sensors. For example, an OE-HCCR device configured as a pressure sensor can be fabricated by replacing the metal plate with a metal diaphragm that deflects when it is subject to variations of static or dynamic pressures, as illustrated in Figure 2.1(a). Alternatively, a metal cantilever can be fabricated on the enface of the OE-HCCR device so that it can be used for acoustic sensing, as shown in Figure 2.1(b). Figure 2.1(c) illustrates an OE-HCCR device vibration sensor or accelerometer, where an inertial mass block is employed as part of the vibration responsive element. Note that all these sensors can be used at elevated temperatures due to the all-metal structures. Another unique and striking feature of the OE-HCCR device is that the phase information of the device can be directly measured in the microwave domain. By combining a phase-shift amplification

technique, it is possible to resolve changes in the *pseudo* cavity length of the OE-HCCR device with picometer resolution. It is expected that the proposed general OE-HCCR device platform will provide an uncharted route to a novel generation of low-cost and ultra-sensitive sensors that operate at a low frequency (sub-gigahertz and gigahertz regimes) for measuring a variety of physical quantities required by many applications.

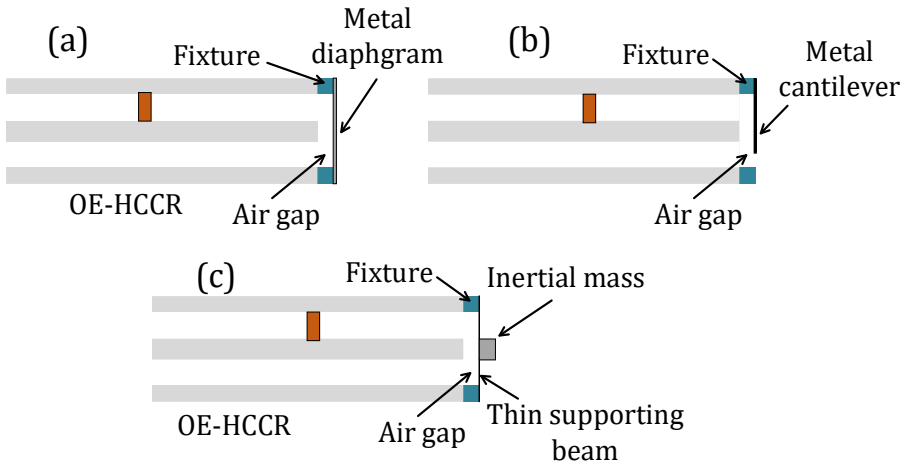

Figure 2.1. Examples of sensors that can be fabricated based on the OE-HCCR device. (a) A pressures sensor. (b) An acoustic sensor. (c) An accelerometer.

BIBLIOGRAPHY

[1] B. H. Bunch and A. Hellemans, The history of science and technology: a browser's guide to the great discoveries, inventions, and the people who made them, from the dawn of time to today. Houghton Mifflin Harcourt, 2004.

[2] B. Culshaw, "Optical fiber sensor technologies: opportunities and-perhaps-pitfalls," Journal of lightwave technology, vol. 22, no. 1, pp. 39-50, 2004.

[3] Z. Fang, K. Chin, R. Qu, and H. Cai, Fundamentals of optical fiber sensors. John Wiley & Sons, 2012.

[4] M. Françon, "Optical interferometry," in Neutron interferometry, 1979.

[5] M. Vaughan, The Fabry-Perot interferometer: history, theory, practice and applications. CRC press, 1989.

[6] T. Yoshino, K. Kurosawa, K. Itoh, and T. Ose, "Fiber-optic Fabry-Perot interferometer and its sensor applications," IEEE Trans. Microw. Theory Tech., vol. 30, no. 10, pp. 1612-1621, 1982.

[7] M. Han and A. Wang, "Exact analysis of low-finesse multimode fiber extrinsic Fabry-Perot interferometers," Applied optics, vol. 43, no. 24, pp. 4659-4666, 2004.

[8] T. Wei, S. Wu, J. Huang, H. Xiao, and J. Fan, "Coaxial cable Bragg grating," Appl. Phys. Lett., vol. 99, no. 11, p. 113517, 2011.

[9] J. Huang, T. Wang, L. Hua, J. Fan, H. Xiao, and M. Luo, "A coaxial cable Fabry-Perot interferometer for sensing applications," Sensors, vol. 13, no. 11, pp. 15252-15260, 2013.

[10] J. Huang, T. Wei, X. Lan, J. Fan, and H. Xiao, "Coaxial cable Bragg grating sensors for large strain measurement with high accuracy," in Sensors and Smart Structures Technologies for Civil, Mechanical, and Aerospace Systems 2012, 2012, vol. 8345: International Society for Optics and Photonics, p. 83452Z.

[11] C. Zhu, Y. Zhuang, Y. Chen, B. Zhang, and J. Huang, "Contactless liquid interface measurement based on a hollow coaxial cable resonator," Sens. Actuators A Phys., vol. 285, pp. 623-627, 2019.

[12] C. Zhu, Y. Zhuang, Y. Chen, and J. Huang, "A Liquid-Level Sensor Based on a Hollow Coaxial Cable Fabry-Perot Resonator With Micrometer Resolution," IEEE Trans. Instrum. Meas., no. 99, pp. 1-6, 2018.

[13] C. Zhu, Y. Chen, Y. Zhuang, and J. Huang, "A Centimeter-Range Displacement Sensor Based on a Hollow Coaxial Cable Fabry–Perot Resonator," IEEE Sens. J., vol. 18, no. 11, pp. 4436-4442, 2018.

[14] C. Zhu, Y. Chen, Y. Zhuang, and J. Huang, "Displacement and Strain Measurement up to 1000° C Using a Hollow Coaxial Cable Fabry-Perot Resonator," Sensors (Basel, Switzerland), vol. 18, no. 5, 2018.

[15] C. Zhu, Y. Zhuang, Y. Chen, and J. Huang, "A hollow coaxial cable Fabry–Pérot resonator for liquid dielectric constant measurement," Rev. Sci. Instrum., vol. 89, no. 4, p. 045003, 2018.

VITA

Chen Zhu was born in Zhongxiang, Hubei, China. He received his B.E. degree in Opto-electronics Information Engineering from the Huazhong University of Science and Technology, Wuhan, China, in 2015. He then spent one year in graduate school at Huazhong University of Science and Technology as a master student, majoring in Optical Engineering. He joined the Department of Electrical and Computer Engineering at the Missouri University of Science and Technology as a Ph.D. student in December 2016, when he was also hired as a Graduate Research Assistant working in the Lightwave Technology Lab at Missouri University of Science and Technology. In May 2021, he received his Ph.D. degree in Electrical Engineering from Missouri University of Science and Technology. His research interest was focused on the development of optical fiber and coaxial cable-based devices and instrumentation for sensing applications in energy, intelligent infrastructures, and clean environments.

He was a recipient of the IEEE Instrumentation and Measurement Society Graduate Fellowship Award from 2018 to 2019 and a recipient of the College of Engineering and Computing Dean's Ph.D. Scholars award in 2019 at Missouri University of Science and Technology. He was a student member of OSA, SPIE, IEEE, the IEEE Instrumentation and Measurement Society, and the IEEE Microwave Theory and Techniques Society.